

THÈSE DE DOCTORAT DE L'ÉCOLE POLYTECHNIQUE

Contrôle optimal en boucle fermée d'instabilités hydrodynamiques par identification de modèles réduits

présentée par

Aurélien Hervé

pour obtenir le titre de

Docteur de l'École Polytechnique

Soutenue en novembre 2012

Devant un jury composé de :

C. Airiau

A. Morgans *Rapporteur*

P. Mouyon

B.R. Noack *Rapporteur*

J.C. Robinet

P.J. Schmid *Encadrant de thèse*

D. Sipp *Directeur de thèse*

Résumé

Résumé

Ces travaux sont consacrés au contrôle en boucle fermée d'écoulements instationnaires, et en particulier à l'établissement théorique de méthodes pratiques de réduction de modèle dédiées au contrôle. Des techniques d'identification sont utilisées sur deux cas d'écoulements, respectivement représentatifs d'écoulements amplificateurs de bruit et d'écoulements oscillants. Dans chaque cas, une approche physique permet de déterminer une structure de modèle à identifier, et un cas fonctionnel de contrôle est présenté.

Mots clefs Identification, modèle réduit, contrôle, mécanique des fluides, contrôle non linéaire, POD, ARX, ARMAX, NARMAX

Abstract

This work aims at defining a low order modeling framework, in order to perform flow control. Two different flow configurations are introduced, that respectively represent a typical case of an amplifier flow and an oscillator flow. For both flows, system identification techniques along with a physical study of the flow are used in order to define a low order model that is suited for control purposes. An efficient closed loop control system is then built, and used to suppress the flow unsteadiness.

Keywords system identification, model reduction, flow control, fluid mechanics, non linear control, POD, ARX, ARMAX, NARMAX

Remerciements

Cette thèse a été réalisée à l'ONERA-DAFE. Je tiens en premier lieu à remercier Laurent Jacquin, mais également l'ensemble du personnel du laboratoire pour l'accueil chaleureux qui m'y a été réservé. Ce fut pour moi un grand plaisir de travailler dans ce laboratoire durant ces trois années de thèse. Merci notamment à Dominique Grandson dont la gentillesse et l'efficacité rendent si facile la vie dans ce laboratoire.

Merci tout particulièrement à Denis Sipp pour m'avoir fait confiance au démarrage de cette thèse, mais surtout pour l'avoir encadré comme tu l'as fait. Ta passion de la recherche et ton énergie sont décidément communicatives, et c'est véritablement d'une disponibilité sans faille, associée à une invariable bonne humeur dont tu fais constamment preuve. C'est sans aucun doute grâce à toi que j'ai pu autant apprécier de traverser cette période, en découvrant le métier passionnant de chercheur.

Merci également à Peter Schmid, également encadrant de cette thèse. C'est toujours avec plaisir que je me suis rendu à nos nombreuses réunions, et notamment au café Daguerre. Beaucoup de café, une aspirine et quelques bons mois de travail suffisent généralement à digérer l'incroyable quantité d'idées qui fusent durant ces moments. C'est grâce à ton implication au long de cette thèse, et notamment durant la difficile période de la rédaction que j'ai aujourd'hui la chance de pouvoir publier ces travaux tels qu'ils sont.

Je tiens bien évidemment à remercier Justine Daffas qui fait désormais incontestablement partie des spécialistes de ce domaine — pourtant bien malgré elle — pour sa courageuse relecture et son soutien moral.

Merci aussi à tous ceux qui contribuent à la bonne ambiance de ce laboratoire. Sami Yamouni, dont j'eus l'honneur de partager le bureau, mais également l'ensemble des doctorants de l'ONERA.

Enfin, merci à ma famille et à tous mes proches qui m'ont offert la possibilité d'effectuer cette thèse dans de si bonnes conditions.

Table des matières

Table des matières	iv
1 Introduction	1
1.1 Instabilités hydrodynamiques	1
1.2 Stratégies de contrôle	3
1.3 Réduction de modèle	5
1.4 Positionnement et objectifs de cette thèse	9
1.5 Plan	13
2 A physics-based approach to flow control using system identification	15
2.1 Résumé de l'article	15
3 Non linear control of vortex shedding phenomenon using low order model identification	55
3.1 Résumé de l'article	55
4 Conclusions	93
4.1 Bilan des travaux présentés	93
4.2 Perspectives futures	94
Bibliographie	99

Introduction

Le domaine du contrôle des écoulements connaît aujourd’hui un essor croissant au sein de la communauté scientifique. Les progrès technologiques aussi bien que scientifiques qui en découlent permettent d’envisager des applications touchant aussi bien à l’industrie aéronautique qu’automobile. L’amélioration de systèmes de mélanges, la suppression d’instabilités, la réduction d’émissions sonores, la diminution de la traînée et l’augmentation du rendement énergétique des véhicules sont autant de problématiques auxquelles le contrôle d’écoulement permet d’apporter des solutions technologiques. Dans un contexte où les ressources énergétiques se font de plus en plus précieuses, la perspective d’importantes réductions de consommation des moyens de transport par le contrôle d’écoulement touche à des enjeux aussi bien économiques qu’écologiques, et fait de ce domaine un axe de recherches particulièrement prometteur.

Les travaux présentés dans cette thèse s’inscrivent dans le cadre du contrôle des instabilités hydrodynamiques, et s’axent en particulier sur l’établissement théorique de méthodes de contrôle applicables en conditions expérimentales par identification de modèles réduits.

1.1 Instabilités hydrodynamiques

Parmi les configurations présentant des instabilités hydrodynamiques, on peut distinguer deux principaux types d’écoulements : les écoulements *auto-oscillants* (ou oscillateurs) et les *amplificateurs de bruits*. Ceux-ci sont instables linéairement et font apparaître de fortes non-linéarités, tandis que ceux-là ne doivent leur instabilité apparente qu’à des excitations extérieures, lesquelles ne sont pas forcément facilement détectables en conditions réelles. Chacune de ces instabilités donne lieu à des stratégies de contrôle strictement différentes, et un écoulement représentatif de chaque instabilité sera étudié dans cette thèse pour en illustrer les différents aspects.

1.1.1 Écoulements oscillants

Les écoulements oscillants se caractérisent par une dynamique oscillatoire auto-entretenue. Pour de faibles nombres de Reynolds,



Figure 1.1 – Allée tourbillonnaire de strato-cumulus, créée par l’île volcanique de Rishiri-to, au nord du Japon (source : NASA).

les effets visqueux stabilisent l'écoulement. Au-delà d'un certain nombre de Reynolds en revanche les effets advectifs l'emportent, et une bifurcation de Hopf se manifeste : une solution stationnaire instable théorique (champ de base) coexiste alors avec un état instationnaire excité, que l'on observe aussi bien numériquement qu'expérimentalement (Sipp and Lebedev, 2007). Parmi les écoulements oscillateurs étudiés dans le contrôle des écoulements, on peut notamment citer les écoulements supercritiques au-dessus de cavités (Akervik et al., 2007; Samimy et al., 2007a; Cattafesta et al., 2008; Barbagallo et al., 2009; Illingworth et al., 2011), les allées tourbillonnaires de type *Von Karman* (Tokumaru and Dimotakis, 1991; He et al., 2000; Protas and Wesfreid, 2002; Bergmann and Cordier, 2008; Ahuja and Rowley, 2010), des profils fortement chargés (Luchtenburg et al., 2009; Ahuja and Rowley, 2010), un écoulement au-dessus d'une bosse (Ehrenstein and Gallaire, 2008; Ehrenstein et al., 2010) ou encore le phénomène de tremblement transsonique (Jacquin et al., 2005; Deck, 2005; Crouch et al., 2007), dont le déclenchement en conditions réelles de vol s'avérerait catastrophique. Un exemple à grande échelle d'allée tourbillonnaire est montré figure 1.1. On y voit le sillage d'une île volcanique, rendu visible par une couche de strato-cumulus présents dans l'atmosphère.

Généralement peu sensibles aux conditions extérieures, les écoulements auto-oscillants sont caractérisés par la présence d'un cycle limite au long duquel oscillent les différents coefficients aérodynamiques. Une fois déclenchées, les oscillations s'auto-entretiennent sans limite, même en l'absence totale d'excitation extérieure. La stabilisation des instabilités par le contrôle permettent de ramener l'écoulement vers un état stable, défini par le champ de base, et dont l'existence peut être montrée théoriquement.

1.1.2 Amplificateurs



Figure 1.2 – Instabilité de Kelvin-Helmholtz visible dans le ciel (photo credit : Brooks Martner, NOAA/ETL).

Contrairement aux écoulements oscillants, les amplificateurs de bruit (ou amplificateurs) sont linéairement stables, mais ils amplifient localement les perturbations extérieures, de sorte qu'ils paraissent instables en pratique. De nombreux amplificateurs de bruit ont été traités dans le cadre du contrôle d'écoulement. On peut citer parmi ceux-ci les couches limites (Bewley and Liu, 1998; Kim, 2003; Chevalier et al., 2007; Kim and Bewley, 2007; Boiko et al., 2008; Bagheri et al., 2009), les écoulements en aval d'une marche (Blackburn et al., 2008; Barbagallo et al., 2012), ou les écoulements de canaux (Ilak and Rowley, 2008).

Le contrôle d'écoulement stable présente une difficulté supplémentaire à celui des écoulements instables, en ce que la modélisation des perturbations extérieures ainsi que celle de leur action sur le système devient cruciale pour la mise en place d'un contrôle efficace. Contrairement aux cas des écoulements oscillants, l'objectif est ici de stabiliser un écoulement lorsque celui-ci est soumis à des excitations extérieures inconnues.



Figure 1.3 – Générateurs de vortex en soufflerie pour le contrôle passif d’écoulement derrière une bosse (Godard and Stanislas, 2006).

1.2 Stratégies de contrôle

Parmi les différentes stratégies de contrôle mises en place, on peut en distinguer deux catégories fondamentales. La première, désignée comme *contrôle passif*, cherche à modifier la géométrie ou ajouter des éléments fixes afin de contrôler l’écoulement. Plus récemment, le *contrôle actif* a fait son apparition en mécanique des fluides. Ce type de contrôle se subdivise lui même en deux sous-catégories, que sont le contrôle en boucle ouverte et le contrôle en boucle fermée.

1.2.1 Contrôle passif

Le contrôle passif consiste à modifier le comportement de l’écoulement au moyen d’artefacts ou de modifications de géométrie. On peut en citer comme exemple l’ajout de générateurs de vortex destinés à dynamiser une couche limite (Lin (2002); Godard and Stanislas (2006), voir figure 1.3), le placement d’un cylindre en amont d’une cavité (Illy et al. (2005), voir figure 1.4), l’emploi de rugosités ou de rides pour le contrôle d’écoulement derrière un cylindre (Shih et al., 1993; Bearman and Harvey, 1993) ou encore celui d’une couche limite séparée (Boiko et al., 2008).

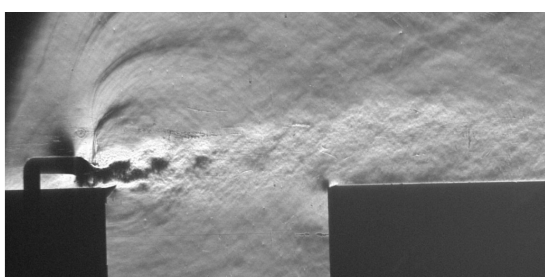


Figure 1.4 – Contrôle passif au-dessus d’une cavité au moyen d’un cylindre (Illy et al., 2005).

Bien que les systèmes de contrôle passif puissent donner de bons résultats de contrôle dans certaines configurations, on pourra souvent leur reprocher un manque d’adaptabilité et de robustesse face à des conditions d’écoulement changeantes. L’évolution des technologies a récemment permis d’introduire le *contrôle actif* en mécanique des fluides, qui permettent de palier à ces difficultés afin d’envisager une gamme d’applications plus large en même temps qu’il permet des performances accrues.

1.2.2 Contrôle actif

Contrairement aux systèmes passifs, les contrôleurs actifs requièrent un apport en énergie, et permettent une gamme d'applications plus large en même temps qu'ils posent des difficultés technologiques nouvelles. Le coût supplémentaire d'un contrôle actif se justifie généralement par un bilan énergétique global positif, par exemple lorsque l'énergie injectée permet de réduire significativement la traînée d'un appareil, en diminuant ainsi la consommation totale.

Les moyens d'agir sur un fluide sont nombreux, tels des lames vibrantes, des systèmes de soufflage/suction à la paroi, une rotation contrôlée de cylindre, ou encore plus récemment l'utilisation de plasmas, permettant d'injecter de la quantité de mouvement dans un fluide (voir figure 1.5).

Boucle ouverte Le contrôle en boucle ouverte consiste à agir sur le fluide selon une loi de contrôle prédéterminée, et optimisée hors ligne. On peut notamment citer les travaux de ([Tokumaru and Dimotakis, 1991](#); [He et al., 2000](#); [Protas and Wesfreid, 2002](#)), dans lesquels un cylindre en rotation commandée permet d'améliorer significativement l'aérodynamique de l'écoulement. Le contrôle en boucle ouverte reste cependant assez limité dans la mesure où il ne s'adapte pas aux conditions de l'écoulement.

Boucle fermée Avec l'évolution des technologies temps-réel, on cherche aujourd'hui à utiliser des lois de contrôle adaptatives, dans le cadre du *contrôle en boucle fermée*. Une information est prise en direct dans l'écoulement (mesures de frottements pariétaux, de vitesse, de pression...) et est utilisée par un algorithme qui en déduit une loi de contrôle optimale à appliquer pour atteindre l'objectif prescrit. Le système de contrôle comporte alors des entrées (mesure(s) prise(s) dans le fluide), ainsi que des sorties (loi de contrôle) et évolue en temps réel en même temps que l'écoulement qu'il cherche à contrôler. Les avantages principaux du contrôle en boucle fermée sont d'augmenter la robustesse face aux perturbations et changements de conditions ([Cattafesta et al., 2003](#)), ainsi que de diminuer de manière drastique la puissance nécessaire à l'actuateur ([Cattafesta et al., 1997](#)) en améliorant l'efficacité de la loi de contrôle.

Le contrôle en boucle fermée, numérique ou expérimental, a déjà été appliqué avec plus ou moins de succès à de nombreux écoulements. Dans la majorité des cas la réalisation du contrôle se fait sur des simulations numériques. On peut citer parmi les écoulements étudiés les oscillations de cavité ([Cattafesta et al., 2008](#); [Barbagallo et al., 2009](#); [Illingworth et al., 2011](#)), des allées tourbillonnaires ([Choi et al., 2008](#); [Ma et al., 2010](#)), des cas de couches limites ([Bagheri et al., 2009](#)), ou encore une marche descendante ([Barbagallo et al., 2012](#)). Si elles sont moins nombreuses du fait de la difficulté de porter les méthodes numériques vers des configurations réelles, des applications expérimentales ont été réalisées,

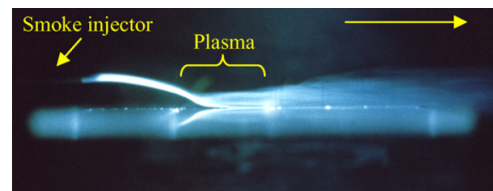


Figure 1.5 – Manipulation par plasma d'un écoulement au-dessus d'une plaque plane. Sans plasma, le filet de fumée reste horizontal ([Moreau, 2007](#)).

notamment par [Morgans and Dowling \(2007\)](#); [Samimy et al. \(2007a\)](#); [Illingworth et al. \(2011\)](#) dans des cas d'oscillations de combustion ou de cavité.

Pour envisager un contrôle en boucle fermée expérimental efficace, il est nécessaire de manipuler des équations d'optimisation en temps réel. L'information tirée du fluide sert au calcul d'une loi de contrôle adaptée, laquelle est immédiatement appliquée. Bien qu'il soit théoriquement possible de résoudre un problème d'optimisation à partir des équations de Navier-Stokes, les dimensions des modèles classiques CFD sont bien trop élevées (de l'ordre du million de variables) pour espérer réaliser une optimisation suffisamment rapide. On a alors recours à des *modèles réduits* ([Booker et al., 1999](#); [Gunzburger, 2000](#)), dont le rôle est de mimer la dynamique de l'écoulement au moyen d'un faible nombre d'équations (avec des dimensions de l'ordre de la dizaine).

1.3 Réduction de modèle

En substituant les équations du modèle réduit à celles du problème de grande dimension, on peut optimiser une loi de contrôle rapidement. On comprend dès lors aisément que la qualité de la loi de contrôle dépendra très fortement de la qualité du modèle réduit. Plus ce dernier présente une dynamique similaire à celle de l'écoulement, plus la loi de contrôle sera pertinente. Un des principaux enjeux du contrôle en boucle fermée consiste donc à définir un modèle réduit efficace pour le contrôle. La réduction de dimension implique de négliger la majeure partie des informations présentes dans le fluide, tandis que la précision du modèle impose d'être capable de prévoir efficacement l'évolution d'un certain nombre de paramètres du fluide.

L'immense majorité des travaux actuels consiste à chercher des modèles linéaires qui captent la dynamique linéarisée des équations de Navier-Stokes autour du champ de base. On peut ainsi estimer à faible coût la dynamique dans le voisinage de l'objectif, et en dériver un contrôle efficace. La pertinence de cette approche peut être justifiée à la fois dans le cadre des amplificateurs de bruit, et dans celui des oscillateurs faiblement supercritiques comme expliqué ci-après.

Considérons dans un premier temps les amplificateurs. Dans ce cadre on utilise les équations incompressibles adimensionnées de Navier-Stokes en notant respectivement les champs de vitesse et de pression v_{tot}, p_{tot} :

$$\nabla v_{tot} = 0 \quad (1.1a)$$

$$0 = \partial_t v_{tot} + v_{tot} \cdot \nabla v_{tot} + \nabla p_{tot} - \frac{1}{Re} \Delta v_{tot} + \varepsilon W, \quad (1.1b)$$

où le terme εW introduit un forçage représentatif des perturbations extérieures excitant l'écoulement. De la définition du champ de base v_0 comme solution stationnaire à l'équation (1.1), on dérive alors l'équation en termes de perturbations autour de v_0 par $v_{tot} = v_0 + \varepsilon v$:

$$\nabla v = 0 \quad (1.2a)$$

$$-\varepsilon(v \cdot \nabla v) = \partial_t v + v_0 \cdot \nabla v + v \cdot \nabla v_0 + \nabla p - \frac{1}{Re} \Delta v + W. \quad (1.2b)$$

La dynamique mise en évidence dans (1.2) devient alors linéaire en v (v_0 est constant) lorsque $\varepsilon \rightarrow 0$, c'est à dire lorsque les perturbations de l'écoulement autour du champ de base sont suffisamment petites (conditions "calmes").

Dans le cadre d'un écoulement instable faiblement supercritique (allée tourbillonnaire, cavité...), on peut montrer (Sipp and Lebedev, 2007) que la dynamique linéaire prévoit la croissance exponentielle d'un mode oscillant. Bien qu'un modèle purement linéaire ne soit pas en mesure de prévoir l'amortissement de cette croissance dû aux effets non-linéaires, l'étude de la dynamique linéaire fournit suffisamment d'informations sur la fréquence et l'amplitude des modes instables pour permettre un contrôle efficace (Barbagallo et al., 2009; Ahuja and Rowley, 2010). Il faut toutefois garder à l'esprit que cette hypothèse perd sa validité lorsque le nombre de Reynolds augmente. Une partie des travaux présentés ici visera à étendre le domaine possible d'application, notamment par l'emploi de modèles non-linéaires (voir §1.4).

Dans cette thèse on s'intéressera particulièrement aux significations physiques des méthodes de réduction, et à leur capacité à "compresser" la dynamique de manière efficace. Pour ce faire, il peut être utile de considérer les méthodes existantes selon un classement de réduction *spatiale* (§1.3.1) ou *temporelle* (§1.3.2). On montrera alors que si ces deux types d'approches peuvent s'avérer identiques dans une approche linéaire idéale, ils permettent en réalité d'approcher différents phénomènes avec plus ou moins de succès, et peuvent s'avérer complémentaires dans certains cas.

1.3.1 Réduction spatiale (POD)

La méthode actuelle la plus populaire dans le domaine de la réduction de modèles dédiés au contrôle est sans doute la POD (Proper Orthogonal Decomposition) (Sirovich, 1991; Berkooz et al., 1993; Holmes et al., 1996; Noack et al., 2003). Cette technique vise à créer une base orthonormale de vecteurs $\Phi_k, k \in (1..n)$ de faible dimension n , de sorte qu'un champ de vitesse v puisse être exprimé comme combinaison linéaire de ces vecteurs de base :

$$v \approx \sum_{k=1}^n x_k \Phi_k, \quad x_k = \langle v, \Phi_k \rangle \quad \forall k \quad (1.3)$$

L'algorithme POD optimise alors la différence $\|v - \sum x_k \Phi_k\|$ selon une norme associée au produit scalaire de (1.3) que l'utilisateur aura défini. Généralement, un produit scalaire énergétique

$$\langle u, v \rangle = \iint_{\Omega} ((u_x * v_x) + (u_y * v_y)) d\Omega \quad (1.4)$$

est défini, de manière à capter le maximum d'énergie cinétique de l'écoulement.

Cette technique est particulièrement adaptée à la mécanique des fluides, puisqu'elle n'utilise que des clichés de champs de vitesse pour le calcul de la base. Ces clichés sont désormais largement disponibles, aussi bien par simulation numérique que par mesure expérimentale PIV. La figure 1.6 montre un exemple de modes POD calculés dans le sillage d'un cylindre (Bergmann and Cordier, 2008), et illustre l'aptitude de l'algorithme à décomposer la dynamique observée en structures tourbillonnaires cohérentes.

Bien que la POD en elle-même ne concerne que le calcul de la base, elle est généralement associée à la *projection de Galerkin*, qui consiste simplement à substituer v par $\sum_k x_k \Phi_k$ dans les équations de Navier-Stokes (1.1). Ce faisant, on obtient alors un système d'équations différentielles qui gouvernent les équations des coefficients POD x_k . La méthode Galerkin-POD est aujourd'hui expliquée et utilisée dans de nombreux travaux (Noack et al., 2003; Rowley et al., 2004; Bergmann et al., 2005; Barbagallo et al., 2009; Cordier et al., 2010), ainsi que dans la majorité des publications citées ici dans le domaine du contrôle en boucle fermée.

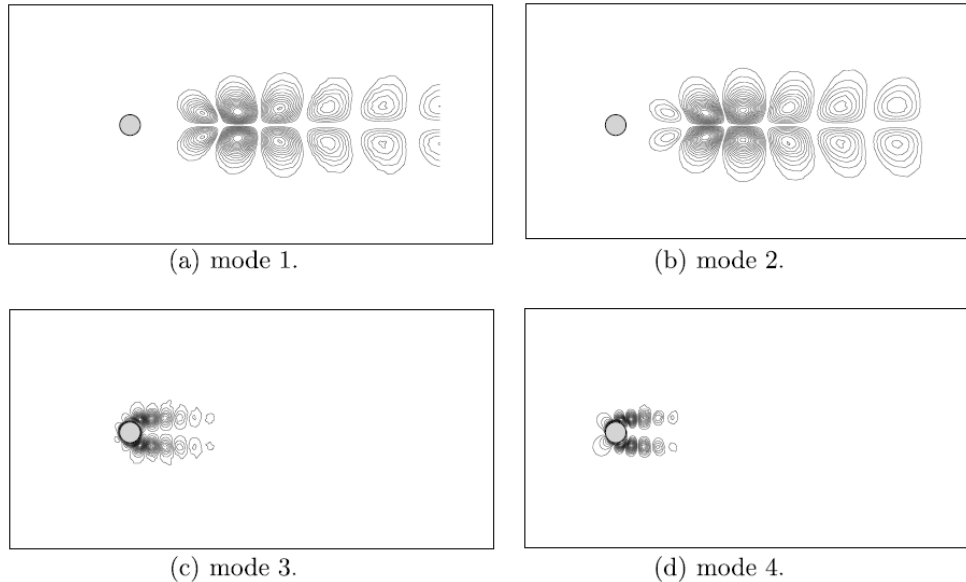


Figure 1.6 – Contours de pression de 4 modes POD issus d'un écoulement derrière un cylindre (Bergmann and Cordier, 2008).

Si on classe la POD comme une méthode de réduction spatiale, c'est qu'elle permet de sélectionner les structures spatiales cohérentes les plus énergétiques, tandis que les structures de faibles dimensions spatiales sont ignorées. L'avantage de cette représentation est de capturer en un très faible nombre de modes de larges structures cohérentes (comme les structures tourbillonnaires visibles figure 1.6(a) et (b)). Dans le cadre du contrôle en revanche, on cherche généralement à agir sur l'écoulement en y introduisant le moins d'énergie possible. En plaçant l'action à des endroits pertinents, par exemple dans une zone d'instabilité convective, on peut impacter l'écoulement de manière significative sans pour autant agir de manière visible. Représenter l'influence directe d'un contrôle sur une base POD peut dès lors s'avérer très délicat, puisque la POD cherche par définition à ignorer les détails spatiaux. De la même manière, il peut s'avérer difficile de représenter des phénomènes d'instabilités convectives, lorsque les structures spatiales évoluent en même temps qu'elles sont advectées par l'écoulement. Un grand nombre de modes POD est alors nécessaire pour représenter de tels phénomènes, ainsi que la dynamique qui lie l'évolution des modes entre eux. Bien que la description de tels mécanismes soit possible dans le formalisme Galerkin-POD, elle nécessite un grand nombre de modes POD, ce qui

pénalise la dimension finale du modèle, et donc l'intérêt de la méthode. On montrera en §1.3.2 que les modélisations par réduction dite *temporelle* sont plus adaptées à ce types d'écoulements.

Plus récemment, la *Balanced-POD* (ou BPOD) est apparue en mécanique des fluides. L'objectif est alors non plus de capturer l'énergie de l'écoulement, mais de capturer la dynamique linéaire qui lie l'actuateur (entrée du système) à la sortie (où la sortie désigne la mesure utilisée pour piloter le contrôleur). Pour qu'un mode POD soit intéressant dans le cadre du contrôle, il faut en effet qu'il soit *observable* (*i.e.* avoir une influence visible sur la mesure, pour être détectable) et *contrôlable* (*i.e.* que l'on puisse influer au moyen de la commande). Des exemples de contrôle par balanced-POD sont disponibles dans la littérature, et ont confirmé l'amélioration des performances des modèles basés sur les bases équilibrées (Willcox and Peraire, 2002; Rowley, 2005; Bagheri and Henningson, 2011; Illingworth et al., 2011).

1.3.2 Réduction temporelle

Une approche différente de réduction de modèle consiste à utiliser des modèles que l'on désignera ici comme *temporels*. Dans le cadre linéaire, les modèles dynamiques Galerkin-POD sont généralement exprimés sous la forme

$$X^{t+1} = AX^t + Bu^t \quad (1.5a)$$

$$y^t = CX^t + Du^t \quad (1.5b)$$

où X désigne l'état, lequel découle d'une réduction spatiale de l'écoulement, et t l'indice discret temporel. Puisqu'elle décrit un système linéaire, l'équation (1.5) peut également être complètement décrite par sa fonction de transfert, dont l'équation peut s'exprimer comme

$$y(t) = \sum_{k=0}^{\infty} h_k u(t-k). \quad (1.6)$$

Les coefficients h_k sont nommés coefficients de Markov, et décrivent explicitement la réponse du système linéaire à une entrée u impulsionale. Pour un nombre infini de coefficients h_k , une équivalence exacte peut être exprimée entre les équations (1.5) et (1.6) (Antoulas, 2005).

Dans le cadre de la réduction de modèle en revanche, on peut considérer un modèle décrivant un nombre fini de coefficients de Markov. De la troncature de cette suite résulte alors un modèle différent de celui que l'on aurait obtenu en ne gardant que N modes POD. Cette approche de description explicite de fonction de transfert s'adapte particulièrement bien à la modélisation des instabilités convectives, telle que celles rencontrées au sein d'un écoulement de marche descendante (voir figure 1.7 extraite de la partie §2, où la marche de Barkley et al. (2002) est utilisée comme cas d'écoulement amplificateur de bruit). En effet, la stabilité globale de l'écoulement implique $h_k \xrightarrow{k \rightarrow \infty} 0$. Il est alors possible de modéliser ce dernier par une description de sa suite de Markov, que l'on pourra tronquer sans perte significative de la dynamique. Contrairement à l'approche POD, une approche de modélisation temporelle ne nécessite pas de description explicite des perturbations

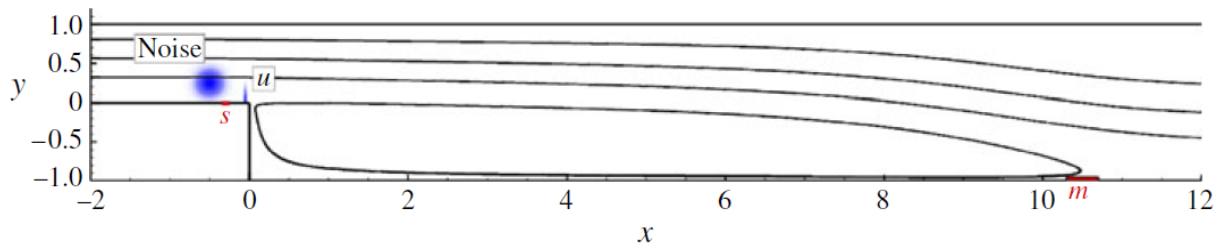


Figure 1.7 – Marche descendante à $Re = 500$.

extérieures pour en décrire les effets sur l’écoulement. De plus, elle permet un modèle compact, là où un grand nombre de modes POD auraient été nécessaires afin de décrire le mécanisme de croissance des perturbations au sein de la couche de mélange.

On peut trouver dans la littérature des exemples de modélisations temporelles par modèles ARX/Subspace ([Huang and Kim, 2008](#)), par la méthode ARMARKOV ([Akers and Bernstein, 1997](#)), utilisée notamment par [Lacy et al. \(1998\)](#) en thermoacoustique, ou encore par l’algorithme ERA, dont l’objectif est de construire un système linéaire à partir d’observations entrée/sortie ([Juang and Pappa, 1985; Ma et al., 2010; Illingworth et al., 2011](#)).

1.4 Positionnement et objectifs de cette thèse

Les travaux présentés dans cette thèse ont pour principal objectif l’établissement de méthodes de réduction de modèle destinées au contrôle en boucle fermée d’écoulements instationnaires. En particulier, et bien que les travaux présentés ici soient purement numériques, on cherchera à définir un formalisme théorique orienté vers une possible réalisation expérimentale. On introduira pour ce faire des techniques d’*identification de système*, dont l’objectif est de modéliser un système d’après son observation directe. Afin d’ouvrir le champ d’applications possibles, on introduira également des non-linéarités dans les modèles proposés.

1.4.1 Vers une réalisation expérimentale

La majeure partie des travaux disponibles dans la littérature utilisent des approches que l’on peut qualifier de *model-based*. Dans cette approche, on postule un modèle qui pilote la dynamique de l’écoulement (équations de Navier-Stokes + maillage), et dont on réduira ensuite la dimension. Si cette approche donne d’excellents résultats en contrôle de simulations numériques, il peut parfois s’avérer très difficile de porter les modèles obtenus en conditions expérimentales. En effet, les imprécisions de modélisation CFD, la méconnaissance des conditions de perturbations extérieures, les possibles aspérités de surface, ou encore la difficulté de mailler des géométries complexes font partie des difficultés auxquelles l’expérimentateur devra parer afin d’obtenir un modèle fiable. En pratique, des méthodes de calibration sont absolument nécessaires à l’utilisation expérimentale

de modèles Galerkin-POD ([Tadmor and Noack, 2004](#); [Couplet et al., 2005](#); [Bergmann and Cordier, 2008](#); [Cordier et al., 2010](#)) ; celles-ci permettent d'adapter le modèle à une configuration particulière à partir de mesures effectuées en condition réelles.

Dans une volonté de proposer une méthodologie à la fois plus simple et plus robuste, les outils utilisés au long de cette thèse dérivent exclusivement des techniques d'identification de système. Cette approche se caractérise par une modélisation fondée uniquement sur la prise directe d'informations dans l'écoulement. Ainsi, aucun modèle ou maillage n'est postulé *a priori*, et c'est de l'observation du système qu'on dérive un modèle réduit.

Si l'utilisation de techniques d'identification permet de résoudre les problématiques énoncées ci-dessus, elle introduit en même temps de nouvelles difficultés qu'il faudra résoudre. La première contrainte est évidemment de n'utiliser que des données effectivement accessibles. Afin de proposer une approche cohérente sur cet aspect, les simulations numériques utilisées dans ces travaux seront généralement traitées comme des données pseudo-expérimentales. On utilisera par exemple des champs de vitesses (obtenus par PIV) ou des mesures de frottements pariétaux (capteurs instationnaires), mais pas de simulation adjointe, ou encore de prise de mesure en plein champ. De la même manière, les actuateurs seront placés à des endroits où une installation paraît plausible. On peut toutefois noter que les modèles numériques CFD utilisés restent assez simplifiés, et ne cherchent pas à modéliser précisément l'action d'un actionneur réel.

L'utilisation de modèles identifiés requiert de plus la définition préalable d'une structure de modèle. Dans chaque partie, c'est une étude physique qualitative de l'écoulement qui permettra la définition d'un modèle compatible avec la dynamique que l'on cherche à modéliser. Une fois de plus, la séparation entre champs amplificateurs de bruit et champs oscillants permet d'isoler des problématiques inhérentes à chaque type d'écoulement, et dans chaque cas un modèle différent est utilisé en conséquence.

Dans le cas des amplificateurs de bruit, on considérera par exemple que les sources extérieures de bruit dont on cherche à contrôler les effets ne sont *a priori* pas connues. Ceci pose une difficulté importante dans la mesure où il est absolument nécessaire de prendre en compte leurs effets sur la dynamique de l'écoulement pour en modéliser l'action. Des solutions seront présentées en §2 pour résoudre à ce problème au moyen d'un capteur instationnaire placé en amont de l'écoulement. À travers l'observation des effets des perturbations extérieures sur un capteur, le modèle sera alors capable de prévoir l'effet de ces mêmes perturbations sur l'objectif final. Aucune information sur lesdites perturbations ne sera pourtant nécessaire à l'obtention du modèle.

Les écoulements oscillants posent quant à eux des difficultés supplémentaires, et deux d'entre elles seront développées ici. La première consiste à définir un objectif accessible. Bien que l'étude numérique d'un lâcher tourbillonnaire permette de déterminer l'existence théorique d'une solution stationnaire (mais instable) de l'écoulement pour des Reynolds supercritiques (champ de base), cette solution n'est jamais observable pratiquement. Le champ de base est pourtant connu comme le seul champ stationnaire accessible, et doit donc être évalué afin de définir un objectif de contrôle acceptable. Il est également important de noter que pour des cas supercritiques, le champ de base ne correspond pas au champ moyen, et ce dernier ne peut donc pas être utilisé comme substitution au champ de base. Dans la partie §3, on montrera pourtant que l'étude de la dynamique saturée de l'écoulement

permet de retrouver avec une bonne précision certaines des caractéristiques du champ de base. On pourra alors fournir un objectif cohérent au système de contrôle, sans avoir recours à un calcul numérique du champ de base.

La deuxième difficulté provient de la forte non-linéarité de la dynamique. L'établissement de l'allée tourbillonnaire peut être décrite comme une croissance exponentielle d'un mode linéaire instable, laquelle est rapidement saturée par les effets non-linéaires. Dans un cadre purement numérique et pour un cas faiblement supercritique, il peut suffire de linéariser la dynamique autour du champ de base pour obtenir un modèle linéaire satisfaisant (Ahuja and Rowley, 2010). Il faut toutefois noter qu'un tel modèle linéaire ne peut qu'au mieux prévoir une croissance exponentielle infinie de ses modes instables. Dans le cadre de l'identification, il devient donc très difficile d'obtenir un tel modèle, puisque celui-ci ne représente pas la dynamique observée (les modes saturent très rapidement en pratique, et la croissance linéaire n'est pas réellement observable). L'objet de la partie §3 sera de proposer un formalisme fondé sur une méthode d'identification de système, qui permettra à la fois d'obtenir un modèle non-linéaire de la dynamique, ainsi qu'une évaluation du champ de base à partir de la dynamique observable, saturée. Un contrôle non-linéaire sera alors proposé, qui s'avérera efficace pour réduire les fluctuations du champ aérodynamique.

1.4.2 Introduction de non-linéarités dans la modélisation

Comme introduit dans la partie §1.3, la majorité des modèles réduits utilisés en contrôle d'écoulements sont purement linéaires. Ceux-ci montrent de bonnes performances dans le cadre de faibles perturbations extérieures pour des amplificateurs de bruit (voir la discussion sur l'équation (1.2)), ou encore pour des oscillateurs faiblement supercritiques. Pourtant ces modèles montrent rapidement leurs limites en dehors du cadre de ces hypothèses. La figure 1.8 montre l'évolution du nombre de Strouhal observable dans un écoulement de lâcher tourbillonnaire derrière un profil (les détails seront présentés dans la partie §3). Comme attendu, on observe une bifurcation de Hopf au Reynolds critique. Si la dynamique linéarisée (courbe bleue) reste très proche de la dynamique saturée (courbe verte) pour des Reynolds faiblement supercritiques, on observe en revanche une différence croissante entre ces deux dernières lorsque le nombre de Reynolds augmente. Plus le Reynolds augmente, et moins il devient pertinent d'utiliser la dynamique linéarisée pour contrôler efficacement l'écoulement. Dans la partie §3, on proposera l'utilisation d'un modèle identifié purement non-linéaire qui permettra de représenter la branche saturée avec fiabilité.

Dans le cadre des amplificateurs de bruit l'emploi de non-linéarités dans le modèle trouve son intérêt pour des raisons différentes. L'identification d'un modèle linéaire passe généralement par la minimisation au sens de la norme 2 de l'erreur de modèle :

$$\|y - f(x)\|^2 = \text{erreur.} \quad (1.7)$$

Si on dispose de suffisamment d'informations sur les entrées, c'est-à-dire sur les perturbations qui viennent exciter le système, il est alors facile de déterminer une dynamique fiable (Huang and Kim, 2008). Malheureusement, ces sources de perturbations sont généralement difficilement détectables, et généralement de nature inconnue. C'est pourquoi il est très

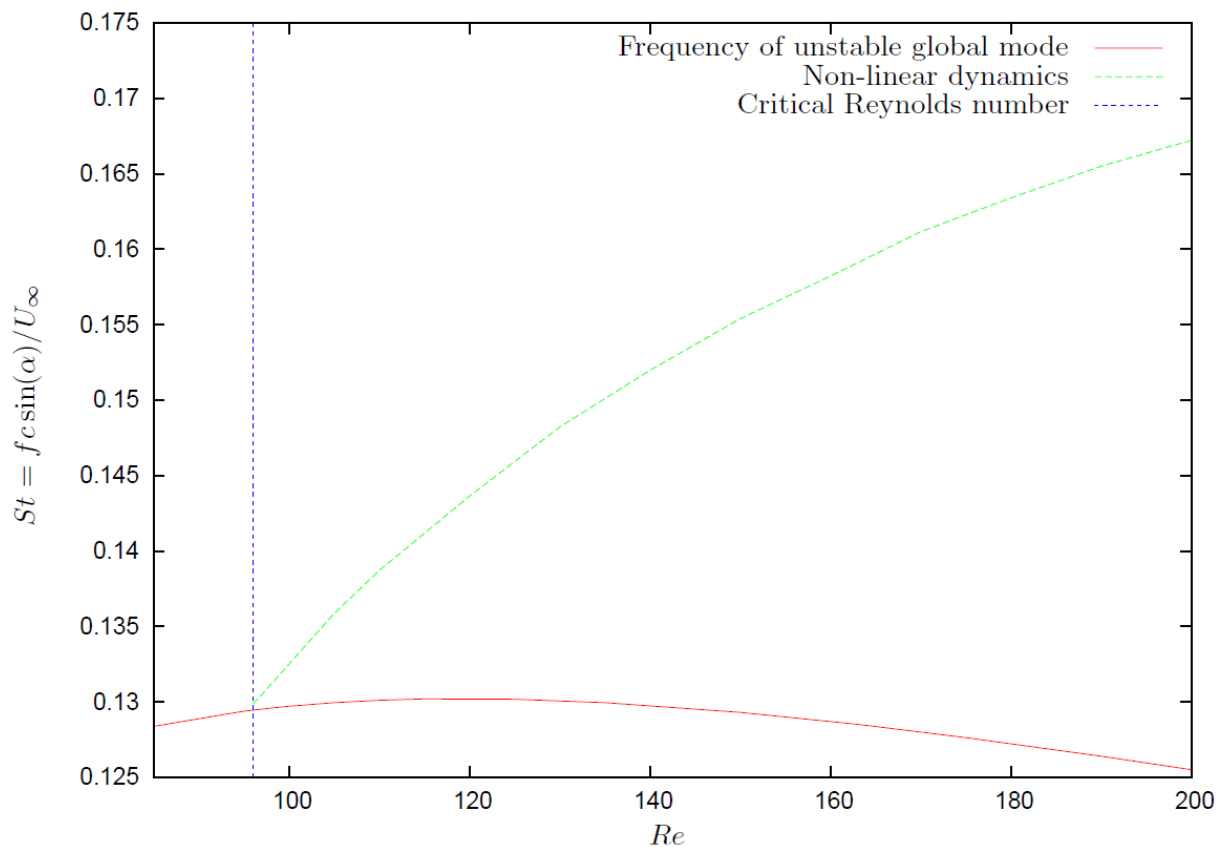


Figure 1.8 – Variations du nombre de Strouhal associé à un écoulement derrière un profil NACA012 d’incidence 30° (extrait de la partie §3). Bleu : limite de criticité. Vert : Strouhal observé. Rouge : Strouhal correspondant aux valeurs propres linéarisées. Plus le nombre de Reynolds augmente, et plus la différence de Strouhal entre linéaire et non-linéaire croît.

probable d’observer une dynamique excitée, sans pour autant connaître la source d’excitation. Dans un cadre de modélisation purement linéaire, cela revient à observer un système qui paraît instable, puisqu’oscillant sans raison apparente. On risque alors d’identifier un modèle faussement instable. Dans la partie §2, on introduira un modèle ARMAX que l’on peut qualifier de pseudo-linéaire (Ljung, 1999). Il consiste en fait en un modèle linéaire, dont l’identification se fait au moyen d’itérations d’un algorithme non-linéaire. Les résultats montreront que l’addition de cette pseudo-non-linéarité permet d’obtenir un modèle particulièrement robuste, même en présence de sources d’excitations non détectables. A l’inverse, des comparaisons montreront que les modèles linéaires (ARX, Subspace) échouent à identifier une dynamique cohérente dès lors qu’on se trouve en présence de sources de bruit non détectées.

1.5 Plan

Cette thèse s'articulera autour de deux publications. La première, présentée en §2, propose le contrôle d'un écoulement de marche descendante à $Reynolds = 500$, lequel correspond à un cas-test d'écoulement amplificateur de bruit. Comme introduit précédemment, l'identification d'un modèle pseudo-linéaire sera réalisée, et sa robustesse face à l'amplitude des perturbations, ainsi que face à des sources de bruit non détectables sera évaluée. Ces travaux ont été publiés au *Journal of Fluid Mechanics* ([Hervé et al., 2012](#)).

La partie §3 sera quant à elle dédiée à l'étude d'un lâcher tourbillonnaire derrière un profil NACA012, qui consiste en un exemple typique d'écoulement oscillateur. Un procédé d'identification purement non-linéaire sera présenté, qui donnera lieu à un contrôle permettant de réduire les fluctuations du champ aérodynamique. Ces travaux font l'objet d'un article soumis au *Journal of Fluid Mechanics* en septembre 2012.

Enfin, les conclusions et perspectives futures seront discutées en §4.

A physics-based approach to flow control using system identification

2.1 Résumé de l'article

Dans cet article on s'intéresse au contrôle d'un écoulement au-dessus d'une marche descendante à $Re = 500$. Ce cas est typique des écoulements amplificateurs de bruit, et présente une dynamique globalement stable, en même temps qu'une zone d'instabilité convective à la suite de la couche de mélange créée par la bulle de recirculation.

Configuration Afin d'observer des instationnarités au sein de la simulation numérique, on définit un forçage volumique aléatoire en amont du sommet de la marche, et proche de la couche limite. Bien que les fluctuations soient connues puisqu'artificiellement introduites dans la simulation, on supposera par la suite qu'aucune information n'est disponible sur cette source de bruit, en accord avec le formalisme pseudo-expérimental introduit en §1. Le schéma de configuration est montré figure 1.7, page 9, et est également schématisé figure 2.1.

Pour permettre le contrôle en boucle fermée, deux capteurs de frottements pariétaux ainsi qu'un forçage volumique sont placés. Le premier capteur amont, dont la valeur de la mesure est notée s , aura pour rôle d'estimer les effets des excitations extérieures, avant même que celles-ci n'atteignent la zone d'instabilité située en aval de la marche. Ainsi, bien que n'ayant aucune information sur la distribution spatiale ou temporelle des excitations, on pourra toutefois en prévoir l'effet au moyen d'un capteur amont.

Le second capteur de frottements (dont la valeur est notée m) est placé en aval de la marche, au pied de la bulle de recirculation. La mesure de ce capteur permet de définir un objectif de contrôle mesurable. L'hypothèse est faite selon laquelle une réduction des fluctuations de ce capteur ne peut s'achever que par une réduction effective des fluctuations de la bulle de recirculation. Ainsi, en construisant un système de contrôle visant à réduire les fluctuations de m , on cherche en réalité à supprimer les instabilités de la bulle de recirculation.

Enfin, le contrôle est situé au sommet de la marche. Il est placé en aval du capteur amont s , ce qui fait de cette configuration une configuration *feed-forward*. En effet, la nature fortement convective de l'écoulement permet de supposer (hypothèse par ailleurs vérifiée) que l'action du contrôle ne sera pas visible sur le capteur amont.

Modélisation Comme introduit en §1, l'écoulement présente une dynamique linéaire lorsqu'il est soumis à des excitations de faible amplitude. L'emploi d'un modèle linéaire est donc possible. De plus, une réduction de type temporelle est choisie, en accord avec la discussion de la partie §1.3. Le modèle a pour objectif de prévoir avec précision les

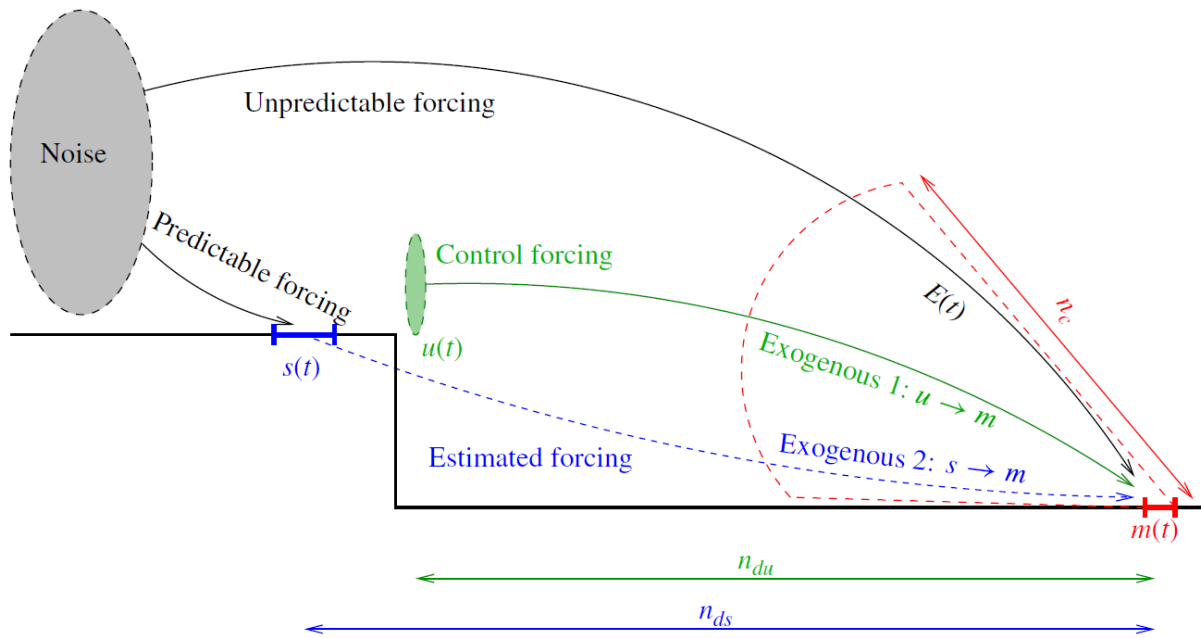


Figure 2.1 – Schéma de la marche, et explication graphique des coefficients du modèle ARMAX

fluctuations de l'objectif (mesure m) à partir des informations fournies par la mesure amont s , ainsi que la connaissance de la loi de contrôle utilisée u . Le modèle utilisé est de type ARMAX. Le choix d'un tel modèle, ainsi que des coefficients nécessaires à sa définition proviennent d'arguments physiques liés à différents temps de convection du système, lesquels sont facilement observables en conditions réelles. L'équation ARMAX complète s'écrit

$$m(t) + \underbrace{\sum_{k=1}^{n_a} a_k m(t-k)}_{auto-regressive} = \underbrace{\sum_{k=n_{du}}^{n_{bu}+n_{du}} b_k^u u(t-k)}_{exogenous 1} + \underbrace{\sum_{k=n_{ds}}^{n_{bs}+n_{ds}} b_k^s s(t-k)}_{exogenous 2} + E(t), \quad (2.1a)$$

$$E(t) = \underbrace{\sum_{k=1}^{n_c} c_k e(t-k) + e(t)}_{moving average}, \quad (2.1b)$$

et ses différents termes sont illustrés par la figure 2.1.

Résultats Dans un premier temps on identifie un modèle ARMAX et on définit une stratégie de contrôle *feed-forward*, fondée sur un formalisme de *Model Predictive Control*

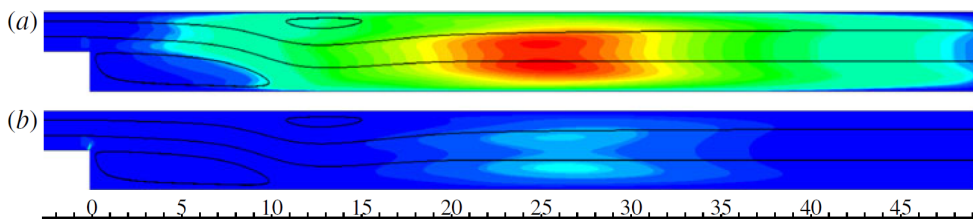


Figure 2.2 – Moyenne de l'énergie des fluctuations dans l'écoulement. En haut : écoulement non contrôlé. En bas : écoulement contrôlé.

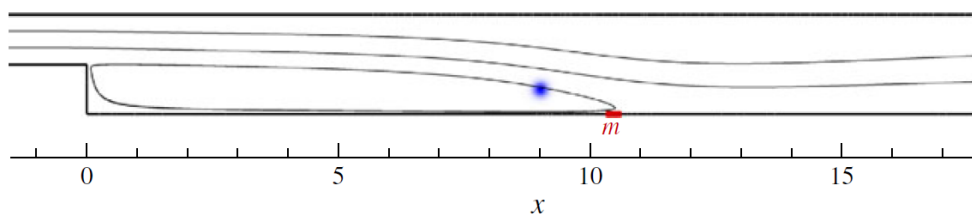


Figure 2.3 – Ajout d'une source de forçage non détectable dans l'écoulement. La source excite le capteur aval, mais ses effets ne sont pas prévisibles à partir des données du capteur amont.

(MPC). Celui-ci cherche à définir une loi de contrôle visant à réduire la prévision de l'objectif (ici les fluctuations de la mesure aval m) sur une fenêtre temporelle définie. Les résultats obtenus sont extrêmement satisfaisants, et montrent une réduction quasi-totale des fluctuations de l'écoulement. La figure 2.2 montre l'énergie moyenne des perturbations avec et sans contrôle. On voit que conformément à l'hypothèse formulée plus haut, la réduction des fluctuations de m s'est bien effectuée par un contrôle efficace de l'ensemble de l'énergie des fluctuations de l'écoulement.

Comme discuté dans la partie §1.4, l'introduction de pseudo-non-linéarités au travers de la partie moving-average permet d'augmenter la robustesse du modèle face aux sources non détectables de bruit. Pour illustrer ce point, une source supplémentaire de bruit est ajoutée dans l'écoulement (figure 2.3). Une fois de plus, on utilise un forçage volumique aléatoire, lequel produit sur la mesure aval un signal supplémentaire. Ce signal étant filtré par l'écoulement avant d'atteindre le capteur, il ne peut pas être assimilé à du bruit blanc. De plus, la position de cette source additionnelle est telle qu'elle ne produit aucun signal détectable sur le capteur amont. Trois différents modèles sont alors identifiés, et comparés. Les deux premiers sont des modèles purement linéaires de type ARX et Subspace (Huang and Kim, 2008), et le troisième est le modèle ARMAX défini plus haut. Si les trois modèles donnent initialement d'excellentes performances, on constate en revanche que l'ajout d'une source de bruit non détectable perturbe complètement l'identification des deux modèles purement linéaires. Les résultats correspondants sont montrés figure 2.4. On y compare la capacité des modèles réduits à prévoir l'objectif, l'apprentissage ayant été fait en présence de la source additionnelle. Comme attendu, seul le modèle ARMAX garde d'excellentes

2.1. RÉSUMÉ DE L'ARTICLE

performances.

Enfin, des tests supplémentaires de robustesse sont réalisés. Dans un cas, on explore la sensibilité du modèle aux bruits de capteurs, et dans l'autre, on introduit des excitations d'amplitude plus élevée afin de provoquer l'apparition de non-linéarités dans l'écoulement. Dans les deux cas, le modèle révèle de très bonnes performances, montrant ainsi une bonne robustesse dans le processus d'identification proposé.

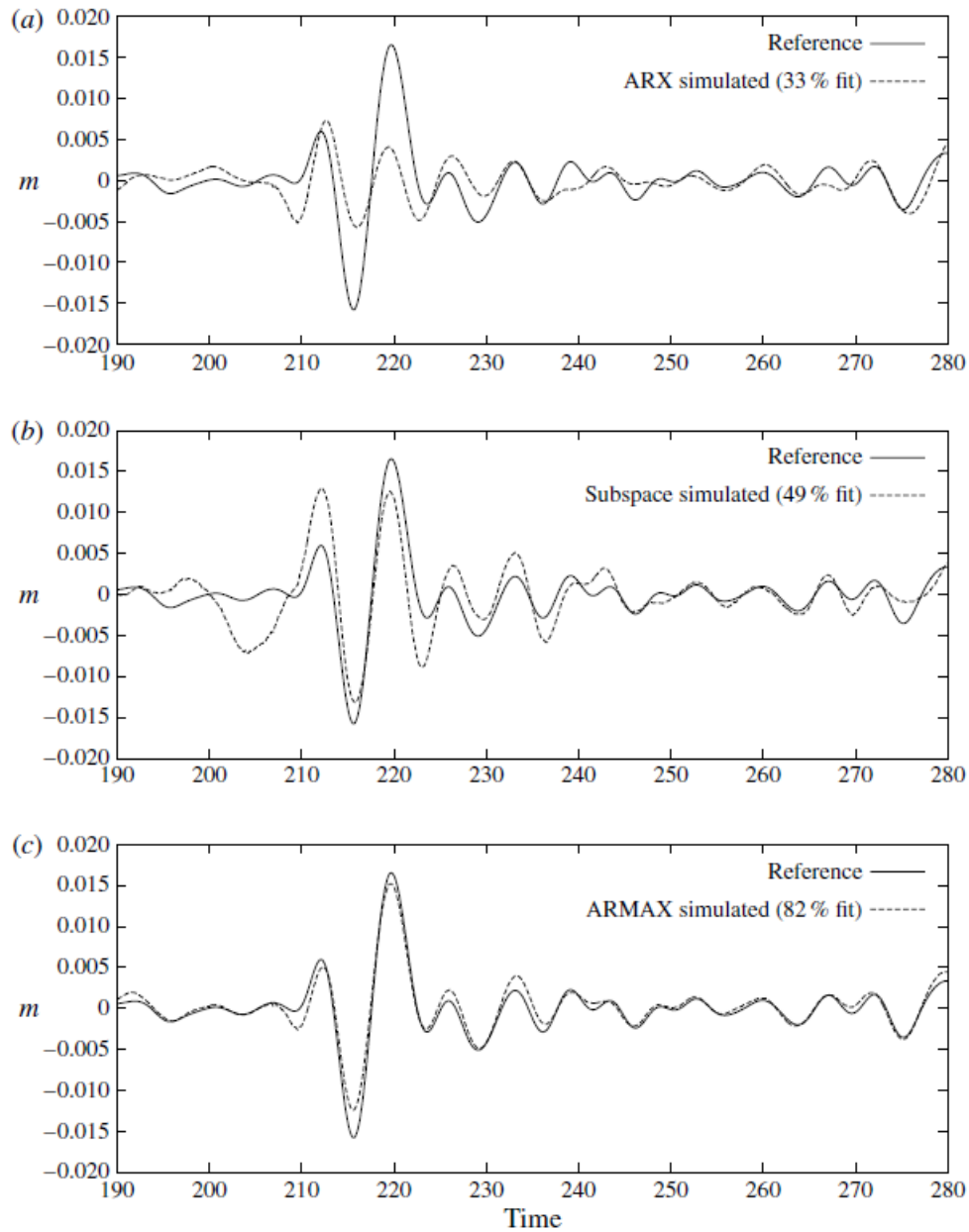


Figure 2.4 – Performances des modèles linéaires et ARMAX lorsque l’écoulement est soumis à une source non détectable d’excitations durant la phase d’identification du modèle. Seul le modèle ARMAX permet de conserver des performances correctes en présence d’un forçage non détecté.

A physics-based approach to flow control using system identification

Aurelien Hervé¹, Denis Sipp¹, Peter J. Schmid^{2†} and Manuel Samuelides³

¹ ONERA - The French Aerospace Lab, 8 rue des Vertugardins, 92190 Meudon, France

² Laboratoire d'Hydrodynamique (LadHyX), CNRS-Ecole Polytechnique, 91128 Palaiseau, France

³ ONERA - The French Aerospace Lab, 2 av. Edouard Belin, 31055 Toulouse, France

(Received 1 April 2011; revised 9 December 2011; accepted 23 February 2012)

Control of amplifier flows poses a great challenge, since the influence of environmental noise sources and measurement contamination is a crucial component in the design of models and the subsequent performance of the controller. A model-based approach that makes *a priori* assumptions on the noise characteristics often yields unsatisfactory results when the true noise environment is different from the assumed one. An alternative approach is proposed that consists of a data-based system-identification technique for modelling the flow; it avoids the model-based shortcomings by directly incorporating noise influences into an auto-regressive (ARMAX) design. This technique is applied to flow over a backward-facing step, a typical example of a noise-amplifier flow. Physical insight into the specifics of the flow is used to interpret and tailor the various terms of the auto-regressive model. The designed compensator shows an impressive performance as well as a remarkable robustness to increased noise levels and to off-design operating conditions. Owing to its reliance on only time-sequences of observable data, the proposed technique should be attractive in the design of control strategies directly from experimental data and should result in effective compensators that maintain performance in a realistic disturbance environment.

Key words: flow control

1. Introduction

It is generally acknowledged that the targeted manipulation of fluid flow holds great promise for a wide range of technological and industrial applications. The enhancement of mixing, the suppression of instabilities, increasing the robustness to uncertainty and noise, the reduction of drag and the improvement of energy conversion efficiencies are but a few objectives that could be reached by employing flow control techniques. For this reason, the discipline of flow control has seen a distinct and steady rise within the fluid dynamics community and has generated interest in academia and industry alike. The majority of successful flow control applications are numerical in nature, where the environmental conditions are favourable to the control strategy or can be managed easily. Less success must be reported for the application of control laws to a disturbance environment typically encountered in physical experiments.

† Email address for correspondence: peter@ladhyx.polytechnique.fr

The success or shortfall of control strategies depends on many factors, principally among them the nature of the inherent flow dynamics. Noise amplifiers which are highly sensitive to the external disturbance environment pose great challenges to the design process. In this case, sources of noise and inaccuracies have to be captured or modelled accurately, since they form the basis of the observed unsteadiness of the flow (Bagheri, Brandt & Henningson 2009). Noise amplifiers are ubiquitous in many engineering applications, such as separated flows, jets or boundary layers, to name a few. A quintessential and much-studied noise-amplifier flow is that over a backward-facing step of Barkley, Gomes & Henderson (2002) at $Re = 500$ where the unsteady behaviour originates from a bounded region of convective instability (Blackburn, Barkley & Sherwin 2008; Marquet *et al.* 2008).

Oscillator flows, on the other hand, are characterized by the presence of a global instability and are by nature insensitive to the ambient disturbance environment as well as to modelling inaccuracies. Suppression of global instabilities (e.g. von-Kármán vortex streets or the shear layer forming over an open cavity) within the linear regime thus puts markedly less stringent constraints on modelling the external disturbance environment (Cattafesta *et al.* 2003; Samimy *et al.* 2003, 2007; Barbagallo, Sipp & Schmid 2009; Ma, Ahuja & Rowley 2010; Sipp *et al.* 2010), but raises different issues related to nonlinear saturation of global instabilities. Besides the intrinsic flow behaviour, the control design approach further divides the techniques and strategies necessary for a successful manipulation of fluid flows. Two approaches have to be distinguished: a model-based approach and a system-identification approach. In the former, a model that accurately describes the flow behaviour is derived *a priori* from the known flow physics. While for simple to moderately complicated geometries and/or artificial disturbance environments this approach has been quite successful, modelling difficulties increasingly arise as the flow becomes more complex and the disturbance environment becomes more realistic. Moreover, coherent fluid structures such as proper orthogonal decomposition (POD) modes, global modes or balanced modes play an important role in the Galerkin-based model-reduction step of the flow design process (see Efe & Ozbay 2003; Rowley, Colonius & Murray 2004; Akervik *et al.* 2007; Barbagallo *et al.* 2009; Sipp *et al.* 2010). The alternative system-identification approach does not rely on a physical model, but rather establishes an approximate relation between input and output signals directly from their observations over time (Ljung 1999). In this sense, system identification is a data-based technique. In most applications of system-identified control design (see Huang & Kim 2008 for an application to flow separation control), the identification process is used as a black-box technique, i.e. with little regard to a proper motivation of its parameters or a physical interpretation of its outcome.

Independently of the chosen control design technique, a reduction of the prescribed or identified model is often necessary. For control applications, recent studies have conclusively shown that balanced modes yield efficient reduced-order models on which a controller can be based (Moore 1981; Rowley 2005; Barbagallo *et al.* 2009). A model can be computed directly from the projection of the governing equations onto a basis that uses snapshots of the flow (Rowley 2005; Barbagallo *et al.* 2009) or from a realization of the observed dynamics (Juang & Pappa 1985; Akers & Bernstein 1997; Gibson, Lee & Wu 2000; Ma *et al.* 2010). Both techniques will ultimately lead to the same reduced-order model, expressed on the balanced basis.

The aim of this study is the introduction of a system-identification technique to a flow control problem and its link with a classical model-based control design process for the effective manipulation of noise-amplifier flows. In particular, during

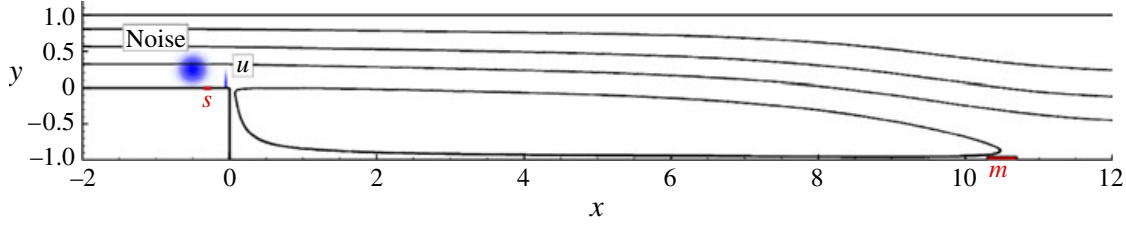


FIGURE 1. (Colour online available at journals.cambridge.org/fim) Sketch of flow geometry, including the different inputs and outputs. Two skin-friction measurements, s and m , are taken, respectively, at the top of the backward-facing step and at the end of the recirculation bubble. The control input u is given by the amplitude of actuation, composed of a spatial, Gaussian distribution of vertical velocity. The upstream forcing is introduced via a similar, spatially localized forcing, but with a stochastic amplitude w . The streamlines illustrate the mean flow \mathbf{v}_0 .

the identification phase we are interested in a rigorous interpretation of parameter choices and the physical understanding and role of various terms of the identified model.

We rely on linear systems theory that states that a model can be designed that recovers the perturbation dynamics from observable inputs. This model will furthermore benefit from the specifics of our configuration and control setup. A general equation with a physically motivated coefficient structure can thus be defined, and system identification techniques will determine these coefficients by a fitting algorithm to available data. Once the model is identified, a state-space optimal controller will be designed.

The article follows the following outline. The flow configuration and model equations are introduced in § 2, after which a brief review of classical Galerkin-based methods for the design of LQG-controllers is given, along with a general introduction of system identification (§ 3). This survey also addresses limitations of the Galerkin approach and helps motivate our alternative procedure. The design procedure of an ARMAX (auto-regressive moving-average exogenous) model based solely on observable data is presented in § 4; a physical interpretation of the model and its coefficients is given, before it is compared to the classical Galerkin-derived Kalman estimator. The subsequent control design process is the topic of § 5, where the compensator is designed, and applied to numerical simulations of the flow. The performance and robustness to noise of the compensator obtained are critically assessed. Conclusions and a summary of the most relevant results are offered in the final section (§ 6).

2. Configuration and governing equations

2.1. Noise amplifier over a backward-facing step

The configuration studied in this article consists of a two-dimensional backward-facing step that has previously been used, e.g. in Barkley *et al.* (2002). Variables are non-dimensionalized using the step height and the upstream centreline velocity; based on these values, the Reynolds number is chosen as $Re = 500$. The computational domain is taken as $(x, y) \in [-10, 50] \times [-1, 1]$ and is partially sketched in figure 1. The upstream boundary condition is modelled by an inflow of Poiseuille type; the upper and lower boundaries are set to wall conditions $\mathbf{v}_{tot} = 0$. For the chosen Reynolds number of $Re = 500$, the above flow configuration is globally stable. Nevertheless, the

flow exhibits a convective instability along the shear layer extending from the top of the step (at $x = 0$, location of branch I) to about $x = 25$ (branch II). As reported in Blackburn *et al.* (2008), the resulting flow unsteadiness is due to this local region of convective instability which is contained between upstream and downstream regions of stability. Even though a global stability analysis does not produce unstable global modes, transient growth of perturbations along the shear layer may arise due to the non-normality of the linearized Navier–Stokes operator. Generic fluid behaviour of this type is an example of a *noise amplifier*: a globally stable flow that still shows a significant, spatially localized response to an external disturbance environment.

The control of our flow configuration is aimed at reducing flow unsteadiness, which is quantified by the energy of the perturbations. As this energy is not easily observable in a real system, a skin-friction measurement m_{tot} is introduced at a downstream position. The sensor is located near the end of the first recirculation bubble at $x = 10.5$ (see figure 1), and $m_{tot}(t)$ will cease to fluctuate as the bubble is stabilized by our control effort. The fluctuating part of the measurement m_{tot} can therefore be taken as our control objective, which is to be minimized; it is then expected that the same control also reduces the global energy of the perturbations.

The external perturbations that will amplify along the shear layer and then impact on the objective m_{tot} originate within the upstream boundary layer. An upstream sensor s_{tot} is placed at $x = -0.3$ and will be used as an input to the compensator. If the sensor s_{tot} is sufficiently sensitive to the external perturbations, its measurements will provide important information about the effects of noise on the system.

For clarity, we introduce the notation of an underline denoting a quantity that is neither known nor measurable in a realistic environment. Generally speaking, a precise knowledge of the underlined quantities is required in a Galerkin-based model reduction approach while they will not be used during the control design process based on system identification.

We consider the dynamics of the flow field \mathbf{v}_{tot} driven by an external forcing term of the form $\underline{\mathbf{F}}_w w(t)$. This term stands for upstream unknown forcings which sustain unsteadiness in the flow field: $w(t)$ is a random forcing of standard deviation $\underline{\sigma}_w$ while $\underline{\mathbf{F}}_w$ is the spatial structure, which is of Gaussian shape

$$\underline{\mathbf{F}}_w(x, y) = \underline{\mathbf{A}} \exp\left(\frac{-(x - \underline{x}_0)^2}{2\underline{\sigma}_x^2}\right) \exp\left(\frac{-(y - \underline{y}_0)^2}{2\underline{\sigma}_y^2}\right). \quad (2.1)$$

The control action will be given by a term of the form $\underline{\mathbf{F}}_u u(t)$. The spatial structure $\underline{\mathbf{F}}_u$ consists of a similar Gaussian momentum forcing (although of smaller spatial extent) which is located at the top of the backward-facing step and driven by the scalar control law $u(t)$ which is yet to be determined. The control term will introduce a forcing at the upstream edge of the convectively unstable region; a small control should thus substantially affect the system and have a noticeable impact on the objective m_{tot} .

The spatial characteristics of both momentum forcing terms are defined by the coefficients in table 1; the momentum forcing terms are also sketched in figure 1. The velocity field expressed in Cartesian coordinates $\mathbf{v}_{tot} = [u_{tot} \ v_{tot}]^T$ is governed by the following non-dimensional equations:

$$\nabla \cdot \mathbf{v}_{tot} = 0, \quad (2.2a)$$

$$\partial_t \mathbf{v}_{tot} + \mathbf{v}_{tot} \cdot \nabla \mathbf{v}_{tot} = -\nabla p_{tot} + \frac{1}{Re} \Delta \mathbf{v}_{tot} + \underline{\mathbf{F}}_w w(t) + \underline{\mathbf{F}}_u u(t), \quad (2.2b)$$

	\underline{x}_0	\underline{y}_0	σ_x	σ_y	A
Noise	-0.5	0.25	0.1	0.1	4.0
Control	-0.05	0.01	0.01	0.1	4.0

TABLE 1. Parameters that define the spatial Gaussian distributions of the control and noise source.

$$s_{tot} = \int_{x=-0.35}^{x=-0.25} \partial_y v_{tot} dx, \quad m_{tot} = \int_{x=10.5}^{x=10.7} \partial_y v_{tot} dx. \quad (2.2c)$$

In the following, we will consider small noise amplitudes $\sigma_w \ll 1$. All quantities will fluctuate around their means, which will be denoted by a subscript zero. Let us explicitly introduce the fluctuations given by $\mathbf{v}_{tot} = \mathbf{v}_0 + \mathbf{v}$, $\mathbf{p}_{tot} = \mathbf{p}_0 + \mathbf{p}$, $m_{tot} = m_0 + m$ and $s_{tot} = s_0 + s$. Since the flow is a noise amplifier, the amplitude of all fluctuations \mathbf{v} , \mathbf{p} , m , s but also u scale with σ_w . The flow field \mathbf{v}_0 corresponds to a base flow, i.e. a steady solution of the nonlinear Navier–Stokes equations. After introducing these expressions into (2.2) the dominant order cancels out and we arrive at the following equations that govern the fluctuating part of the flow field:

$$\nabla \cdot \mathbf{v} = 0, \quad (2.3a)$$

$$\partial_t \mathbf{v} + \mathbf{v} \cdot \nabla \mathbf{v}_0 + \mathbf{v}_0 \cdot \nabla \mathbf{v} = -\nabla p + \frac{1}{Re} \Delta \mathbf{v} + \underline{\mathbf{F}_w} w(t) + \underline{\mathbf{F}_u} u(t). \quad (2.3b)$$

This shows that the dynamics of the fluctuations around the mean flow is linear. In particular, the dynamics from the inputs $(w(t), u(t))$ to the outputs $(s(t), m(t))$ is linear. In an experiment, m and s are straightforwardly obtained by subtracting the mean measurements m_0 and s_0 from the actual measurements m_{tot} and s_{tot} .

Even though the controller will be designed and optimized for operation within a linear regime, results in § 5.2.3 will show a remarkable robustness of the control law with respect to nonlinear effects. For the design process, external excitations should remain as low as possible so that the system stays in the linear regime; but one can still expect to obtain good results with the computed controller as one ventures beyond its design point. This feature will also play a role from an experimental point of view, where a small-amplitude environment is used to design the control law which will remain applicable, with reasonable results, in a less quiet setting.

2.2. Numerical method

We use a direct numerical simulation code which solves the nonlinear, incompressible Navier–Stokes equations (2.2) in primitive variables $(u_{tot}, v_{tot}, p_{tot})$. To increase accuracy for low-amplitude perturbations, the code is based on the perturbed form (2.3) of the governing equations but still includes the nonlinear term $(\mathbf{v} \cdot \nabla \mathbf{v})$. Finite elements with a mesh composed of triangular elements are used for the spatial discretization; for our case, the mesh contains about 123 000 triangles. The velocity fields are projected onto six-node triangular elements with quadratic interpolation (P2-elements), while the pressure field is discretized using three-node triangular elements with linear interpolation (P1-elements). The pressure field is obtained using the Uzawa algorithm, preconditioned by the Cahouet–Chabart method (Glowinski 2003). The temporal discretization is semi-implicit and based on a second-order

backward-differentiation scheme. We use the standard free-outflow condition

$$p\mathbf{n} - Re^{-1}\nabla\mathbf{u} \cdot \mathbf{n} = 0 \quad (2.4)$$

at the outlet of our computational domain.

3. System identification for control-oriented flow modelling

In this section the model reduction based on Galerkin projections will first be briefly discussed, to motivate the use of identification methods in the design of optimal control strategies. In particular, we will focus less on its practical application but more on its underlying assumptions and requirements during the design process. *System identification* will then be introduced, as an alternative approach to model flow dynamics.

3.1. Model-based methods: Galerkin projection

A common method to obtain a reduced-order model is based on Galerkin projection. It consists of projecting the linearized Navier–Stokes equations onto a prescribed (bi-orthogonal) basis which results in a reduced state–space equation. The model must accurately represent the input–output behaviour of the full system; this prerequisite is a crucial component for the choice of bases that are appropriate for a given control application. POD bases (Efe & Ozbay 2003; Rowley *et al.* 2004; Barbagallo *et al.* 2009, and many others) which describe the most energetic structures of the system, or balanced bases (Moore 1981; Rowley 2005) which focus directly on the input–output behaviour of the system, are most commonly used to project the equations.

The Galerkin projection provides a linear dynamical model that is commonly expressed in standard finite-dimensional time-invariant state–space form. Projection of equations (2.3) onto the chosen basis yields

$$\mathbf{X}(t+1) = \mathbf{AX}(t) + \mathbf{Bu}(t) + \mathbf{B}_w w(t), \quad (3.1a)$$

$$s(t) = \mathbf{C}_s \mathbf{X}(t) + g_m(t), \quad (3.1b)$$

$$m(t) = \mathbf{C}_m \mathbf{X}(t) + g_s(t). \quad (3.1c)$$

The variable \mathbf{X} is referred to as the state variable. It describes the amplitudes of the various spatial structures that have been taken as a projection basis. The plant noise, i.e. the random disturbance environment driving the state dynamics, is modelled by the term $\mathbf{B}_w w(t)$. It consists of the forcing source \mathbf{B}_w , which is driven by the stochastic scalar forcing term $w(t)$. The term \mathbf{B}_w captures the unknown external excitations that enter the system and stems from the projection of the spatial distribution \mathbf{F}_w of the forcing term onto the chosen basis. Analogously, the term $\mathbf{Bu}(t)$ stands for the actuation: \mathbf{B} is obtained by projection of \mathbf{F}_u onto the Galerkin basis. The quantity (g_m, g_s) represents the noise sources for each of the two measurements. The temporal standard deviations of these stochastic quantities are inherent to the sensors (they are not determined by the projection) and are referred to as $\text{std}(g_m) = \mathbf{G}_m$ and $\text{std}(g_s) = \mathbf{G}_s$. The two matrices \mathbf{B} and \mathbf{B}_w describe system inputs in the form of forcing terms; the matrices $\mathbf{C}_{s,m}$ represent the extraction of information from the flow via the sensors (\mathbf{C} takes information from the state \mathbf{X}). The individual components of \mathbf{C} therefore refer to measurements of the spatial structures of the projection basis.

A Galerkin projection usually yields a continuous-time format for the state–space system (3.1). For simplicity we have chosen to formulate it in a discrete-time format, with t as the time step index. The remainder of the article pertaining to identification methods, it is more naturally expressed in the discrete-time framework. Yet, one

should keep in mind the equivalence of the continuous and discrete frameworks due to a straightforward transformation (see Antoulas 2005, for details on the correspondence between discrete and continuous-time matrices).

A proper model should accurately capture the transfer behaviour of the linear system from the input variables (w, u) to the output variables (s, m). The effectiveness of the model relies on the ability of the chosen Galerkin basis (e.g. POD modes, balanced POD modes, etc.) to represent this input–output mapping – a difficult undertaking in the light of the fact that the noise environment w is generally not known to a sufficient degree of detail (Dergham, Sipp & Robinet 2011). For this reason, simplifying assumptions about w (such as e.g. assuming it is spatially located) have to be made during the design process (see e.g. Bagheri *et al.* 2009), and their adverse impact on the overall performance of the compensated system has to be acknowledged as a deficiency of Galerkin-based control design. We would like to stress at this point that in the subsequent analysis a forcing w in the form of white noise is not required. Yet, it covers the most general case as it generates time-coloured fluctuations in s and m , which are the only quantities that are processed during the identification phase; the noise term w , on the other hand, never enters the analysis and is merely used to generate the perturbations.

3.1.1. Kalman filter

Computing the control law requires real-time knowledge of $X(t)$ which is commonly not available under realistic conditions. For this reason, an estimator that uses only partial information of the system to estimate an approximate state \hat{X} is used in lieu of X . The Riccati equation for the estimator depends on $(\mathbf{A}, \mathbf{B}_w, \mathbf{C}_s)$ and the signal-to-noise ratio σ_w/\mathbf{G}_s . The better the sensor, the lower \mathbf{G}_s ; the higher σ_w/\mathbf{G}_s , the more accurate the estimator.

The estimator consists of a dynamical system that recaptures the effect of noise sources w from the measurement(s) (in our case, the signal s) via a Kalman filter \mathbf{L} . The dynamics of the system has to be known such that the unknown forcing terms and their action on the entire flow field can be estimated. If the perturbations are observable from the measurement s , the optimal estimator reads

$$\hat{X}(t+1) = \underbrace{(\mathbf{A} - \mathbf{LC}_s)}_{\mathbf{A}_e} \hat{X} + \mathbf{Bu} + \mathbf{Ls}, \quad (3.2a)$$

$$\hat{m} = \mathbf{C}_m \hat{X}. \quad (3.2b)$$

It statistically minimizes the error $\|\hat{X} - X\|_2$ (with \hat{X} as the estimated state) in order to provide an accurate prediction \hat{m} of the measurement m . Equation (3.2) illustrates that the effects of the stochastic field $\mathbf{B}_w w(t)$ are captured by processing the difference between the actual measurement s and the measurement $\mathbf{C}_s \hat{X}$ predicted by the model.

3.1.2. Assessment and limitations of Galerkin-based methods

Galerkin models are a popular choice for model reduction, owing to their ease of use in feedback applications, mathematical bounds on their convergence, and their link to physically relevant flow structures. But despite their widespread use, Galerkin-based methods for the computation of reduced-order models also suffer from notable limitations and drawbacks.

An accurate large-scale model of the state dynamics is required. The Galerkin projection requires that the flow dynamics is accurately represented by a physics-based model. The implementation of boundary conditions, the computation of the base flow,

the incorporation of turbulence effects via a model and the influence of neglected nonlinear effects have to be justified with due caution, and their influence on the final model has to be assessed carefully.

Observability of the basis is required. To accurately reproduce the input–output dynamics of the system, the projection basis has to be sufficiently observable. This requirement commonly necessitates the use of adjoint simulations to determine a balanced basis which, in turn, is mandatory for large-scale state models. If no adjoint simulations are at hand and only POD modes are used for the projection basis, then the resulting transfer function may only poorly reproduce the original one.

An explicit description of the actuator is difficult to obtain. To define \mathbf{B} , the spatial distribution $\underline{\mathbf{F}}_u$ of the actuator momentum forcing has to be known or estimated, which is problematic in any experimental application. If $\underline{\mathbf{F}}_u$ is not known, a technique discussed in Samimy *et al.* (2003) and Cattafesta *et al.* (2003) can be used. A Galerkin projection of the Navier–Stokes equations onto e.g. a POD basis then yields an autonomous set of ordinary differential equations. The influence of the external actuation hence appears implicitly which causes problems for the control design. In order to obtain an explicit description of the actuation, separation methods may be employed (see Efe & Ozbay 2003, for a complete description of the separation method) in addition to the reduced-order model computation.

A reduced-order model that accurately captures the influence of the upstream noise $w(t)$ on the state is difficult to obtain. To allow an accurate reduction of the dynamics, knowledge about the noise source is required when computing the reduction basis. In the absence of this knowledge, modelling assumptions have to be made (Bagheri *et al.* 2009; Dergham *et al.* 2011) or a full state-to-sensor mapping has to be determined. Either approach is problematic and has significant consequences for the overall performance and robustness of the compensator.

Statistical information about the external noise sources is necessary. The computation of the estimator (that is, the Kalman gain \mathbf{L}) requires at least an approximate knowledge of the spatial distribution of the external disturbance environment (\mathbf{F}_w). Since statistical properties of the external forcing are often unknown or difficult to obtain, the estimator will ultimately perform suboptimally, leading to disappointing results when applied under realistic (experimental) condition.

3.2. An alternative approach: system identification

In this article we propose and apply an algorithmic process for the design of a controller based on a low-dimensional model that only requires data which can readily be extracted, for example, from a real lab experiment. This process relies on techniques from *system identification*, which provides quantitative information about the system’s dynamics directly from its observation. System identification provides models that are particularly well-suited for control applications since, by design, the only dynamics that are taken into account are part of the observable input–output behaviour of the system.

3.2.1. Predicting the effect of the observable sources

In general, the physical inputs of the flow are the control u and an *a priori* unknown number of external forcing sources w_k . The sources, whose effect can be detected by s before they reach m , are referred to as *predictable*, whereas the sources, which impact on m without having been detected by s , are referred to as *unpredictable*. Assuming linear flow behaviour, the output measurement m is given as a linear combination of

influences stemming from those sources

$$m = f_u u + \sum_{\text{predictable } w_k} f_{w_k} w_k + \sum_{\text{unpredictable } w_k} f_{w_k} w_k. \quad (3.3)$$

For all predictable forcing sources, a model can then be derived that aims at estimating the future measurement m by using the upstream measurement s according to

$$m = f_u u + f_s s + E, \quad (3.4a)$$

$$E = \sum_{\text{unpredictable } w_k} f_{w_k} w_k. \quad (3.4b)$$

In effect, this approach anticipates the effect of the predictable sources w_k on m by measuring their effect on the upstream sensor s before reaching m . What is not measurable by s cannot be anticipated and is included in an error term E . If the effect of the predictable forcing sources is well-estimated, a control law can be computed to cancel their influence on the measurement m . This approach is consistent with the Galerkin state-space framework introduced in § 3.1, since (f_s, f_u) defines a model that is equivalent to the estimator (or Kalman filter) given in (3.2). In particular, we note that these models share the same inputs/outputs. It is however important to bear in mind that the identified transfer function f_u is related to (3.2) rather than (3.1), and is therefore based on the system matrix $(A - LC_s)$ rather than A .

The system-identification approach aims at modelling the (f_s, f_u) transfer functions by a direct observation of the flow behaviour whereas the classical Galerkin approach derives them from the Navier–Stokes equations. Even though the two approaches differ, both aim to ultimately represent the dynamics that relate the available input(s) to the output(s) of the system. As pointed out by Kim & Bewley (2007), those dynamics are the only ones needed for a control-oriented low-order model.

It is important to realize that the model error referred to above arises from the part of the flow dynamics that cannot be predicted by the upstream sensor s . Consequently, term E will generally not be white Gaussian noise. As most of the linear identification methods commonly determine a model by assuming the unobservable dynamics as white-noise perturbations, this fact will raise important modelling issues. Most identified linear models (such as e.g. the subspace or ARX models, used by Huang & Kim 2008) assume E as white noise; they are referred to as *purely linear* by Ljung (1999), as they solve a least-squares error problem to determine the dynamics of the model. In contrast, a *pseudo-linear* ARMAX model will be introduced in § 4.1. It consists of a linear equation, computed via a nonlinear algorithm, hence allowing modelling of E as time-coloured noise (without any *a priori* knowledge of the colour of this noise).

3.2.2. Pseudo-experimental setup

One aim of our study is the introduction and assessment of low-order control design based on system identification that is adoptable for later applications to physical experiments. In view of this goal we will treat our numerical experiments in a quasi-experimental setting and process only data that would be easily available or measurable in reality. We will therefore impose a few restrictions on the design process. We will not require exact or approximate information about generally unknown quantities and in particular about all underlined quantities – for example, the characteristics of the upstream noise environment ($\underline{\mathbf{F}}_w$, $\underline{\sigma}_w$) and the behaviour of the actuator ($\underline{\mathbf{F}}_u$). This is in stark contrast to a (model-based) Galerkin approach

which necessitates the approximation, estimation or modelling of the external noise environment and the details of the actuation process. In addition, following a typical setup in a laboratory experiment, we will assume that upstream noise sources are omnipresent during the design procedure. It is thus not possible to process information where e.g. the control is the only source of external forcing. Also, we will allow sensors s and m to be corrupted by white measurement noise characterized by the standard deviations \mathbf{G}_s and \mathbf{G}_m whose precise values will also be considered as unknown in the design process. Finally, when controlling the flow, continuous control laws will have to be used. Although an impulse response of a linear system would provide a complete description of its transfer function, we assume that such an excitation is experimentally not feasible to a sufficiently high degree of accuracy.

3.2.3. Limitations of system identification

Like any computational techniques, system identification suffers from limitations, and, for a fair comparison, we present some of the weaknesses associated with system-identification methods.

Nonlinearity. In contrast to model-based methods, system-identified linear models can present great challenges when nonlinearities are present. In our configuration, the identification is performed in a quiet environment that ensures linear dynamics. Once identified, the model can show remarkable performance when exposed to stronger perturbations (§ 5.2.3). However, the identification process has to be performed within a linear flow regime if satisfying results are to be obtained.

Stability. Most linear identification algorithms cannot guarantee stability of the resulting model, contrary to model-based linear systems. This issue becomes critical, if the system is excited by an unknown source that continuously affects the objective measurement. System identification may model such a sustained influence as an instability of the system, unaware of the fact that it stems from an unknown external excitation source. This matter will be investigated further in § 4.4 where such an additional forcing source will be considered. In contrast to *purely linear* models, a *pseudo-linear* model will be introduced in § 4.1 that ensures stability.

Objective functional. In contrast to a Galerkin-POD approach where the total energy of the flow can be estimated and taken as an objective function, system identification only allows the control of observable objectives. In this article we introduce a downstream sensor and presume that a successful reduction of the measured fluctuations will give rise to a proportional reduction of the global fluctuation energy. Such an assumption is, of course, not assured in general and needs to be verified *a posteriori*. Note also that, once the model is identified, the downstream measurement is no longer needed. The goal of the model/compensator is to predict and to cancel a detected perturbation before it reaches the downstream measurement. Owing to the convective nature of the flow, any information from downstream of the actuator is irrelevant since it is already out of reach of the controller. From an experimental point of view, this implies that the downstream sensor is only needed during the identification process. Unlike the upstream sensor, it does not have to be included in the controller.

Tuning the model. System identification can often require setting some parameters for the regression algorithm. Although these coefficients can be based on a physical interpretation (§ 4.1), it requires some insight to properly set them; the same is not necessary for the model-based approach.

4. ARMAX as a linear model to identify the backward-facing-step dynamics

In this section the ARMAX model will be presented. Its physical interpretations will be discussed in § 4.1, and it will be used to model the backward-facing step (§ 4.2), before it is finally compared to the model that can be derived from a classical Balanced-POD Galerkin framework (§ 4.3). To assess the effect of the unpredictable forcing sources (equation (3.3)) on the identification process, an additional source of excitations has been used in the flow computation. Its location is chosen so that it corrupts the m signal without affecting s , in order to identify the dynamics in the presence of dynamics that are non-observable by s , but time coloured (§ 4.4). The performance of the ARMAX model in the presence of the additional forcing source will be compared to the performance of purely linear models.

4.1. Introduction of the ARMAX model and its physical interpretation

An auto-regressive moving-average exogenous (ARMAX) model will be used to identify the transfer function of the system. We have

$$m(t) + \underbrace{\sum_{k=1}^{n_a} a_k m(t-k)}_{\text{auto-regressive}} = \underbrace{\sum_{k=n_{du}}^{n_{bu}+n_{du}} b_k^u u(t-k)}_{\text{exogenous 1}} + \underbrace{\sum_{k=n_{ds}}^{n_{bs}+n_{ds}} b_k^s s(t-k)}_{\text{exogenous 2}} + E(t), \quad (4.1a)$$

$$E(t) = \underbrace{\sum_{k=1}^{n_c} c_k e(t-k)}_{\text{moving average}} + e(t). \quad (4.1b)$$

The superscripts u, s in (4.1) allow to differentiate two different sequences of (b_k) coefficients and should not be confused with an exponentiation. The regression consists of finding the (a_k, b_k, c_k) coefficients, such that the residual $e(t)$ only contains white noise of minimal variance.

The following parameters play an important role in the ARMAX-model: n_a is the number of previous outputs on which the current output depends (the Auto-Regressive part); the parameters n_{du}, n_{ds} denote the number of input samples that pass before the input starts to affect the output (i.e. measuring delay). Setting $n_d > 0$ means that the inputs do not have an instantaneous effect on the measurement, which is the case for our configuration. The parameters n_{bu}, n_{bs} signify the number of previous inputs on which the current output depends (the eXogenous part). For each input i , $n_{bi} + n_{di}$ defines the truncation order of the transfer function $i \rightarrow y$, where y is defined in (4.5) below (and the delay n_d causes the first coefficients $b_k^i, k = 0, \dots, n_{di} - 1$, to vanish). Finally, n_c is used to model time-coloured noise (the Moving-Average part). This term will be further discussed in § 4.1.2.

4.1.1. Auto-regressive model

Equation (3.4a) involves two transfer functions that can be represented as

$$m(t) = \sum_{k=0}^{\infty} h_k \tilde{u}(t-k), \quad (4.2)$$

where

$$\tilde{u}(t) = \begin{bmatrix} u(t) \\ s(t) \end{bmatrix}. \quad (4.3)$$

The h_k coefficients are referred as the Markov parameters. They represent the impulse response of the system. When using the state-space Kalman estimator, these coefficients are defined as

$$h_k = \begin{bmatrix} \mathbf{C}_m \mathbf{A}_e^k \mathbf{B} & \mathbf{C}_m \mathbf{A}_e^k \mathbf{L} \end{bmatrix} \quad (4.4)$$

where \mathbf{C}_m , \mathbf{A}_e , \mathbf{L} are defined as in (3.2)

Since the dynamics of the model is stable, we have $\lim_{k \rightarrow \infty} h_k = 0$, and the transfer function can be approximated by truncating the h_k -sequence at some index N based on a given error bound ε , i.e. $|h_k| < \varepsilon$ for $k > N$. The minimum rank N for which the truncation gives accurate results can be rather high (especially for weakly damped systems) and requires the identification of a large number of Markov parameters. In an effort to reduce the number of parameters, an auto-regressive representation of the transfer function can be used as follows.

Since the measurement m stems from a continuous physical system dynamics, it is reasonable to assume a strong auto-correlation in time. Therefore, one can expect to find a set of coefficients $a_{k=1,n_a}$ that defines

$$y(t) = m(t) + \sum_{k=1}^{n_a} a_k m(t-k) \quad (4.5)$$

such that $|y(t)| \ll |m(t)|$ for all time. The variable y can be viewed as the residual of the auto-regression of m over n_a time steps; the stronger the auto-correlation of the signal m , the lower the residual norm $|y|$.

By defining the Markov parameters b_k of the transfer function $\tilde{u} \rightarrow y$ as

$$y(t) = \sum_{k=0}^{\infty} b_k \tilde{u}(t-k) \quad (4.6)$$

the relation $|y| \ll |m|$ together with (4.2) and (4.6) yields $|b_k| \ll |h_k|$ for all k , which means that the Markov parameters b_k converge towards zero faster than the original Markov parameters h_k do. It is thus possible to truncate the transfer function $\tilde{u} \rightarrow y$ at a lower order $N' < N$ without loss of accuracy. Equation (4.5) then yields

$$m(t) = - \sum_{k=1}^{n_a} a_k m(t-k) + \sum_{k=0}^{\infty} b_k \tilde{u}(t-k). \quad (4.7)$$

This expression is thus based on a significantly smaller set of coefficients (compared to the direct representation (4.2)) to describe the transfer function $\tilde{u} \rightarrow m$.

We observe that the representations (4.2) and (4.7) are mathematically equivalent. However, the truncation step for each of these sequences has different interpretations. Based on (4.2), a truncation at order N is equivalent to the statement that the system returns to its equilibrium state (the base flow) in N time steps after being excited by an impulse in \tilde{u} ; for a weakly damped noise amplifier, N can be large. When using the recursive equation (4.7), a truncation at order N' means that N' time steps are needed to describe how an impulse in \tilde{u} starts to disturb the flow. The remaining observed dynamics is described by the auto-regressive part and consists of a self-sustaining process. This latter description is more suited to our case, since we know that the dynamics arises from weakly damped self-sustained oscillations that are triggered by small upstream disturbances.

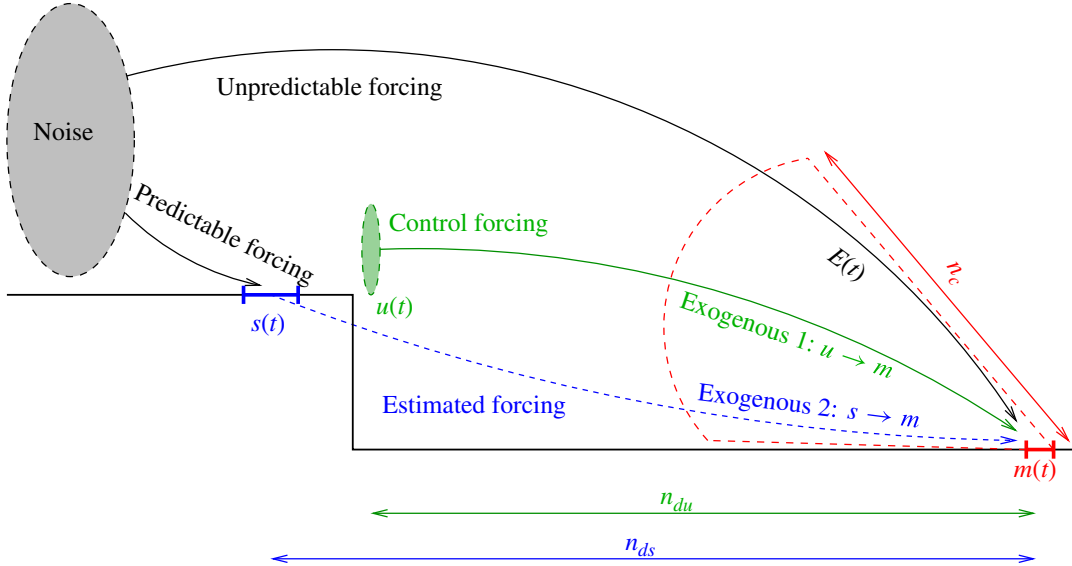


FIGURE 2. (Colour online) Schematic representation of the different terms and parameters in the ARMAX equation.

4.1.2. Exogenous and moving-average part

Figure 2 presents a sketch showing a physical interpretation of the ARMAX equation. The exogenous terms attempt to capture the effect of the two inputs on the output m , as shown by the arrows labelled Exogenous1 and Exogenous 2. As the inputs do not instantaneously affect the output, they are delayed using the (n_{du}, n_{ds}) coefficients which can be linked to the convective speed of the flow.

Although the upstream sensor s succeeds in acquiring useful information about the external excitations, it is not sufficient to observe the full external forcing. For this reason, dynamical characteristics that stem from non-observable (by s) excitations will pass through the system to eventually reach the output m . As such dynamics cannot be predicted by our model, its overall effect on the measurement m will be observed as measurement error $E(t)$. This error term contains the effects of advected and selectively amplified excitations; thus, the measurement noise cannot be modelled as white noise. Huang & Kim (2008) attempted to model a generic separated flow using an ARX equation, which represents a special case of our ARMAX equation with $n_c = 0$, i.e. with white-noise residuals. Not surprisingly, the ARX model showed poor results, attributed to lacking robustness to measurement noise. In contrast to the ARX model, the moving average part of the ARMAX equation allows us to model the measurement error as time-coloured Gaussian noise. This term is a key feature of our approach, as it ensures robustness against time-coloured noise that arises from unobservable (by s) forcing terms that propagated through the system.

Once the ARMAX equation has been determined to estimate m with sufficient accuracy, the downstream sensor m can be eliminated, as the model – and consequently the controller – will only use s and u as inputs.

4.2. Designing the model

4.2.1. DNS datasets for learning and testing

The coefficients in the ARMAX model are computed by first performing a direct numerical simulation (DNS) employing an arbitrary forcing law u . The DNS uses a time step of $dt_{dns} = 0.002$, and the time interval between measurement samples

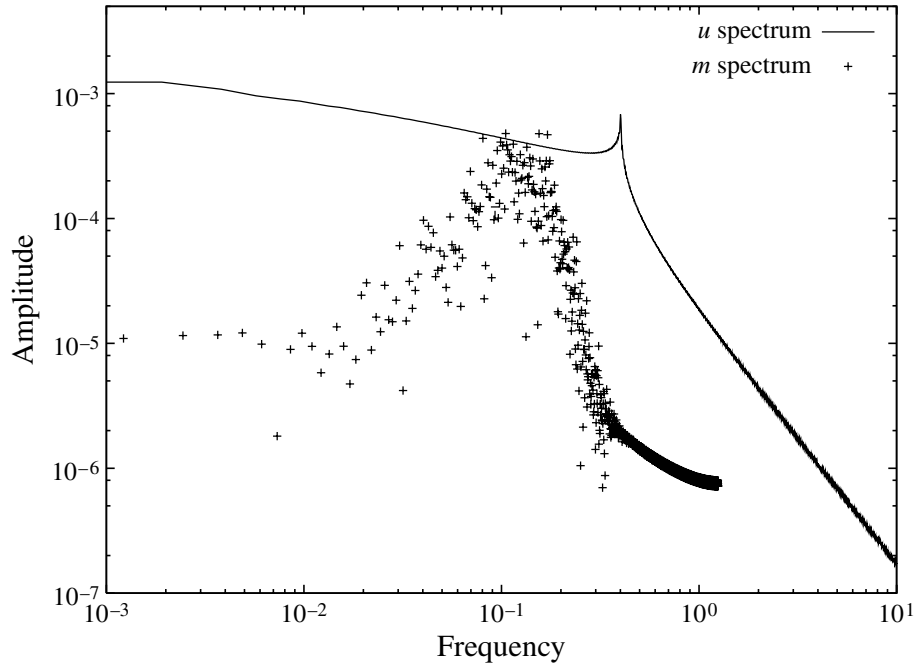


FIGURE 3. Comparison between the spectrum of the designed forcing signal u (taken for $t \in [0; 60]$ in figure 4b) and the spectrum of the measured signal m from an unforced, but noise-contaminated simulation.

is $dt_m = 0.1$. A (changing) pseudo-random noise is always introduced in the numerical simulations, which mimics upstream excitations of unknown source and distribution (as they are present in physical experiments). Unless otherwise stated, we will use in the following a low-amplitude forcing $\underline{\sigma}_w = 0.01$, which ensures that the perturbations behave linearly, and perfect sensors characterized by $\mathbf{G}_s = \mathbf{G}_m = 0$.

The spectrum of the measurement $m(t)$ for the case of an unforced simulation (i.e. with $u = 0$, but with upstream excitations present) is plotted in figure 3 (crosses). It demonstrates that the bulk of the excited frequencies are located between 10^{-2} and 0.2 . We thus can assume that most of the flow dynamics can be excited by using a forcing law u that covers this frequency band. Figure 4 shows three signals, s , u , and m , that have been used as a learning dataset to identify the model. Of the three signals, s and m are not given *a priori* but are extracted from the DNS. The control law u is continuous in time (as required by an actuator in a real experiment) and designed to allow the simultaneous identification of the action of both u and s on the measurement m : the peaks in u trigger a similar but delayed response in m , while between the peaks (where the action of u is rather weak, e.g. from $t = 40$ to $t = 60$) the response of m to s can be identified. For comparison, the spectrum of the chosen forcing u is given in figure 3. The maximum amplitude of the forcing u has to be chosen such that its triggered response can be easily identified over the noisy perturbations; at the same time, it is limited by the fact that triggered nonlinear effects are undesirable for the identification process. A few representative snapshots of the perturbation vorticity are displayed in figure 5. It clearly illustrates transient spatial growth (from $x = 0$ to $x = 25$) arising from the forcing followed by exponential decay (for $x > 25$).

Two additional test datasets have been used (as shown in figure 6 and figure 7) to check if the identified model is able to reproduce the dynamics of m for different datasets. These two datasets provide a broader range of conditions to which the flow and the model are being exposed. Figure 6 shows the same control law u as the one

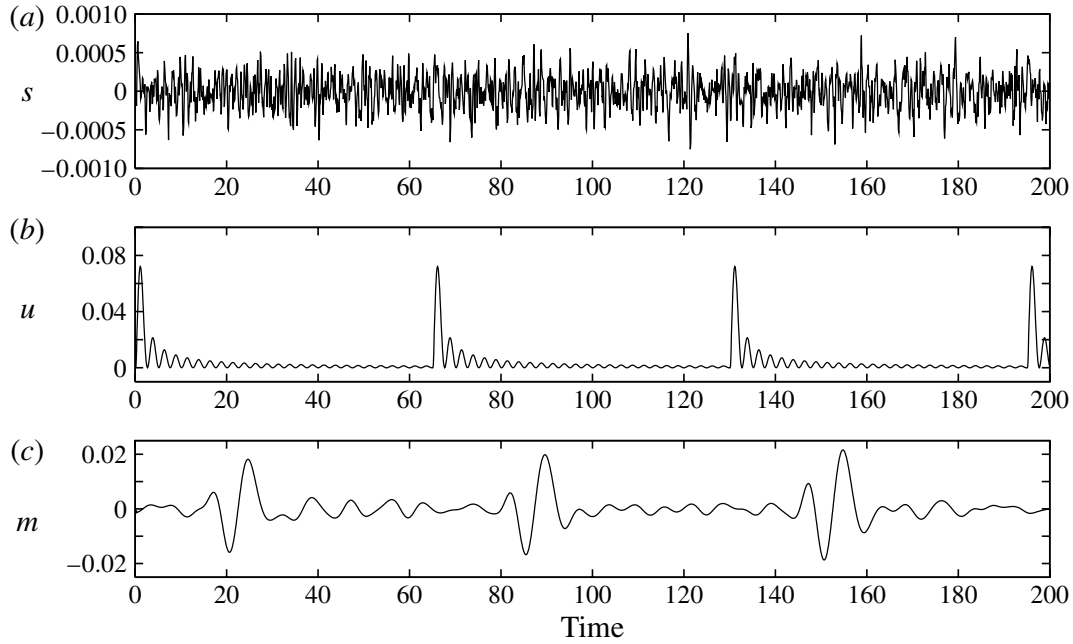


FIGURE 4. Three data sequences, used to identify the model: (a) the measurement s capturing the influence of external noise, (b) a deterministic, broadband control law u , (c) the measurement m taken near the reattachment point.

used in the previous dataset, whereas the upstream measurement s is subjected to a different noise source. This test is to ensure that the influence of u and s on m are identified independently. Figure 7 shows a different control law which corresponds to a step followed by an arbitrary combination of a small number of sinusoidal functions.

4.2.2. Choosing the ARMAX coefficients

The ARMAX regression introduced above requires the selection of the following coefficients: n_a , n_{bu} , n_{bs} , n_{du} , n_{ds} , and n_c . As explained in § 4.1.2, these coefficients are related to various properties of the flow and can thus be easily set. They should improve the regression efficiency but do not have to be defined precisely. In addition, the more data that are available for the identification process, the less important the exact values of these coefficients become.

In determining n_a , an auto-correlation of $m(t)$ has been calculated using one of the above datasets. Results are shown in figure 8(a): the solid curve corresponds to the auto-correlation. Owing to the short dataset, the auto-correlation should not be assumed as fully converged. Nevertheless, the correlation shows a quasi-oscillatory behaviour. We set $n_a = 36$ (indicated by the grey zone in figure 8a) which approximately corresponds to half this oscillation period.

The time delays n_{du}, n_{ds} can be obtained by considering the cross-correlations between $[u(t)s(t)]$ and $m(t)$. Figure 8(b) displays the cross-correlation between u and m ; it shows that the influence of u is felt at the measurement location at $t \approx 11$. It was significantly more difficult to reach convergence of the cross-correlation between s and m , since the spectrum of s is substantially closer to a flat white-noise spectrum. An experimental setup would probably provide substantially longer datasets. This would allow us to determine these correlations with enough accuracy. In our study, however, we chose to evaluate the convective time scale of the flow in a different way. We note that the evaluation of n_{du}, n_{ds} can also be derived from an estimation of the convective speed of the flow. The convective speed of perturbations is approximately

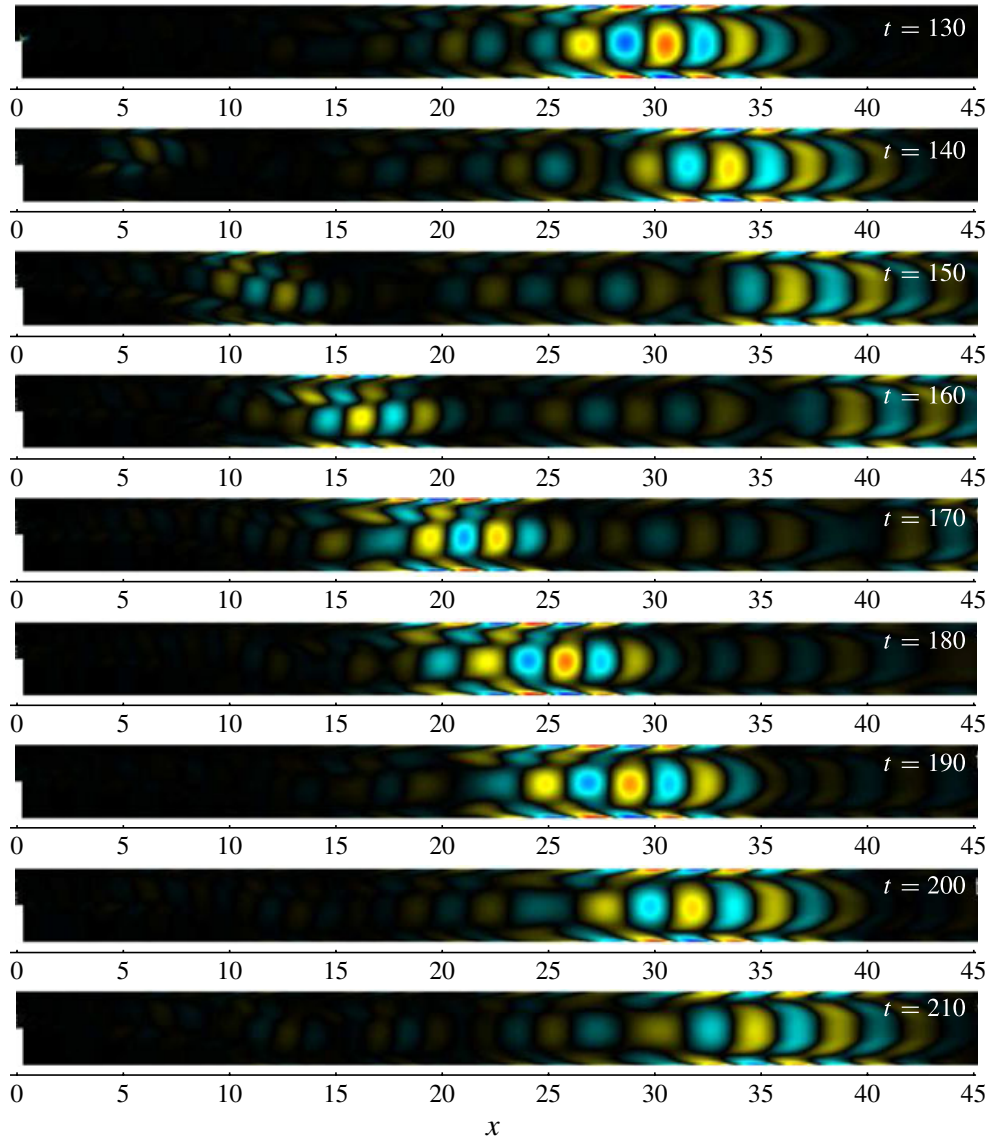


FIGURE 5. Contours of the perturbation vorticity for the simulation that produced the dataset in figure 4. The control (visible at $t = 130$) creates a wave packet that is spatially amplified between $x = 0$ and $x = 25$ before it exponentially decays. The effect of the control peak at $t \approx 70$ is still visible at $t = 130$ when the second control peak occurs. Between the two triggered wave packets, additional perturbations are visible which can be ascribed to excitations from the upstream noise.

given by the time until a particle released at the locations of s and u reaches the sensor location of m . Integrating a numerical simulation with passive particles, or simply the base-flow equations, will lead to the same results, as small perturbations will not significantly affect the convective speed of the flow. Since it is acceptable to underestimate the delays, but not to overestimate them, the fastest particle (initially located at the centreline position) is taken as a reference. Figure 9 shows different streamlines of the base flow, with passive particles being integrated from the actuator location (a) for determining n_{du} and the sensor location (b) for determining n_{ds} . It takes, respectively, about 11.4 and 12.2 time units for the fastest particles released at the control and sensor location to reach m ; for this reason, n_{du} and n_{ds} are set to the corresponding values of $n_{du} = 114$ and $n_{ds} = 122$ (since $dt_m = 0.1$). The n_{du} coefficient

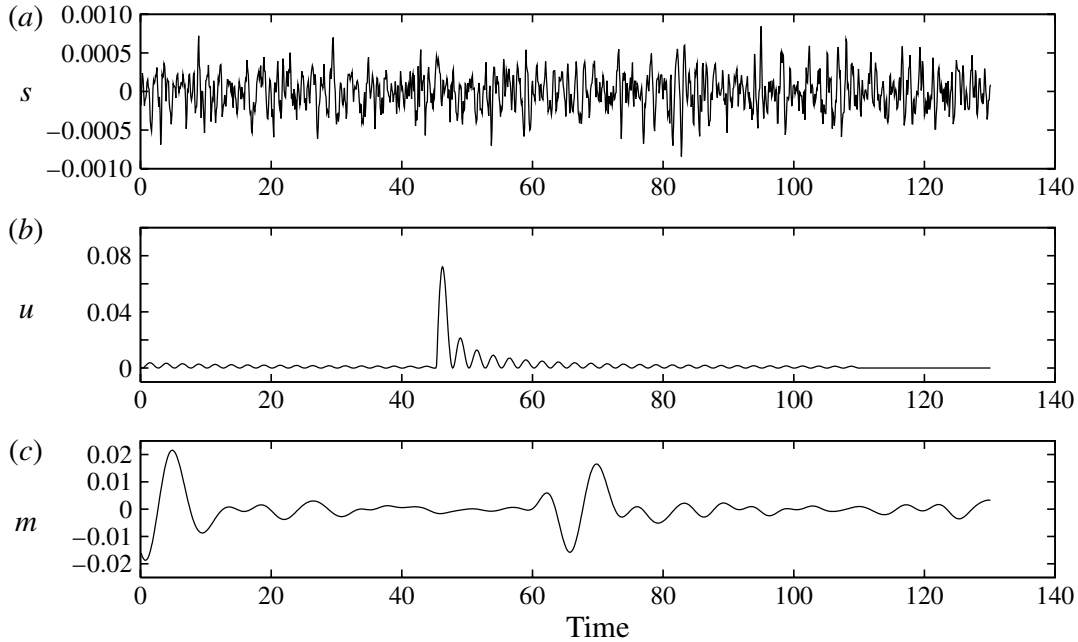


FIGURE 6. Three alternative data sequences, that define the first testing dataset (a) the measurement s capturing the influence of external noise, (b) a deterministic, broadband control law u , (c) the measurement m taken near the reattachment point.

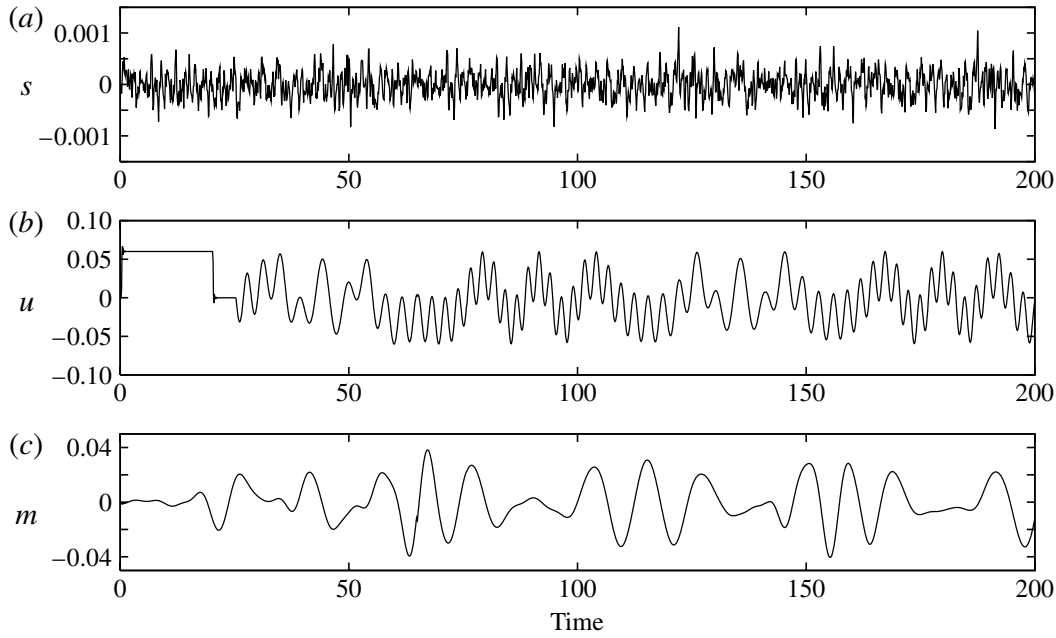


FIGURE 7. Three alternative data sequences, that define the second testing dataset (a) the measurement s capturing the influence of external noise, (b) a deterministic, broadband control law u , (c) the measurement m taken near the reattachment point.

is consistent with the value we found by evaluating the cross-correlation between u and m .

The coefficient n_{bu} is set to 49 such that the first visible peak in figure 8(b) is captured. We therefore set $n_{bs} = n_{bu} = 49$. Numerical tests revealed that the model showed little sensitivity to variations in the coefficients $[n_{bu}, n_{bs}]$. The grey zone

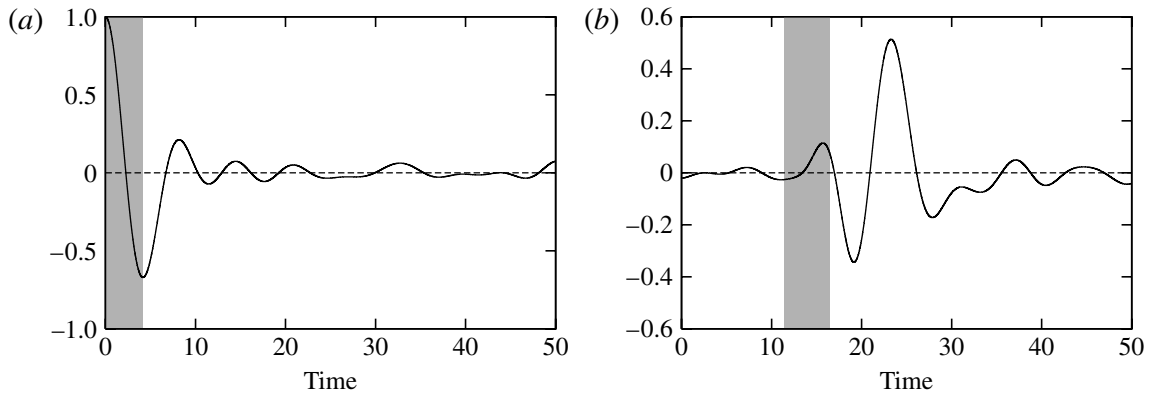


FIGURE 8. Correlations between temporal signals: (a) auto-correlation of m and (b) cross-correlation between u and m . The shaded area indicates the window length that is relevant for the proper performance of the auto-regressive model.

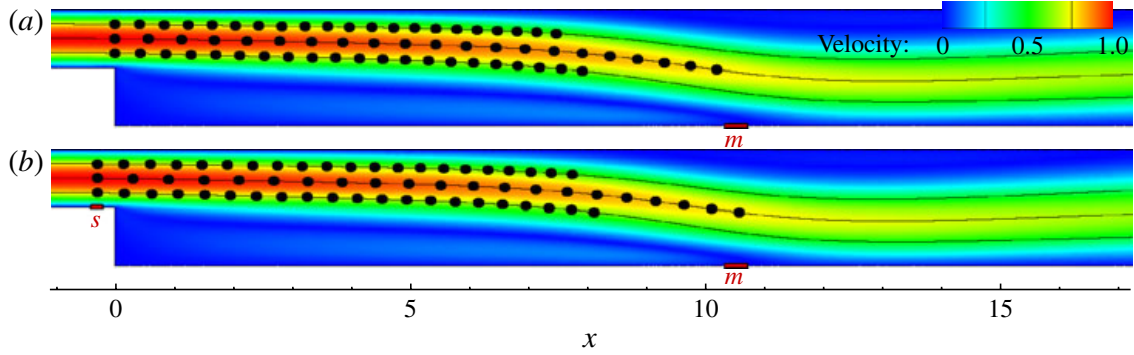


FIGURE 9. Motion along the base flow streamlines. (a) from $t = 0$ to $t = 11.4$, starting at the location of the controller. (b) $t = 0$ to $t = 12.2$, starting at the location of the upstream sensor. The contours are coloured according to the base flow velocity.

in figure 8(b) is bounded by $t/dt_m = [n_{du}; n_u]$. We recall that it is not necessary to increase n_{bu} in order to obtain an efficient model; a signal that is sufficiently auto-correlated can be represented with only a few coefficients b_k by using an auto-regressive equation (see the arguments in § 4.1.1). The chosen grey zone contains the first arrival of information from u in the measurement m . An alternative, direct identification of the Markov parameters (that is, by setting $n_a = 0$) is conceivable but, in this case, the coefficient n_u should be set to at least $n_u = 300$. This value stems from the approximate support of the signal in figure 8(b), yielding a state-space model more than doubled in size. This exercise highlights the importance of the auto-regressive part of the model which is able to capture the dynamics in a far more compact manner.

Finally, the coefficient n_c can simply be chosen by evaluating various models once the remaining coefficients have been determined. By increasing n_c from 0 to 20, an optimal value at $n_c = 9$ has been found that resulted in very satisfactory results.

In summary, the selected values for the ARMAX coefficients can be found in table 2.

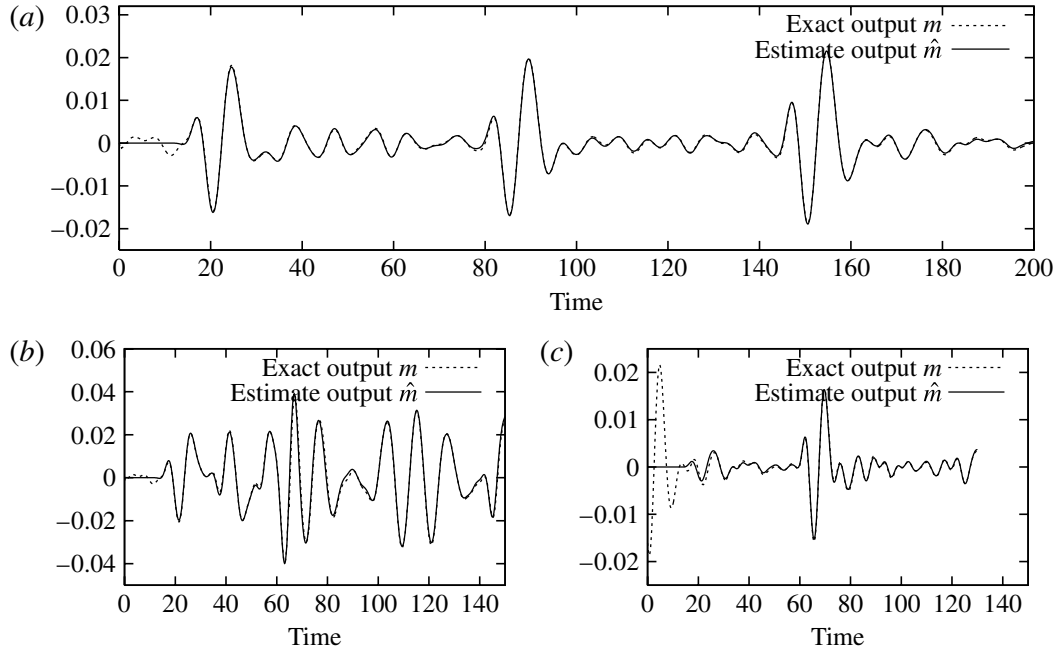


FIGURE 10. Performance of the system-identified model ARMAX_0 compared to DNS measurements. The ARMAX model starts from the zero state, and results are compared to the DNS dataset: (a) learning dataset; (b) validation dataset 1; (c) validation dataset 2.

n_a	n_{bu}	n_{bs}	n_{du}	n_{ds}	n_c
36	49	49	114	122	9

TABLE 2. Choice of coefficient values for the ARMAX model.

4.2.3. Identification algorithm

The computation of an ARMAX model (with $n_c > 0$) involves an iterative algorithm. Owing to the non-white-in-time error term E , the algorithm can ensure stability by modelling the unpredictable dynamics as the error. We used the MatLab routine `armax` to compute the model; more details about the algorithm can be found in Ljung (1999).

4.2.4. Model performance

Figure 10 illustrates the performance of the system-identified ARMAX model, in particular its accuracy in reproducing the output m for the three datasets displayed in figures 4, 6 and 7. The model is based on the ARMAX equation (4.1), whose coefficients are listed in table 2. In what follows, this model will be referred to as ARMAX_0 ; it estimates the output m from the inputs u and s . The identified model is initialized with a zero state vector (which explains the vanishing values for $t \in [0, 11.4] = [0, n_{du}]dt_m$) and is only driven by (s, u) to provide an estimate for m . The output of the model is compared to the measurement m from DNS: the model is able to predict the output with very high accuracy, which validates both the relevance of the model equation (4.1) and the implementation of the s -sensor to provide important information to the model.

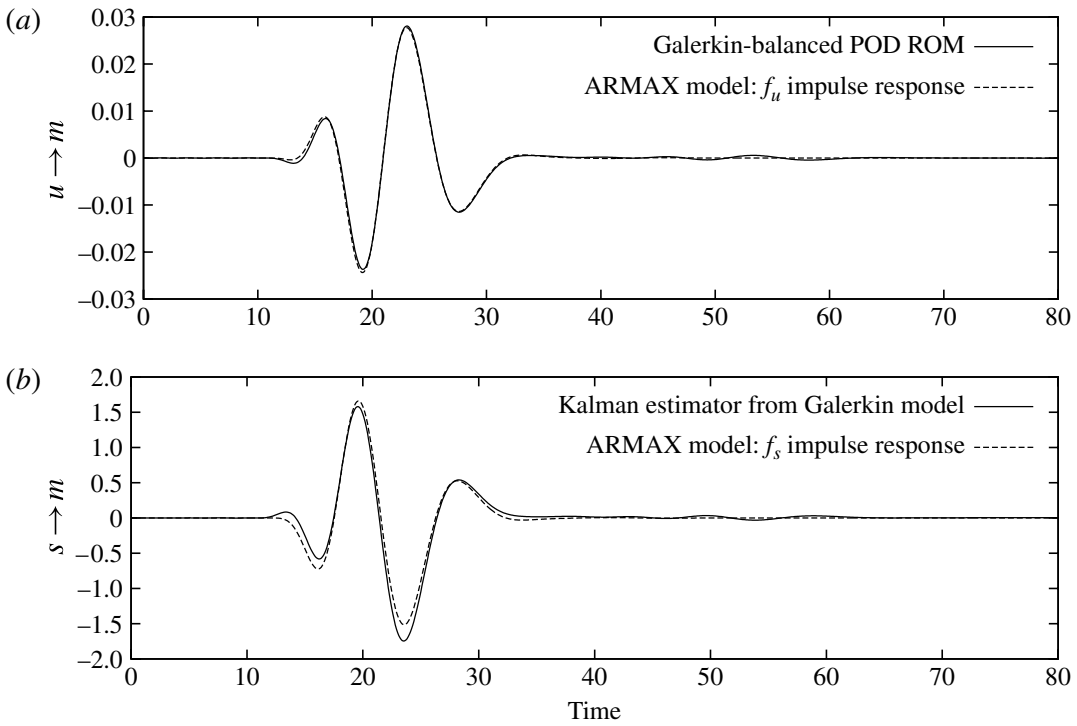


FIGURE 11. Galerkin-based ROM versus ARMAX impulse responses. (a) From u to m .
(b) From s to m .

4.3. Comparison between Galerkin-POD and ARMAX model

For the sake of completeness, a comparison between the identified model and a Galerkin-based model is presented. As mentioned in § 3, both the Galerkin-based Kalman filter (3.2) and the system-identified model (4.1) aim at presenting the output m as a function of the two inputs u and s . In addition, both models are linear and can thus be compared using their respective impulse response. To this end, we computed a Galerkin reduced-order model, taking advantage of full knowledge of our numerical system (note that the computation of the Galerkin ROM cannot be performed within the pseudo-experimental setup introduced in § 3.2.2).

We proceeded as described in Rowley (2005). First, two snapshot sequences for the impulse responses of the direct equations starting with an impulse in u , and w are computed which are then used to determine a balanced-POD basis that was thereafter truncated to contain 23 modes. The Navier–Stokes equations are then projected onto this truncated basis. A Kalman estimator is then computed to estimate the state from upstream measurements s . As we do not consider sensor noise in this section, the Kalman filter is computed in the large-gain limit (which is equivalent to assuming $\text{var}(w) \gg \text{var}(g_s)$ in (3.1)). Solving an algebraic Riccati equation finally provides the Kalman filter (3.2), whose transfer functions correspond to (f_u, f_s) .

The Kalman estimator is known to be the optimal linear system that predicts the output measurement m given the inputs (u, s) . One can therefore expect the transfer functions of such a model to match the transfer functions obtained via ARMAX identification. Comparing the impulse response of different systems is therefore an appropriate test as it is independent of the chosen basis and the particular formulation of the model (state-space form or polynomial representation of the transfer function).

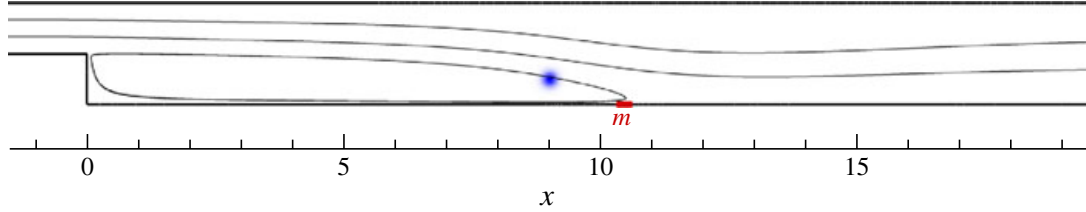


FIGURE 12. (Colour online) Additional source of noise. A Gaussian momentum forcing is located in the shear layer, near the end of the recirculation bubble so that it generates structures that impact on m but not s .

	\underline{x}_0	\underline{y}_0	$\underline{\sigma}_x$	$\underline{\sigma}_y$	A
Additional noise	9	-0.5	0.1	0.1	7.2

TABLE 3. Parameters that define the spatial Gaussian distributions of the new noise source. It is located in the shear layer, near the end of the recirculation bubble so that it will create structures that impact on m but not s .

Figure 11 shows a comparison of the impulse responses that have been obtained using the Galerkin framework and using the ARMAX identification technique. It shows a remarkable correspondence between the two models, which again corroborates the ability of the chosen system-identification technique to capture the relevant flow dynamics.

4.4. Robustness of the ARMAX model with respect to non-predictable forcing sources

In a realistic environment, the external disturbances may arise from multiple locations, and some of them may not be observable by the upstream sensor. Nevertheless, they can influence the output m and consequently disturb the identification process. In this section we investigate the effects of such perturbations on the identification process.

To highlight the properties of the ARMAX model, the results will be compared with those of purely linear models: an ARX model and a subspace model. The ARX model represents a special case of an ARMAX model with $n_c = 0$, whereas the subspace model is obtained as described in Huang & Kim (2008), with a dimension of 120. To model an unknown external excitation that impacts on the downstream sensor m without being observable by s , a new random forcing source is added to the flow: it is located in the shear layer, near the end of the recirculation bubble, so that it will impact on m without being detected by s . Figure 12 shows the precise location of the additional forcing source; numerically, it is modelled as a momentum forcing, similarly to the main forcing source (the coefficients are given in table 3).

In such a configuration, the downstream sensor measures the combination of *predictable dynamics* (by s) that arise from the main forcing source and *unpredictable dynamics* that arise from the new forcing source. Ideally, the identified model should treat the unpredictable dynamics as the model error $E(t)$ (as introduced in § 3.2). In other words, it should ignore it and, rather, focus on the predictable dynamics whose effects can be cancelled by the controller. As far the controller is concerned, the objective is to attenuate the predictable noise, since the unpredictable part is out of reach.

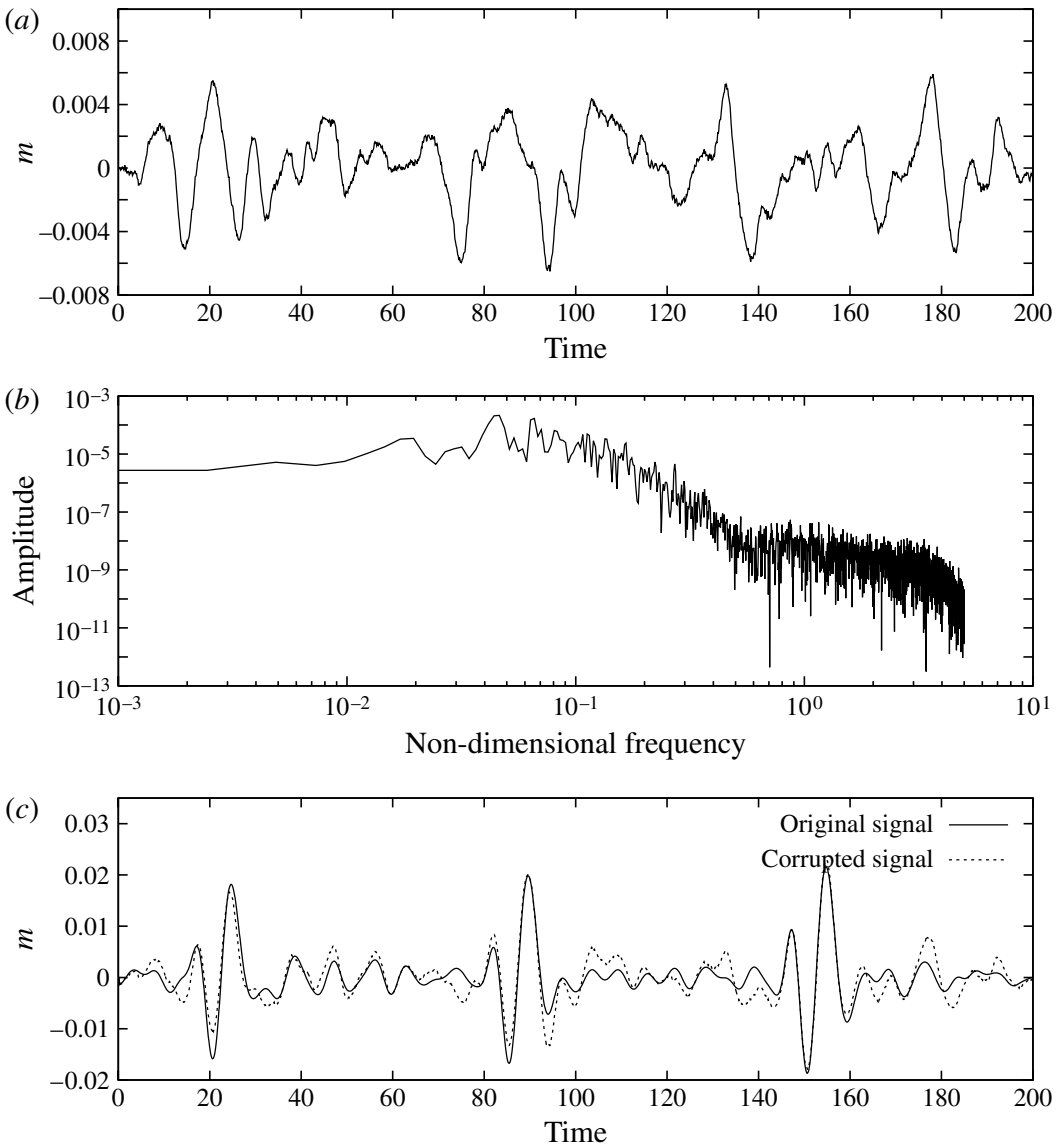


FIGURE 13. Additional source of noise: (a) signal generated by the additional forcing source alone; (b) periodogram of the perturbation signal; (c) resulting corrupted output signal, compared to the original (uncontaminated) signal.

As previously mentioned (see § 4.1.2), most linear system-identification techniques treat the model error as white noise; the ARMAX equation differs in this respect by allowing time-coloured noise. This additional feature is critically important in this study: the model error is certainly time coloured since it corresponds to physical structures that do not affect s but are nonetheless advected and filtered by the flow until they eventually reach the sensor m .

Figure 13 displays the additional measurement (a), its power spectrum (b), as well as the resulting corrupted learning dataset (c). In figure 13(b) one can clearly see that the high frequencies are filtered by the flow before the excitations affect the output measurement. The standard deviation of the perturbation signal (figure 13a) is equal to 44 % of the standard deviation of the original signal. New models are then obtained based on the corrupted dataset of figure 13(c). This is followed by simulations using the validation dataset of figure 6, which has not been corrupted by the

Presence of additional external forcing source:	No (%)	Yes (%)	Relative loss (%)
ARMAX fit	96	82	15
ARX fit	72	33	41
Subspace fit	95	49	48
Relative improvement from ARX to ARMAX	32	148	

TABLE 4. Influence of an additional external forcing on the ARX, subspace, and ARMAX model performance. While the ARMAX identification remains accurate in the presence of unpredictable forcing sources, the purely linear ARX and subspace models show a significant loss in performance.

additional forcing source; it is thus possible to compare the results obtained to those in § 4.2.4.

For a quantitative comparison, we use as a criterion the fraction of the output variation that is captured by each model. We introduce

$$\text{fit} = 1 - \frac{\|m_{\text{simulated}} - m_{\text{ref}}\|}{\|m_{\text{ref}} - \text{mean}(m_{\text{ref}})\|}. \quad (4.8)$$

For the regression of the ARX and ARMAX models, we use the same coefficients as those given in table 2, except for n_c . Owing to the dependence of the ARMAX model on the properties of the unpredictable noise, the value of n_c had to be adjusted. As in § 4.2.2, n_c has been varied from 0 to 20, and best results have been obtained for $n_c = 17$.

Figure 14 depicts the performance of the ARX, subspace, and ARMAX models in recovering the (clean) validation dataset, with an additional source of noise having been present during the identification process. Both purely linear models show inferior performance, while the ARMAX model performs well in predicting both the control peak response and the subsequent dynamics. Quantitative results are given in table 4. For comparison, we also conducted tests using the initial (uncorrupted) learning dataset of figure 4 during the identification process; results are also given in table 4 (column headed No). In the presence of *mostly predictable* dynamics, the ARX performance is significantly lower than the subspace model performance; the latter is comparable to ARMAX. This is consistent with the results of Huang & Kim (2008) where the subspace model showed better performance than the ARX model. On the other hand, both purely linear models suffer a severe loss in performance when the identification processes are afflicted by unpredictable time-coloured noise. The ARMAX model, on the other hand, fared significantly better, which underlines the importance of the moving-average component of the model to cope with unpredictable dynamics in the flow.

5. Feed-forward control

In this section, we build a compensator based on the ARMAX_0 model. It consists of a dynamical linear system that is designed to compute an optimal control law u from the measured signal s . The objective of the controller is to minimize the quadratic norm of the measurement m . The control design is detailed in § 5.1, before the compensator is used to control the direct numerical simulation in § 5.2.

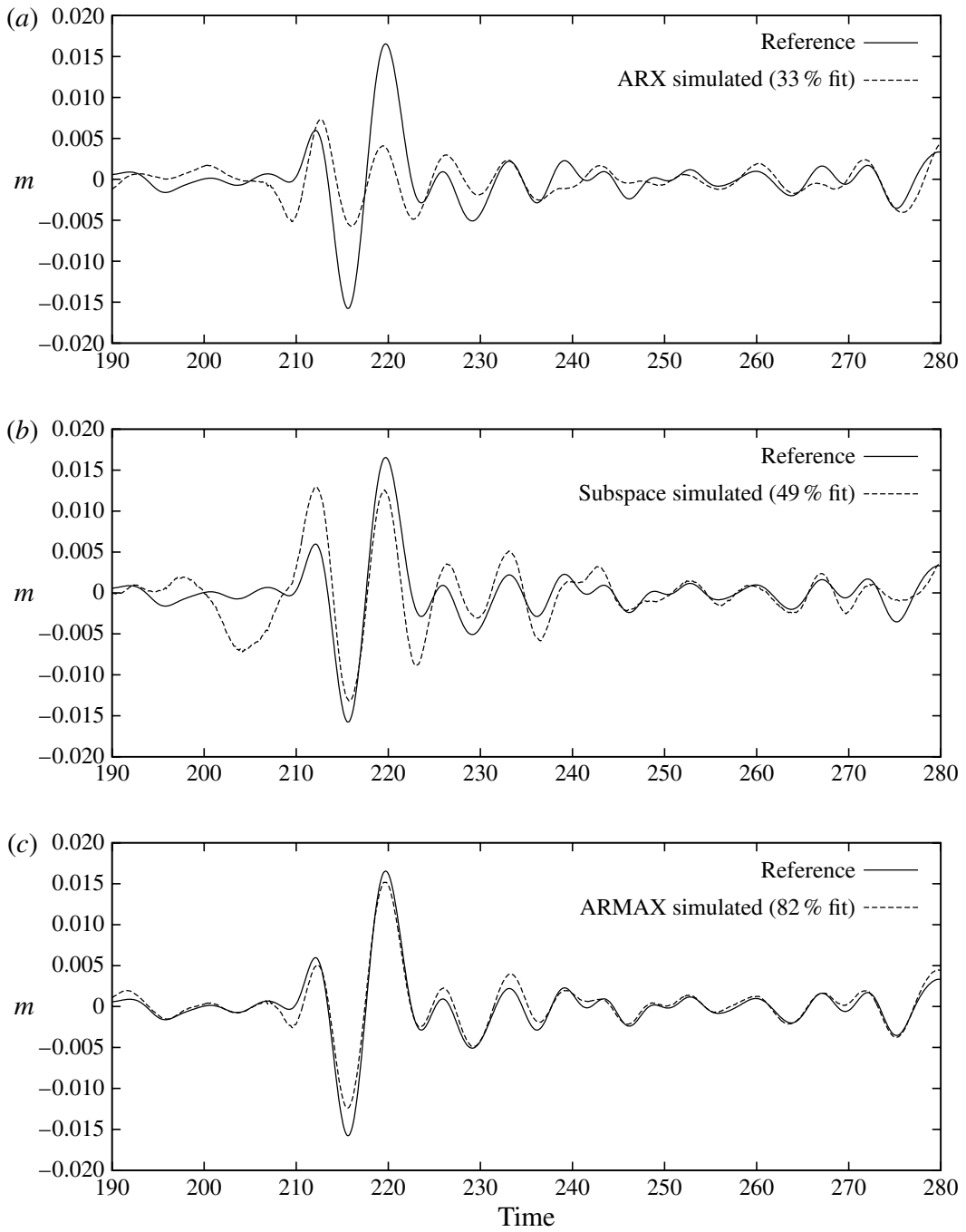


FIGURE 14. Comparison of the performance of (a) ARX, (b) subspace and (c) ARMAX models to recover the validation dataset. The models were identified in the presence of an unpredictable noise source. Both purely linear models are substantially affected by the presence of time-coloured noise, and do not provide accurate estimations of the signal. The ARMAX model, on the other hand, remains accurate despite a small loss in performance. Note that the fit coefficient, defined in (4.8), has been computed using a longer simulation.

5.1. Control design

Considering (3.4a), together with the objective to minimize $\|m\|$, the control law may formally be written as

$$u = -f_u^{-1} f_s s. \quad (5.1)$$

In practice, f_u cannot be properly inverted, and a pseudo-inverse has to be used. This consists of finding a control vector that minimizes the prediction of the output m , from t to $t + T$ where T defines the control horizon (whose value will be set below).

5.1.1. Designing the compensator dynamics

Using the impulse responses f_u and f_s displayed in figure 11, one can construct the two Markov sequences defined in (4.2). Figure 11 shows that both impulse responses eventually converge towards zero, which justifies our assumption of $h_{k>500=N_0} = 0$ (the index N_0 corresponds to a time $t = 50$). For an arbitrary discrete-time control horizon $T > N_0$, the output measurement vector \mathbf{M}_T that results from a combination of a past control vector \mathbf{U}^p , a future control vector \mathbf{U}^f and a past measurement vector \mathbf{S}^p reads

$$\begin{aligned} \begin{pmatrix} m_t \\ m_{t+1} \\ \vdots \\ m_{t+T} \end{pmatrix} &= \underbrace{\begin{pmatrix} h_0^u & & & \\ h_1^u & h_0^u & & \\ \dots & \dots & \ddots & \\ h_T^u & \dots & & h_0^u \end{pmatrix}}_{\mathbf{H}_u} \underbrace{\begin{pmatrix} u_t \\ u_{t+1} \\ \vdots \\ u_{t+T} \end{pmatrix}}_{\mathbf{U}^f} + \underbrace{\begin{pmatrix} h_1^u & \dots & h_T^u & \\ h_2^u & \dots & h_T^u & 0 \\ \vdots & & \ddots & \\ h_T^u & \dots & & 0 \\ 0 & \dots & \dots & 0 \end{pmatrix}}_{\mathbf{G}_u} \underbrace{\begin{pmatrix} u_{t-1} \\ u_{t-2} \\ \vdots \\ u_{t-T} \end{pmatrix}}_{\mathbf{U}^p} \\ &+ \underbrace{\begin{pmatrix} h_0^s & \dots & h_T^s & \\ h_1^s & \dots & h_T^s & 0 \\ \vdots & & \ddots & \\ h_T^s & \dots & & 0 \end{pmatrix}}_{\mathbf{G}_s} \underbrace{\begin{pmatrix} s_t \\ s_{t-1} \\ \vdots \\ s_{t-T} \end{pmatrix}}_{\mathbf{S}^p}. \end{aligned} \quad (5.2)$$

To define the compensator, we minimize the predicted output norm $\|\mathbf{M}_T\|_2^2$. The solution then reads

$$\mathbf{U}^f = (-\mathbf{H}_u^+ \mathbf{G}_u) \mathbf{U}^p + (-\mathbf{H}_u^+ \mathbf{G}_s) \mathbf{S}^p, \quad (5.3a)$$

$$u(t) = [1 \ 0 \ \dots \ 0] \mathbf{U}^f, \quad (5.3b)$$

where \mathbf{H}_u^+ denotes the pseudo-inverse of \mathbf{H}_u (Penrose 1955). Equation (5.3) defines a linear dynamical system, whose inputs are the past measurements s and the past control inputs u , and whose output is $u(t)$. In practice, using a simple inverse would provide a system where the high frequencies are highly amplified, since $f_u \rightarrow 0$ at high frequencies. A pseudo-inverse is required with a non-zero tolerance level; it is based on the reciprocals of all singular values of \mathbf{H}_u that fall above a user-specified threshold. Setting this tolerance level is equivalent to applying a filter and enables an effective compensator design. Regardless of the tolerance level, the performance of the compensator increases with T . We set $T = 1000$, which corresponds to a non-dimensional time length of $t = 100$. For the tolerance level, best results were obtained for a value of 0.0218, where 48 singular values are retained.

5.1.2. Balanced truncation and characterization of the compensator

Once the compensator has been designed, it can be recast into a simpler state-space model through balanced truncation (the algorithm is described in Safonov & Chiang 1989). The transfer function of the compensator (5.3) can be described, without significant loss in accuracy, by a 14-modes state-space model that reads, in general

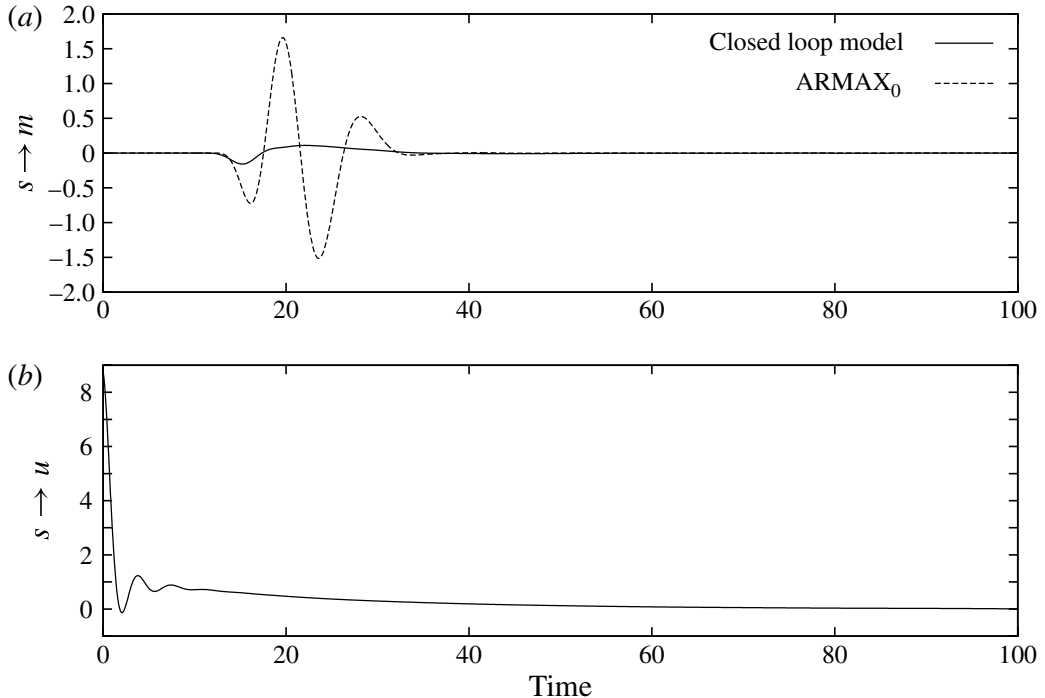


FIGURE 15. Impulse response of both the open-loop and closed-loop models. (a) Predicted measurements. The response of ARMAX₀ is the same as in figure 11. (b) Control law (corresponds to the impulse response of the compensator). Closing the loop efficiently reduces the effects of an impulse in s for the model.

form,

$$\mathbf{X}(t+1) = \mathbf{AX}(t) + \mathbf{Bs}(t), \quad (5.4a)$$

$$u(t) = \mathbf{Cx}(t) + \mathbf{ds}(t). \quad (5.4b)$$

Figure 15(a) shows a comparison between the impulse response of the open-loop model (no control) and impulse response of the closed-loop model (where the compensator is used to provide the control law). As expected, it shows a very effective reduction of the predicted output. The associated control law is shown in figure 15(b).

5.2. Control results

5.2.1. Using perfect sensors

So far, the effectiveness of the compensator has been tested on the identified model ARMAX₀ itself. In this section, we present results from DNS as the control. The compensator is driven by measurements from the DNS; the DNS, in turn, uses the control law that the compensator provides. The time step for the compensator has been changed from dt_m to dt_{dns} in order to compute a control law at each time step of the DNS while keeping the same transfer function. Such a transformation is straightforward and described in Antoulas (2005).

Figures 16 and 17 show the control performance using a compensator that consists of a state-space system of 14 modes. As anticipated, the compensator not only reduces the fluctuations of m (the r.m.s. value of the output fluctuations is reduced by 93 % in figure 16) but also accomplishes a reduction of 99 % of the perturbation energy in the entire computational domain (figure 17).

Figure 18 depicts the average turbulent kinetic energy of both the uncontrolled and the controlled simulations. The maximum peak of turbulent energy is located at

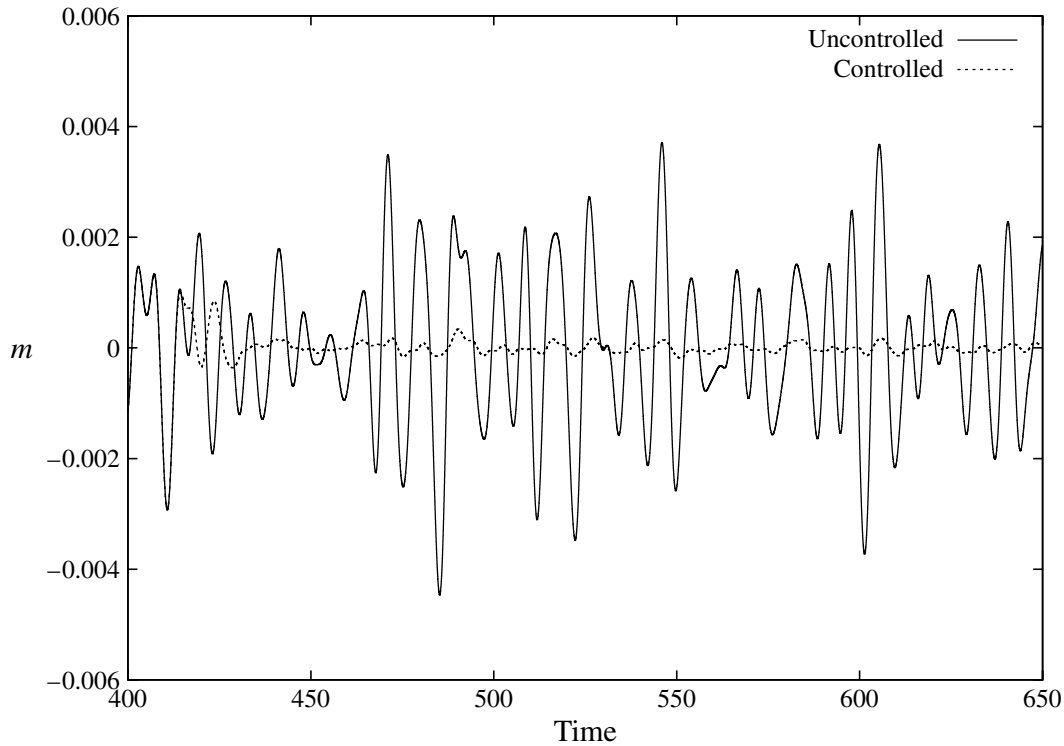


FIGURE 16. Output measurement m extracted from the DNS as a function of time. Both the controlled and the uncontrolled simulations (using the same exact source of random noise) are compared. The compensator is based on 14 modes, and the sensors are taken as noise-free.

$x \approx 25$ in both cases, with the output sensor placed near the reattachment point of the separation bubble (at $x = 10.5$). The maximum peak of turbulent energy coincides with the location where the convective instability ends, which is in agreement with linear theory. The choice of the downstream skin-friction measurement m as an appropriate objective for the control design is validated, since the reduction of its fluctuations led to a substantial reduction of the turbulent energy in the entire computational domain. The turbulent kinetic energy is reduced by 96 % at $x \approx 25$, the same location as where the uncontrolled turbulent kinetic energy is maximal.

5.2.2. Using noisy sensors

Noisy sensors are modelled by adding white Gaussian noise to all measured signals. Noise on m only affects the design process, whereas a noisy measurement s affects both the design process and the compensated simulation (the compensator is driven with a noise-contaminated measurement).

Figures 19 and 20 display the difference between the exact and corrupted signals, both for m and s , for different standard deviations of the noise. The noise root-mean-square (r.m.s.) value is expressed as a percentage of the r.m.s.-value of the exact signal. The same learning dataset has been used and corrupted with different levels of measurement noise. All models are generated using the same coefficients n_a , n_{bu} , n_{bs} , n_{du} , n_{ds} , n_c and the same tolerance for the pseudo-inverse.

Figure 21 illustrates the effect of the measurement noise on the control performance. The energy of the fluctuations is plotted versus time for the various simulations, and the standard deviation of the noise measurements is expressed as a percentage of the r.m.s. value of the noise-free signal. The compensator appears to be quite robust to measurement noise and remains effective even with the two measurements $[s, m]$

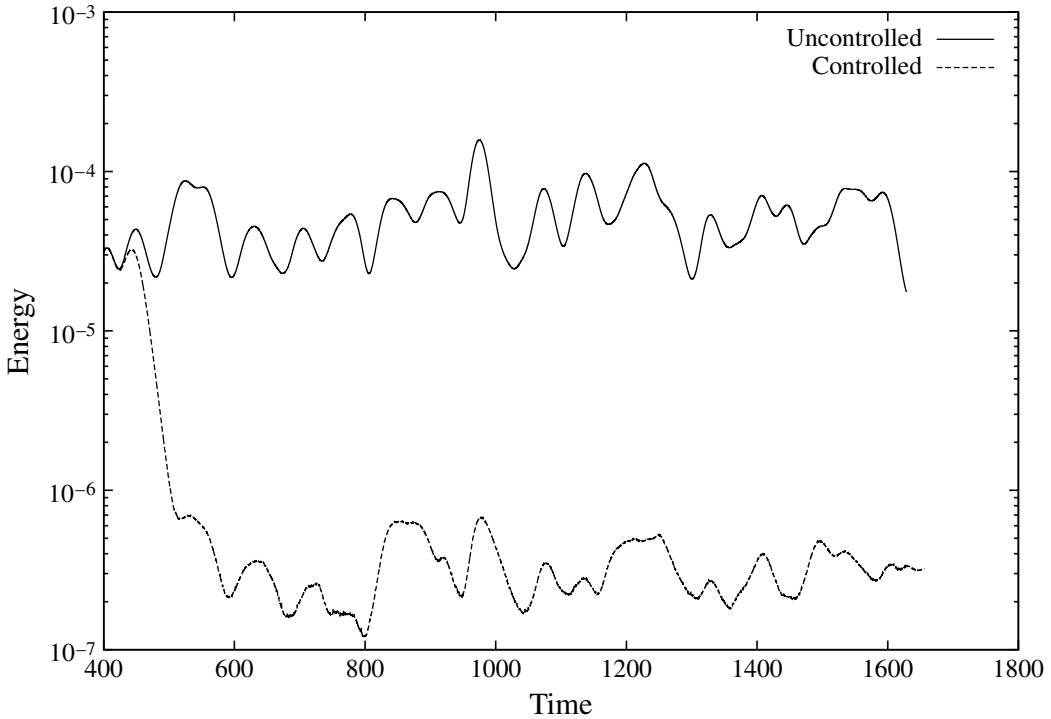


FIGURE 17. Perturbation energy from the DNS as a function of time. Both the controlled and the uncontrolled simulations (using the same exact source of random noise) are compared. The compensator is based on 14 modes, and the sensors are taken as noise-free.

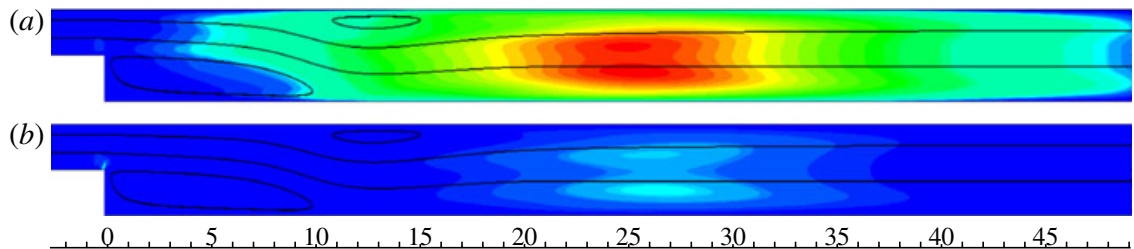


FIGURE 18. Contours of the mean turbulent kinetic energy from the numerical simulation (the vertical coordinate is stretched for more clarity). (a) Uncontrolled simulation. (b) Controlled simulation. Streamlines of the base flow are also shown. The control action is barely visible at the top corner of the step in the controlled simulation. The maximum peak of turbulent kinetic energy is reduced by 96 %.

corrupted by 100 % of their respective signal-r.m.s. As expected, noise-corrupted measurements, in general, lead to a reduced control performance. More specifically, a contamination of the signal s shows more effect on the performance than an equal contamination of the signal m . This should not come as a surprise since the measurement noise g_m is eliminated during the ARMAX regression and thus never appears again. A corruption of the measurement s , on the contrary, will affect both the ARMAX regression and the input signal of the compensator.

5.2.3. Using stronger perturbations

As the noise levels are raised, nonlinear effects start to come into play during the numerical simulations. To facilitate a comparison, the same random source sequence is used but is simply multiplied by a different amplitude σ_w (see table 5). The

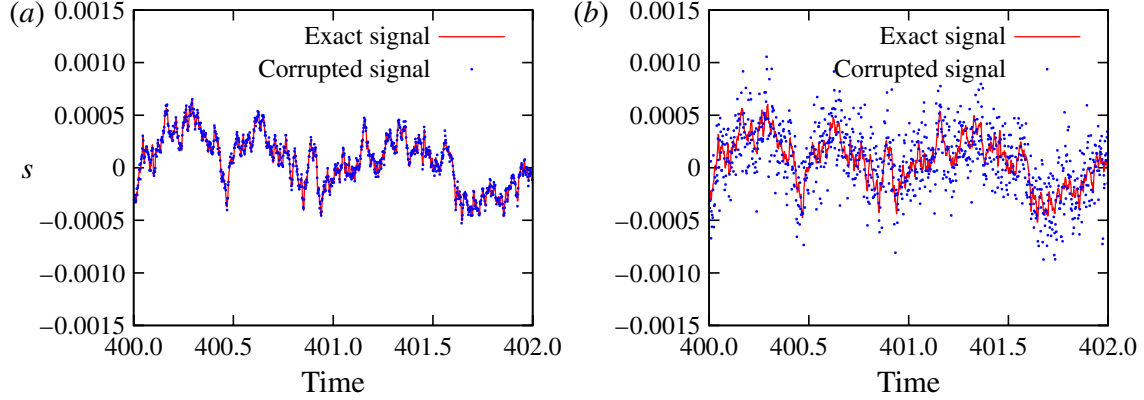


FIGURE 19. Short sequence of the noisy signal s , corrupted by 10 % of the r.m.s. of s (a) and by 100 % of the r.m.s. of s (b). The exact signal is extracted from the controlled numerical simulation whose energy is shown in figure 17.

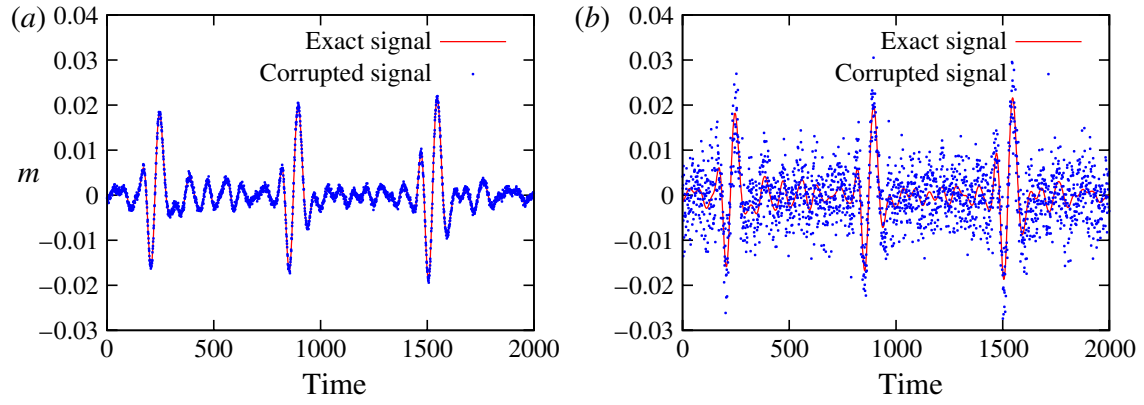


FIGURE 20. Comparison between the noise-free and noisy signal m from the learning dataset: (a) corrupted by 10 % of the r.m.s. of m , (b) corrupted by 100 % of the r.m.s. of m .

	n_1	n_2	n_3	n_4	n_5	n_6	nl_1	nl_2	nl_3
m_{rms} reduction (in %)									
Achieved	93	75	66	42	22	15	93	80	23
Expected	93	75	69	37	22	18	—	—	—
Energy reduction (in %)									
Achieved	99	95	85	76	55	43	98	87	49
Standard deviation of the noise σ_w	0.01	0.01	0.01	0.01	0.01	0.01	1	$\sqrt{10}$	10

TABLE 5. Summary of achieved and expected controller performances, as well as model-expected performances. n_i refers to the simulations from § 5.2.2 probing the influence of measurement noise; nl_i refers to the simulations from § 5.2.3 assessing the effects of nonlinearities. The relative standard deviation of the noise in the DNS computation is given by σ_w .

same controller based on ARMAX₀ (which has been computed with $\mathbf{G}_s = \mathbf{G}_m = 0$ and $\underline{\sigma}_w = 0.01$) is used for each simulation. To quantify the amount of nonlinear

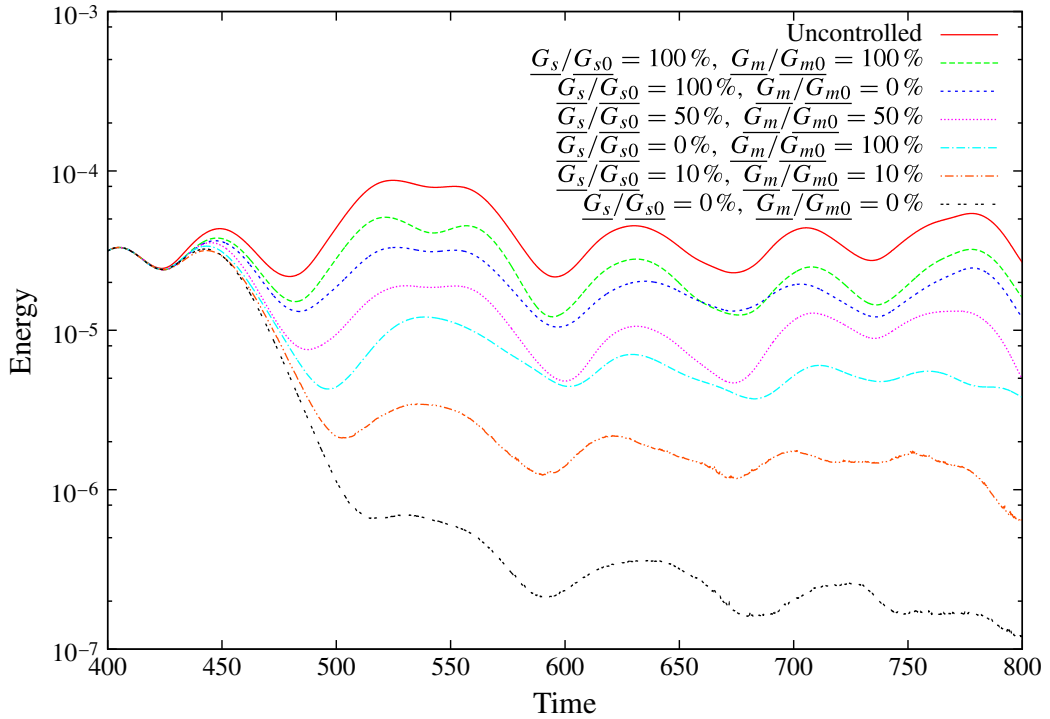


FIGURE 21. Effect of noisy sensors on the overall controller performance, measured by the kinetic energy (in semilog scale) versus time. Noise levels are expressed in percentage of the r.m.s. of the exact signals.

effects, a linearized simulation based on the same random source sequence has been computed. Figure 22 shows the resulting energy plots where three levels of noise are presented. Each level is displayed in a different colour; the dashed lines show the energy of the uncontrolled simulation, while the solid lines correspond to the controlled simulations. Symbols correspond to the extrapolated linear uncontrolled simulation, so that the difference between symbols and dashed lines shows the effects of nonlinearities. In each case, the controller starts at $t = 100$. For each simulation, the controller accomplishes a reduction of the perturbation energy. However, the *relative* energy reduction diminishes as the noise amplitudes (and thus the nonlinear effects) increase.

Figure 23 shows the average turbulent kinetic energy of the uncontrolled and controlled simulations for the case with strongest noise levels (the pink lines in figure 22). Compared to the linear case, the maximum peak of the turbulent energy has shifted to $x \approx 8$, a manifestation of the linear theory no longer holding. Nevertheless, the controller has been able to reduce the maximum peak of turbulent kinetic energy by an impressive 88 % (the maximum energy peak values for uncontrolled/controlled simulations are taken at $x \approx 8$ and $x \approx 15$, respectively) whereas the global reduction is 49 % (see nl_3 in table 5).

5.2.4. A final comparison

Table 5 summarizes the results of different controlled simulations. The abbreviations n_1, \dots, n_6 correspond to the six simulations performed in § 5.2.2 (see figure 21), arranged in descending order of energy reduction. The abbreviations nl_1, \dots, nl_3 correspond to the simulations that have been shown in § 5.2.3, figure 22, sorted in the same way. The expected reduction in the r.m.s.-values of m originates from the

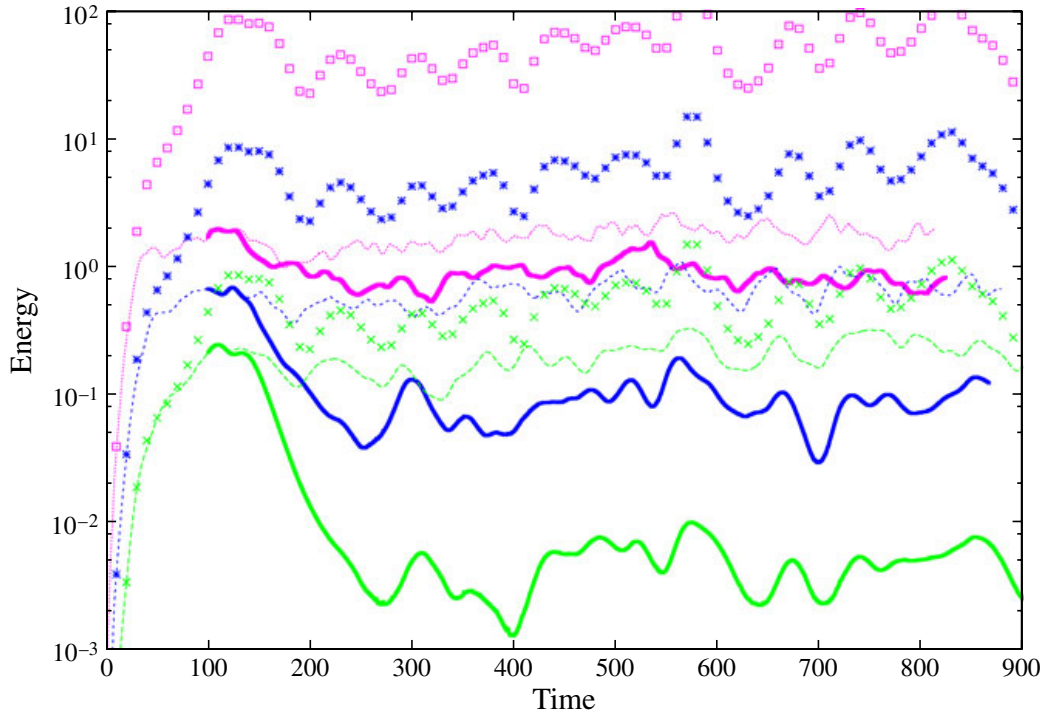


FIGURE 22. Control of nonlinear flows, displayed by perturbation energy as a function of time. Dashed lines: uncontrolled nonlinear simulations; solid lines: controlled nonlinear simulations. Symbols: extrapolated linear simulation. Curves of the same colour correspond to same level of noise excitation in the uncontrolled DNS. The controller starts after an initial transient period at $t = 100$.

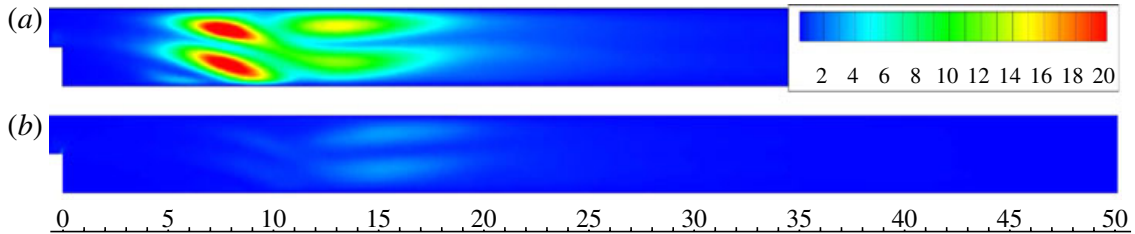


FIGURE 23. Contours of the average turbulent kinetic energy ($v_x^2 + v_y^2$) from the nonlinear numerical simulations (the vertical scale is stretched for more clarity). (a) The uncontrolled simulation; (b) the controlled simulation. The maximum peak of uncontrolled mean turbulent kinetic energy is located at $x \approx 8$ and is reduced through control efforts by 88 %.

control of the specific model that has been computed in § 4.2 by assuming noise-free sensors and low levels of environmental noise.

6. Conclusions

The flow over a backward-facing step has been considered as a typical amplifier flow where the influence of noise sources and model uncertainty plays a dominant role in the design of accurate low-order models and effective controllers. This type of flow is often encountered in industrial settings and research experiments; model-based control strategies, however, have shown only limited success when applied to amplifier flows under realistic disturbance environments. Rather than enforcing a particular

(idealized) flow model *a priori*, a model is extracted directly from time sequences of observable data. During the design process, special care has to be taken that only data which are readily available, e.g. in an experiment (generally contaminated by noise), enter the system-identification procedure.

In our case, a model has been designed based on an ARMAX-equation which consists of an auto-regressive (AR) component for the measurements, a moving-average (MA) component for the collective noise sources, and exogenous (X) terms for the input variables. The latter input variables are composed of the control input as well as an upstream sensor signal which acts as a proxy variable for the unknown upstream noise. The coefficients of this regression model are chosen on physical grounds by considering the general convective behaviour of the flow for the delay terms and by analysing the mutual influence (or lack thereof) of actuators and sensors. In a second step, the model forms the base of a feed-forward controller. Applying this combined system-identification/control-design approach to our flow over a backward-facing step yielded remarkable results. A reduction of more than 90 % of the measurement energy and total energy could be observed. Increasing the noise levels to high values did not compromise the stability of the compensator, even though its effectiveness diminished accordingly. An application of the linearly designed compensator to a nonlinear numerical simulation showed encouraging results. The *total* turbulent kinetic energy could still be reduced by nearly 50 % and the *maximal* turbulent kinetic energy by 88 %, even though the compensator operated far off its design point.

In summary, a robust and compelling flow control procedure has been introduced that is data-based in the model design and follows classical methods for model-reduction and control layout. This technique is particularly attractive for amplifier flows, where the accurate modelling of noise sources and their influence on system dynamics and sensor output is imperative for a successful compensator performance. It should also appeal to experimental efforts and practical applications of closed-loop flow control.

REFERENCES

- AKERS, J. C. & BERNSTEIN, D. S. 1997 ARMARKOV least-squares identification. *Proc. Am. Contr. Conf.* 186–190.
- AKERVIK, E., HOEPFFNER, J., EHRENSTEIN, U. & HENNINGSON, D. S. 2007 Optimal growth, model reduction and control in a separated boundary-layer flow using global eigenmodes. *J. Fluid Mech.* **579**, 305–314.
- ANTOULAS, A. C. 2005 *Approximation of Large-Scale Dynamical Systems. Advances in Design and Control*. Society for Industrial and Applied Mathematics.
- BAGHERI, S., BRANDT, L. & HENNINGSON, D. S. 2009 Input/output analysis, model reduction and control of the flat-plate boundary layer. *J. Fluid Mech.* **620**, 263–298.
- BARBAGALLO, A., SIPP, D. & SCHMID, P. J. 2009 Closed-loop control of an open cavity flow using reduced-order models. *J. Fluid Mech.* **641**, 1–50.
- BARKLEY, D., GOMES, M. G. M. & HENDERSON, R. D. 2002 Three-dimensional instability in flow over a backward-facing step. *J. Fluid Mech.* **473**, 167–190.
- BLACKBURN, H. M., BARKLEY, D. & SHERWIN, S. J. 2008 Convective instability and transient growth in flow over a backward-facing step. *J. Fluid Mech.* **603**, 271–304.
- CATTAFESTA, L., WILLIAMS, D. R., ROWLEY, C. W. & ALVI, F. 2003 Review of active control of flow-induced cavity resonance. *AIAA Paper* 2003-3567.
- DERGHAM, G., SIPP, D. & ROBINET, J.-C. 2011 Accurate low dimensional models for deterministic fluid systems driven by uncertain forcing. *Phys. Fluids* **23** (9), 094101.
- EFE, M. O. & OZBAY, H. 2003 Proper orthogonal decomposition for reduced order modelling: 2D heat flow. *IEEE Conf. Contr. Appl.* **2**, 1273–1277.

- GIBSON, J. S., LEE, G. H. & WU, C. F. 2000 Least-squares estimation of input/output models for distributed linear systems in the presence of noise. *Automatica* **36** (10), 1427–1442.
- GLOWINSKI, R. 2003 Finite element methods for incompressible viscous flow. In *Handbook of Numerical Analysis* (ed. P. G. Ciarlet & J. L. Lions). *Numerical Methods for Fluids (Part 3)*, vol. 9, pp. 3–1176. Elsevier.
- HUANG, S.-C. & KIM, J. 2008 Control and system identification of a separated flow. *Phys. Fluids* **20** (10), 101509.
- JUANG, J. N. & PAPPA, R. S. 1985 An eigensystem realization algorithm for modal parameter identification and model reduction (control systems design for large space structures). *J. Guid. Control Dyn.* **8**, 620–627.
- KIM, J. & BEWLEY, T. R. 2007 A linear systems approach to flow control. *Annu. Rev. Fluid Mech.* **39**, 383–417.
- LJUNG, L. 1999 *System Identification: Theory for the User*, 2nd edn. Prentice Hall.
- MA, Z., AHUJA, S. & ROWLEY, C. W. 2010 Reduced-order models for control of fluids using the eigensystem realization algorithm. *Theor. Comput. Fluid Dyn.* **25**, 1–15.
- MARQUET, O., SIPP, D., CHOMAZ, J.-M. & JACQUIN, L. 2008 Amplifier and resonator dynamics of a low-Reynolds-number recirculation bubble in a global framework. *J. Fluid Mech.* **605**, 429–443.
- MOORE, B. 1981 Principal component analysis in linear systems: Controllability, observability, and model reduction. *IEEE Trans. Autom. Control* **26** (1), 17–32.
- PENROSE, R. 1955 A generalized inverse for matrices. *Proc. Camb. Phil. Soc.* **51**, 406–413.
- ROWLEY, C. W. 2005 Model reduction for fluids, using balanced proper orthogonal decomposition. *Intl J. Bifurcation Chaos* **15** (5), 255–289.
- ROWLEY, C. W., COLONIUS, T. & MURRAY, R. M. 2004 Model reduction for compressible flows using POD and Galerkin projection. *Physica D* **189**, 115–129.
- SAFONOV, M. G. & CHIANG, R. Y. 1989 A Schur method for balanced-truncation model reduction. *IEEE Trans. Autom. Control* **34** (7), 729–733.
- SAMIMY, M., DEBIASI, M., CARABALLO, E., OZBAY, H., EFE, M. O., YUAN, X., DEBONIS, J. & MYATT, J. H. 2003 Development of closed-loop control for cavity flows. *AIAA Paper* 2003-4258.
- SAMIMY, M., DEBIASI, M., CARABALLO, E., SERRANI, A., YUAN, X., LITTLE, J. & MYATT, J. H. 2007 Feedback control of subsonic cavity flows using reduced-order models. *J. Fluid Mech.* **579**, 315–346.
- SIPP, D., MARQUET, O., MELIGA, P. & BARBAGALLO, A. 2010 Dynamics and control of global instabilities in open flows: a linearized approach. *Appl. Mech. Rev.* **63** (3), 030801.

Non linear control of vortex shedding phenomenon using low order model identification

3.1 Résumé de l'article

3.1.1 Configuration

Le sujet de cet article porte sur la modélisation et le contrôle d'un écoulement de lâcher tourbillonnaire derrière un profil NACA012, qui constitue un exemple typique d'écoulement oscillant, tels que décrits en §1. Le profil est soumis à une incidence de 30° , et l'écoulement devient instable au-delà d'un Reynolds critique $Re_c = 96$. Comme on l'a introduit en §1 (voir figure 1.8 page 12), la dynamique linéarisée s'éloigne progressivement de la dynamique observée au fur et à mesure que le nombre de Reynolds augmente. Ici, on cherche à explorer des méthodes de réduction de modèle adaptée à un cas éloigné du seuil de criticité. Le nombre de Reynolds pour le contrôle sera donc fixé à $Re = 200$, soit environ $2Re_c$.

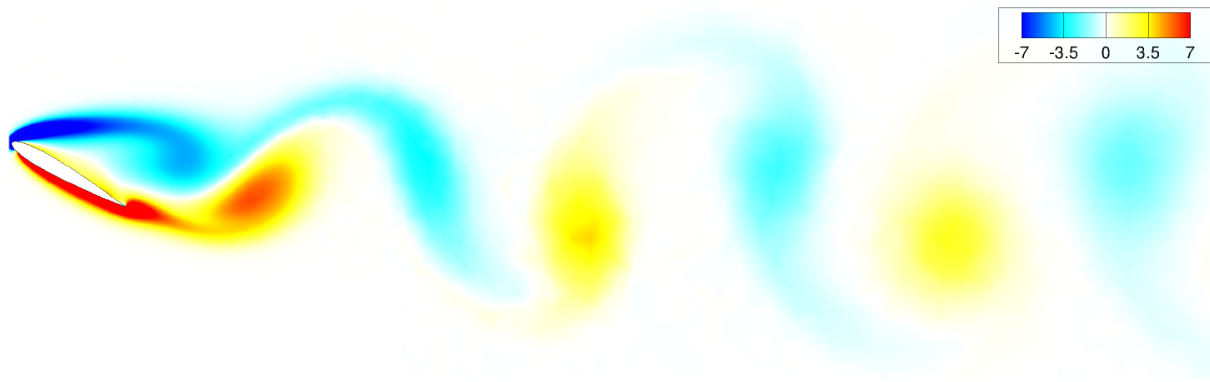


Figure 3.1 – Cliché simulé d'écoulement derrière un profil NACA012 à 30° d'incidence (contours de vorticité).

La figure 3.1 montre un cliché de simulation typique, obtenu à $Re = 200$. On y voit un lâcher tourbillonnaire, similaire à ce que l'on peut observer derrière un cylindre ([Galletti et al., 2004](#); [Bergmann et al., 2009](#)).

Pour établir un contrôle en boucle fermée on utilise un actuateur et un capteur, comme montré figure 3.2. L'actuateur est situé en amont du bord de fuite. Il est une fois de plus constitué d'un forage volumique situé proche de la paroi, et “souffle” avec un angle de 30° par rapport à la normale de la corde, dans le sens de l'écoulement. De façon similaire à

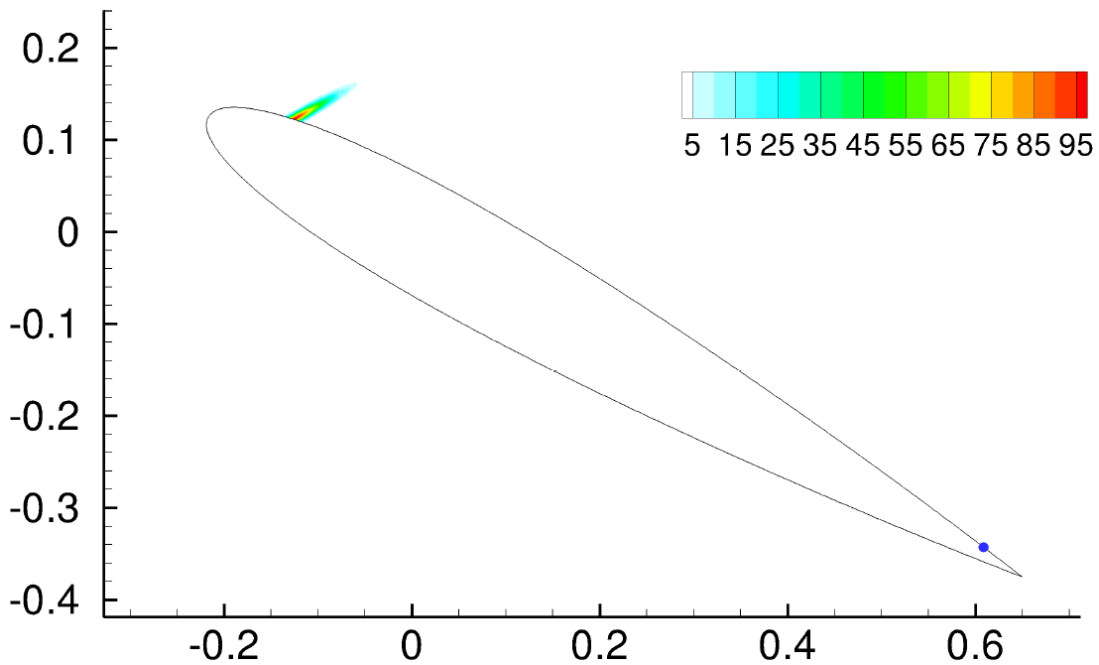


Figure 3.2 – Placement de l’actuateur et du capteur de frottements pariétaux pour le contrôle en boucle fermée.

l’approche utilisée en §2, on place un capteur de frottement pariétal en aval de l’aile, dont la réduction des fluctuations définit un objectif de contrôle. Le placement de ce capteur assure une bonne sensibilité aux structures tourbillonnaires aval.

3.1.2 Modélisation

La modélisation de cet écoulement par identification se déroule ici en deux étapes distinctes. Dans un premier temps, la dynamique dite *libre* de l’écoulement est identifiée. Elle correspond aux oscillations de l’écoulement, sans influence du forçage. La deuxième partie sera dédiée à la prise en compte des effets du contrôle dans l’écoulement.

Dynamique libre De par la nature des structures spatiales cohérentes qui constituent l’instabilité, une approche spatiale POD est choisie pour modéliser l’écoulement (voir discussion en §1.3 sur les différentes approches de réduction). L’algorithme choisi n’est toutefois pas classique. On montre en effet qu’un calcul POD basé sur l’énergie cinétique de l’écoulement (voir équation (1.4), page 6) produit une base dont les variations des modes ne sont pas visibles au moyen du capteur aval utilisé comme objectif. Afin d’augmenter l’observabilité de la base, un produit scalaire différent est introduit dans l’algorithme POD, qui aura pour effet de produire une base pouvant à la fois prédire la mesure aval m avec précision, en même temps qu’elle décrit la structure du lâcher tourbillonnaire que l’on cherche à contrôler.

Une fois la base POD déterminée, on dérive une structure de modèle compatible avec les équations de Navier-Stokes. L'approche théorique de la projection de Galerkin fournit pour cela une structure de modèle que l'on garde, en considérant toutefois les coefficients qui la constituent comme des régresseurs dont les valeurs seront identifiées par la suite. De plus, la dépendance en Reynolds est conservée à travers une variable $\varepsilon = \frac{1}{50} - \frac{1}{Re}$. En effet, l'étude des équations projetées de Navier-Stokes montre qu'un lien existe entre la dynamique à bas Reynolds et la dynamique à plus haut Reynolds. Ainsi, en observant le comportement de l'écoulement sur différents régimes, on améliore la qualité du modèle obtenu à $Re = 200$.

Le modèle choisi se lit donc

$$x_i^{t+1} - x_i^t = \varepsilon^t A_i + \underbrace{\sum_j (B_{ij} + \varepsilon^t \beta_{ij}) x_j^t + \sum_{j,k} C_{ijk} x_j^t x_k^t}_{\Phi_i(X^t, \varepsilon^t)}, \quad (3.1)$$

où A, B, β, C sont les régresseurs, dont les valeurs seront identifiées.

L'identification du modèle est détaillée dans l'article, et donne d'excellents résultats pour prévoir à la fois l'évolution temporelle des coefficients POD, mais aussi de la mesure aval m .

Enfin, la recherche d'un point fixe de l'équation (3.1) permet de définir un champ POD qui servira d'objectif de contrôle. On pourra alors vérifier la correspondance entre cet état stationnaire identifié et la projection du champ de base exact sur la base POD réduite considérée. Ce test permet d'évaluer si la physique de l'écoulement a bien été capturée par le modèle. En effet, l'étude physique de l'écoulement montre l'existence d'un unique point fixe qu'est le champ de base. On peut donc s'attendre à ce qu'un modèle correctement identifié accepte également un point fixe correspondant à ce champ de base. De fait, les résultats montrent une remarquable correspondance entre les deux champs, comme montré figure 3.3

Dynamique forcée Une fois la dynamique libre et le champ de base identifiés, il reste à inclure l'influence du forçage dans le modèle. En accord avec l'argumentaire développé en 1.3, des résultats préliminaires montrent que l'influence instantanée d'une commande sur la base POD est presque négligeable. En effet, le contrôle est vu comme un détail spatial, et n'est de ce fait pas pris en compte par l'algorithme POD, dont la nature même est d'évacuer les structures spatiales de faible dimension. Si le contrôle a un effet visible sur la base, ce n'est qu'au bout d'un certain temps, qui correspond à la croissance spatiale des structures que l'actuateur introduit dans l'écoulement. Pour cette raison, on choisit d'inclure l'effet du contrôle dans le modèle par une réduction de type temporelle. Ainsi, plutôt que de prendre en compte un grand nombre de modes spatiaux représentant l'influence complète du contrôle, on préfère ne prendre en compte que son influence sur les 5 modes POD principaux, mais sur une fenêtre temporelle étendue.

Afin d'isoler les effets du forçage, on construit un ensemble de données noté Δ , correspondant à la différence entre la prédiction du modèle Φ (3.1) et l'état POD observé. Pour un modèle Φ suffisamment précis, on peut considérer que cette différence est due aux seuls effets du forçage. Le modèle le plus simple pour ce faire peut être défini par une régression

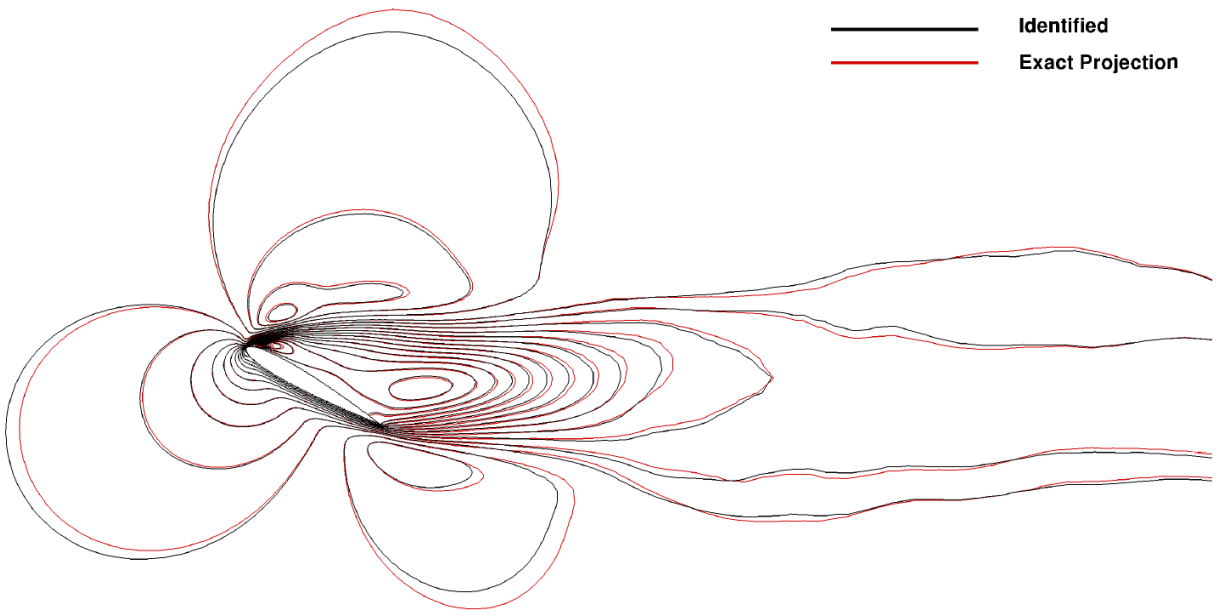


Figure 3.3 – Comparaison entre le champ de base évalué d’après l’identification de la dynamique saturée (noir), et la projection rigoureuse du champ de base sur la base POD choisie (rouge).

linéaire

$$\Delta^t = (X^{t+1} - X^t) - \Phi^t = \underbrace{\sum_{k=0}^{n_u} \alpha_k u^{t-k}}_{\Psi(u^t, \dots, u^{t-n_u})}, \quad (3.2)$$

et montre des résultats satisfaisants.

Modèle final Une fois les deux modèles Φ et Ψ identifiés, on forme un modèle final capable de prédire l’évolution de l’écoulement dans un cas forcé. La figure 3.4 montre un exemple où le modèle prédit l’évolution de la mesure pendant une simulation forcée aléatoirement.

3.1.3 Contrôle

Contrairement à l’article présenté en §2, on réalise ici un contrôle purement non-linéaire. Pour des raisons de praticité, le modèle est exprimé sous la forme

$$X^{t+1} = f(X^t) + Bu^t \quad (3.3a)$$

$$m^t = CX^t, \quad (3.3b)$$

où l’état X est redéfini de manière à inclure les deux modèles $\Phi + \Psi$.

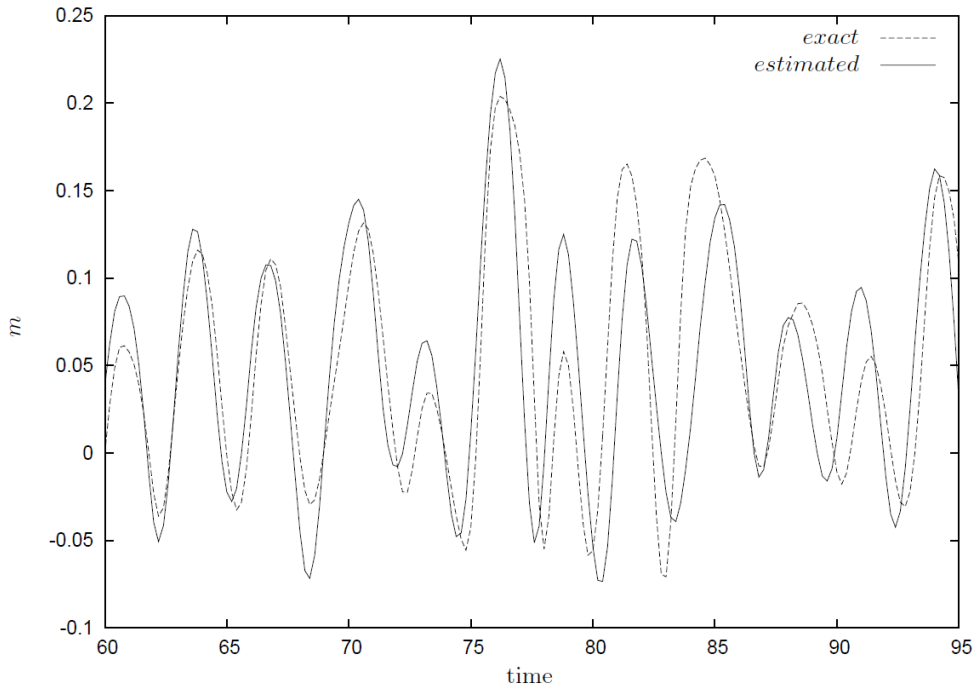


Figure 3.4 – Prédiction de la mesure par le modèle réduit. Les résultats sont comparés à ceux obtenus par une simulation CFD. Ici, le champ est excité au moyen d'une loi de forçage aléatoire de forte amplitude. Le modèle réduit prédit avec une précision satisfaisante l'évolution de la mesure.

L'optimisation de la loi de contrôle passe alors par une formulation Lagrangienne, avec une fonctionnelle définie par

$$J^t = \frac{1}{2} \sum_{i=t}^{t+100} [(CX^i - CX_{200}^i)^2 + l^2(u^i)^2], \quad (3.4)$$

et dont le but est de réduire les fluctuations de m autour de la valeur du champ de base (identifié) m_{200} , tout en introduisant un coût de contrôle via la variable l .

Les résultats sont finalement présentés, et montrent une réduction importante des oscillations de la mesure m . La figure 3.5 montre la réduction obtenue sur l'énergie moyenne des perturbations. De façon similaire aux résultats présentés en §2, on observe que la résolution d'une fonctionnelle basée sur une mesure de frottement pariétal permet de réduire l'énergie turbulente des fluctuations en champ libre de manière importante.

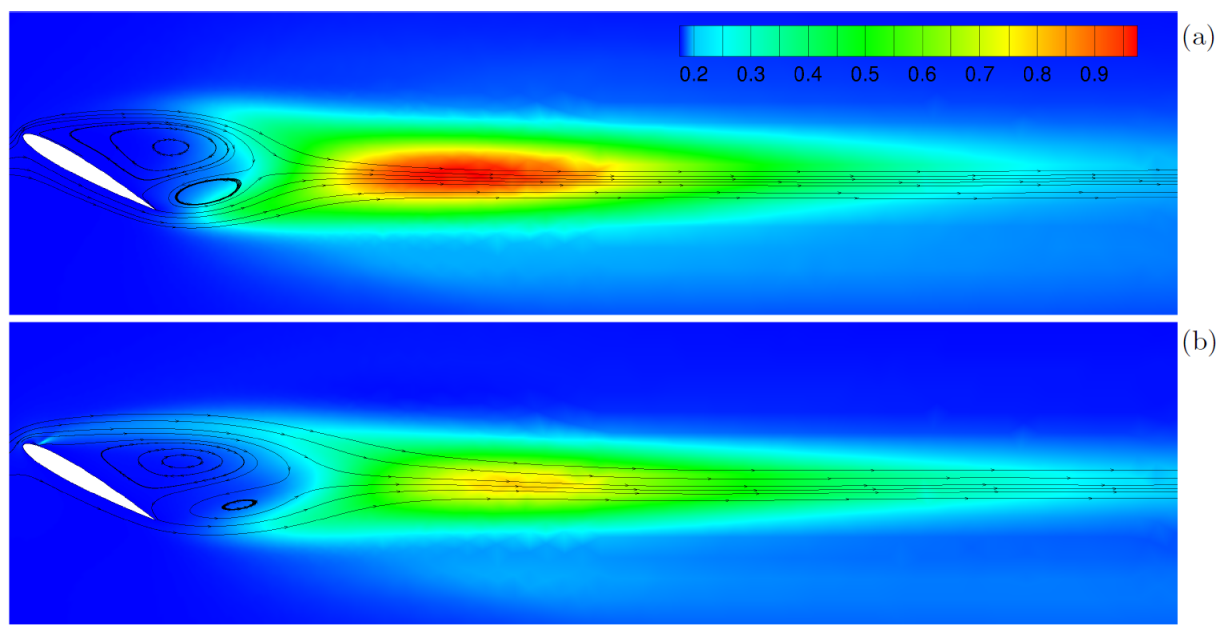


Figure 3.5 – Résultat de contrôle : visualisation de l'énergie turbulente des perturbations autour du champ de base. En haut : simulation non contrôlée. En bas : simulation contrôlée.

Non linear control of vortex shedding phenomenon using low order model identification

AURELIEN HERVÉ¹, DENIS SIPP¹,
PETER J. SCHMID²

¹ONERA, 8 rue des Vertugardins, 92190 Meudon, France

²Laboratoire d'Hydrodynamique (LadHyX), CNRS-Ecole Polytechnique, 91128 Palaiseau, France

³ONERA-DTIM, 2 av. Edouard Belin, 31055 Toulouse, France

(Received 24 October 2012)

Supercritical vortex shedding behind an airfoil at a large angle of attack is controlled using system identification of a nonlinear reduced-order model. A modified POD technique is used that produces an observable POD basis which in turn produced a model of the unforced flow dynamics by nonlinear system identification. The effects of the control input are taken into account using a simple linear model. Based on these models, a nonlinear model-predictive control (MPC) technique is then applied which significantly reduces the unsteadiness of the flow.

1. Introduction

Flow control is a discipline of fluid mechanics that has received a great deal of interest over the past years. With a great many applications that could conceivably benefit from an altered flow behavior to increase efficiency, suppress instabilities or reduce sensitivities, flow control will continue to play an important role in the design and improvement of fluid devices.

The majority of flow control studies have applied linear control techniques to a flow linearized about an equilibrium point, commonly the base flow. This approach has resulted in successful designs for globally stable flows that amplify environmental noise or for globally unstable flows that have to remain sufficiently close to the equilibrium point (see, e.g. Ahuja & Rowley 2010). Once a globally unstable flow deviates too far from the equilibrium point and settles into a limit-cycle behavior, linear flow control quickly becomes ineffective since the saturated flow dynamics can no longer be represented by the linearized model. Configurations such as, e.g., flow over an open cavity (Akervik *et al.* 2007; Cattafesta *et al.* 2008; Barbagallo *et al.* 2009) or vortex shedding behind a bluff body (He *et al.* 2000; Bergmann & Cordier 2008; Ahuja & Rowley 2010) are characterized by strongly nonlinear dynamics associated with a few unstable global modes. The ensuing oscillatory flow behavior is a common target of flow control. Even though open-loop control can be employed to suppress the flow unsteadiness in some cases (Tokumaru & Dimotakis 1991; He *et al.* 2000; Protas & Wesfreid 2002), closed-loop control represents a far more promising approach: an efficient control strategy designed within a closed-loop framework can drastically reduce the cost of control and, at the same time, increase robustness (Cattafesta *et al.* 2003). The difficulty of controlling this type of flow mainly arises from the strong nonlinearities that become even more pronounced as the Reynolds number increases. In addition, even though a steady state of the Navier-Stokes equations

(i.e., a base flow) still exists at higher Reynolds numbers, this base flow becomes more elusive as it is unobservable without efficient control, and also quite different from the mean flow. Nonetheless, the base flow needs to be determined such that an acceptable control objective can be specified.

The present work aims at applying model-predictive control (MPC) to vortex shedding in a strongly saturated state. Various nonlinear approaches using POD-Galerkin projection techniques have been proposed in the literature (Bergmann *et al.* 2005). For such models, calibration techniques (Sirisup & Karniadakis 2004; Cordier *et al.* 2010) are mandatory but can be difficult to implement in an experiment. Instead of using a model-based approach, this study follows up on Hervé *et al.* (2012) and proposes a framework for model reduction solely based on data that are readily available in an experiment. Identification techniques are quite suited for this purpose, allowing the extraction of reduced-order models from observed temporal input and output sequences. These techniques are well known in the system theory and automatic control communities (Ljung 1999), but also seem to provide a promising framework for model reduction in flow control (Morgans & Dowling 2007; Huang & Kim 2008; Hervé *et al.* 2012) owing to their robustness and general applicability. The framework proposed herein will only use velocity fields (available, e.g., from TR-PIV measurements) and shear-stress signals and will rely on physical insight to build a reduced-order model of the flow dynamics. In the course of the model identification, we will also recover base flow properties from the observation of the unsteady system dynamics. Using both a low-order model of the dynamics and the identified base flow, a nonlinear controller can then be designed.

In §2, the flow configuration as well as the control objective is introduced and the input forcing and ouput measurements are defined. The process of model reduction is covered in detail in §3. It consists of two distinct steps. First, a nonlinear model that describes the unforced dynamics of the flow is derived in §3.1. It uses a POD basis determined by a modified algorithm that improves the observability of the modes by the given sensor. In a second step, the effects of the control input (forcing) are accounted for via a linear model that explicitly describes the transfer function between the input signal and the retained POD modes (§3.2). A controller is then designed using classical optimization techniques in §4 and its performance on the full numerical simulations is assessed.

2. Flow configuration and control objective

We consider the two-dimensional flow around a NACA 0012 airfoil inclined at an angle of attack (AoA) of 30° which is governed by the nonlinear, incompressible Navier-Stokes equations

$$\partial_t \mathbf{v} + \mathbf{v} \cdot \nabla \mathbf{v} = -\nabla p + \nu \Delta \mathbf{v}, \quad (2.1a)$$

$$\nabla \cdot \mathbf{v} = 0. \quad (2.1b)$$

We use direct numerical simulations to explore flow features at various Reynolds numbers (based on the airfoil chord, denoted by c , and the free-stream velocity) ranging from 50 to 200. A finite-element spatial discretization is employed, where the velocity fields are projected onto six-node triangular elements with quadratic interpolation (P2-elements), while the pressure field is discretized using three-node triangular elements with linear interpolation (P1-elements). A typical mesh of about 60,000 triangles is sufficient to resolve all relevant scales over the above range of Reynolds numbers. The computational domain stretches from $x = -4$ to $x = 10$; the upper and lower boundaries are located at $y = \pm 3$. Inflow conditions ($v_x = U_\infty, v_y = 0$) are used at the inlet, symmetry conditions ($\partial_y v_x = 0, v_y = 0$) are applied at the upper and lower boundaries,

no-slip conditions ($v_x = 0, v_y = 0$) are employed on the airfoil surface, and standard outflow conditions ($p - \nu \partial_x v_x = 0, \partial_x v_y = 0$) are imposed at the outlet. The pressure field is obtained using the Uzawa algorithm, preconditioned by the Cahouet-Chabart method (Glowinski 2003). The temporal discretization is semi-implicit and based on a second-order backward-differentiation (BD2) scheme; a characteristics-based Galerkin method is used for the convective terms of the governing equations. The time-step in all reported simulations is equal to $\Delta t = 0.01$, and temporal and spatial refinement studies have been conducted to ensure converged results.

Similar to flow around a cylinder (see, e.g., Sipp & Lebedev 2007), the flow around an airfoil undergoes a super-critical Hopf bifurcation. The critical Reynolds number is found to be equal to $Re_c = 96$. For Reynolds numbers lower than this critical value, the flow converges towards a steady state, an equilibrium point of the Navier-Stokes equations referred to as a base flow. These base-flow solutions can be traced beyond the critical Reynolds number Re_c (e.g. using Newton's method), even though they can no longer be observed in direct numerical simulations or experiments. At supercritical Reynolds numbers, the base flow becomes linearly unstable and the flow converges towards a limit cycle. All flow variables then display periodic oscillations whose amplitudes increase with Reynolds number. For supercritical Reynolds numbers, the mean flow which is obtained by time-averaging over the limit cycle, is considerably different from the base flow. In particular, the region of separated flow is substantially smaller for the mean flow than for the corresponding base flow. This feature is illustrated in figure 1 for a supercritical Reynolds number of $Re = 200$, where the base flow (a), mean flow (b) and a representative snapshot on the limit cycle (c) is shown, visualized by vorticity.

Note that a Reynolds number of $Re = 200$ is significantly higher than the critical Reynolds number $Re_c = 96$, which ensures the presence of strong nonlinearities in the flow dynamics. The nonlinear character of the flow at a supercritical Reynolds number of $Re = 200$ is also reflected in a comparison of the Strouhal number of the flow (obtained from the numerical simulations) and the non-dimensionalized frequency of the unstable global mode (obtained from a stability analysis of the base flow, see Barkley (2006)). Figure 2 shows the Strouhal numbers $St = f_c \sin(\alpha)/U_\infty$ (with α as the angle of attack) for these two cases as a function of the Reynolds number for $Re > Re_c$. Coinciding at the critical Reynolds number $Re_c = 96$, the two curves quickly diverge as the Reynolds number increases. This behavior can be attributed to nonlinear interactions, in particular to the mean-flow harmonic generated by the unstable global mode (see Sipp *et al.* 2010). It is worth noting that the described dynamics is reminiscent of the cylinder wake at supercritical Reynolds numbers (see Barkley 2006; Sipp & Lebedev 2007, for a comparison). The control effort proposed in this article aims at suppressing the shedding of vortices into the wake. To this end, we use an actuator whose input signal will be denoted by $u(t)$. The actuator is located near the leading edge on the suction side of the airfoil (see figure 3) and consists of an elliptical, 60°-rotated volume force of Gaussian shape modeled by the expression

$$\mathbf{f} = \begin{bmatrix} \sin(\theta) \\ \cos(\theta) \end{bmatrix} A \exp \left(-a(x - x_0)^2 + 2b(x - x_0)(y - y_0) + c(y - y_0)^2 \right) \quad (2.2)$$

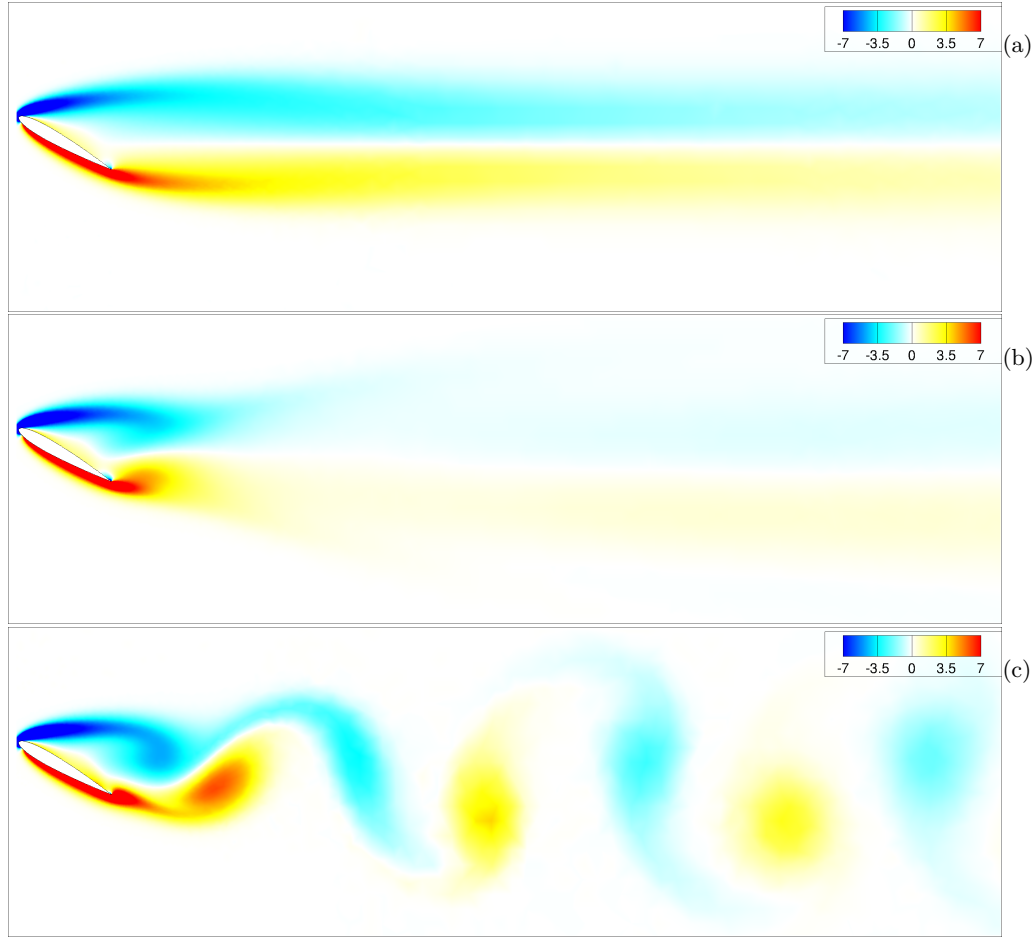


FIGURE 1. Flow around a NACA 0012 airfoil at a 30° angle of attack and a chord Reynolds number of $Re = 200$, visualized by contours of vorticity: (a) base flow, (b) mean flow, and (c) selected snapshot from the limit cycle.

with

$$a = \frac{\cos^2 \theta}{2\sigma_x^2} + \frac{\sin^2 \theta}{2\sigma_y^2}, \quad (2.3a)$$

$$b = -\frac{\sin 2\theta}{4\sigma_x^2} + \frac{\sin 2\theta}{4\sigma_y^2}, \quad (2.3b)$$

$$c = -\frac{\sin^2 \theta}{2\sigma_x^2} + \frac{\cos 2\theta}{2\sigma_y^2}. \quad (2.3c)$$

The numerical values for the parameters $\theta, A, x_0, y_0, \sigma_x, \sigma_y$ are given in table 1. The choice of actuator location was driven by practical considerations; more effective, but far less feasible locations in the far-field have been studied in, e.g., Ahuja & Rowley (2010). Nonetheless, our actuator has a discernible influence on the flow in the wake of the airfoil.

This article proposes a model-identification framework for the recovery of the flow dynamics from data that could readily be provided within an experimental setting. For this reason, we assume to have access to flow snapshots (such as the one shown in Figure

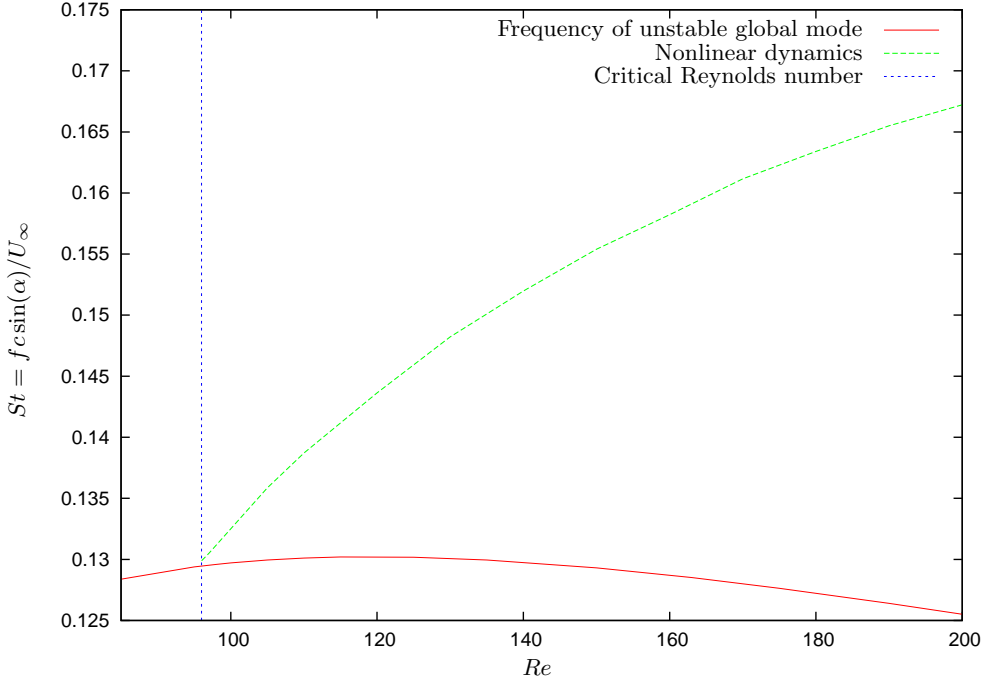


FIGURE 2. Strouhal number as a function of Reynolds number. Blue: critical Reynolds number ($Re = 96$). Green: observed nonlinear, unsteady dynamics of the flow. Red: frequency of the unstable global mode associated with the linearized dynamics about the base flow.

θ	A	x_0	y_0	σ_x	σ_y
60°	10	-0.13	0.12	$5 \cdot 10^{-3}$	$5 \cdot 10^{-2}$

TABLE 1. Parameter values for the Gaussian-shaped volume forcing (see equ. (2.2) and (2.3)).

1(c)) and to shear-stress measurements m near the trailing edge (see Figure 3). This type of data could be obtained from time-resolved PIV measurements and a shear-stress sensor, respectively. Figure 4(a) presents a sample of the shear-stress signal for flow on the limit cycle at Reynolds $Re = 200$. For comparison, the values of the base flow and mean flow (obtained by averaging) have been indicated as well. An oscillatory skin friction signal has been obtained as expected. It appears instructive to visualize the flow dynamics in form of a phase diagram representing, e.g., the measurement m versus its time-derivative \dot{m} . The limit cycle manifests itself as a closed curve, while both the base flow and the mean flow correspond to a single point in this phase portrait. The phase portrait corresponding to the above shear-stress signal is given in figure 4(b) for a Reynolds number of $Re = 200$; base flow and mean flow are indicated by colored symbols.

We will later apply model predictive control (MPC) which requires (i) an attainable objective and (ii) a reliable model. Based on the findings above, we will use the base flow as our control target, as it represents a steady-flow solution and thus minimizes vortex shedding. In terms of the phase portrait (see figure 4), we attempt to drive the system

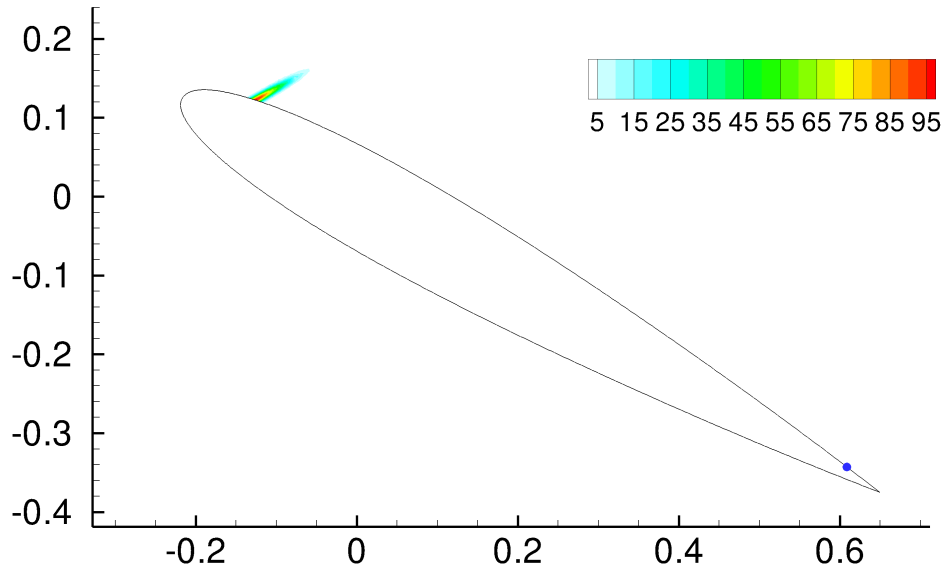


FIGURE 3. Actuator and sensor location on the airfoil. The actuator is modeled by volume forcing located near the leading edge (visualized by velocity contours); the sensor is located near the trailing edge (blue symbol) and records the skin friction.

from the limit-cycle curve towards the point referring to the base flow. At Reynolds numbers only slightly above Re_c , the difference between the base and mean flow is rather small and linearization about the base flow yields an effective control design (Ahuja & Rowley 2010). At strongly super-critical Reynolds numbers, however, linear models fail, making nonlinear models imperative. Recalling figure 2, the frequency of the unstable global mode is nearly 30% lower than the limit-cycle frequency; consequently, the dynamics linearized about the base flow no longer furnishes a valid model of the flow behavior on and near the limit cycle. This latter observation poses a serious challenge for system identification. Since the objective can no longer be observed directly (neither by numerical simulation nor by experiment) due to an unstable base flow, special care has to be exercised when formulating the model to be identified. Moreover, the low-order, identified model must be able to provide accurate representations over a range of dynamic behavior — from the saturated unsteady dynamics (the uncontrolled state) to the dynamics in the vicinity of the base flow (our control objective). The latter base-flow state may not be observable without efficient control, which adds further difficulties and demands on the chosen identification strategy.

3. Reduced-order modeling

The unsteady fluid process we seek to control consists of the periodic shedding of large-scale structures into the wake of the airfoil, and it seems reasonable to assume that this type of motion could be captured by a low-order model based on proper orthogonal decomposition (POD) modes where only the most energetic modes are taken into account. An efficient control input, in contrast, should consist of rather small energy which nevertheless ultimately impacts the large-scale flow dynamics via a reverse energy cascade, such as, e.g., a flow instability. A POD description of the controlled flow would thus eliminate the control input as an energetically insignificant detail, unless an unreasonably

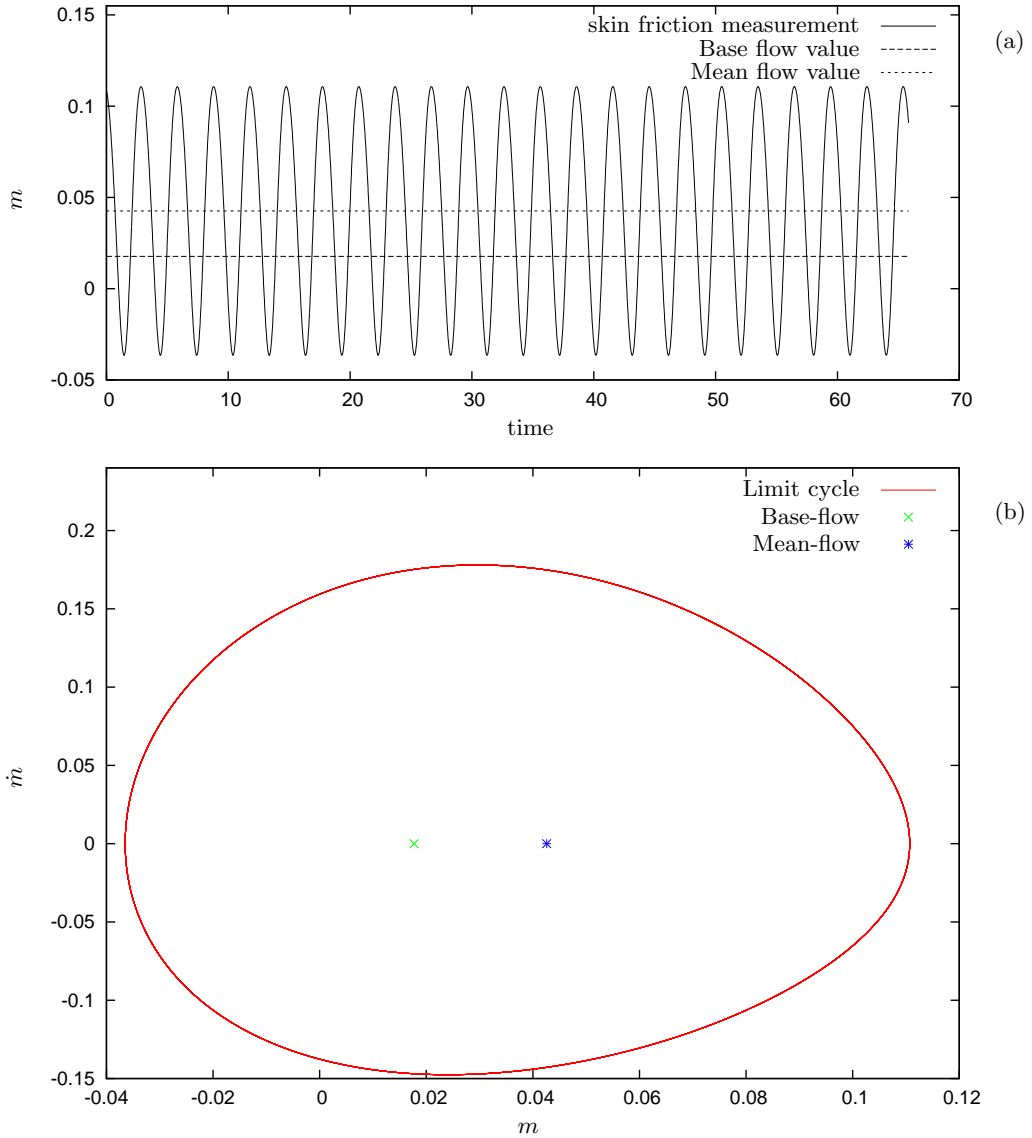


FIGURE 4. (a) Sample of the skin-friction signal m for a Reynolds number of $Re = 200$. The two horizontal lines refer to the mean-flow and base-flow values. (b) Corresponding phase diagram showing limit-cycle behavior (phase trajectory in red); the base-flow value is represented by the green symbol, the mean-flow value by the blue symbol.

large number of POD modes is considered. To resolve this issue, we propose a procedure consisting of two distinct steps. First, a model that solely captures the uncontrolled dynamics of the flow over a range of Reynolds numbers is identified (§3.1). At this point, no control input is taken into account, and the model can be based on the large-scale features (observed in figure 1) to produce a representation of the flow dynamics with only a small number of POD modes. In a second step, extra terms are added to the previous model to account for the effects of actuation (§3.2). The design of these terms relies on a

temporal, rather than a spatial, model reduction: the additional terms directly describe how the control input affects the previously defined spatial structures over a specified time interval.

3.1. Modeling the unforced dynamics

We commence by modeling the unforced dynamics of the flow. A customized POD algorithm is first introduced (§3.1.1), that ensures observability of the obtained basis by the shear-stress sensor downstream. In §3.1.2, a physics-based model structure is then proposed, whose coefficients need to be identified. Several data-sets are defined in §3.1.3, which span the range of the particular flow dynamics to be modeled. Finally, the model coefficients are identified from these data-sets, and validation tests are performed in §3.1.4.

3.1.1. Definition of an observable POD basis

Proper Orthogonal Decomposition (POD) aims at extracting a set of spatial structures $\{\phi_k\}$ from a series of snapshots \mathbf{v}_i . The basis formed by these structures is then optimal in representing the dynamics given by the snapshot sequence, where optimality is related to a chosen scalar product $\langle \cdot, \cdot \rangle$. In addition, the basis $\{\phi_k\}$ is orthonormal, satisfying $\langle \varphi_{k_1}, \varphi_{k_2} \rangle = \delta_{k_1 k_2}$. A given snapshot \mathbf{v} can thus be approximated by

$$\mathbf{v} \approx \mathbf{v}_R + \sum_k x_k \varphi_k, \quad x_k = \langle \varphi_k, \mathbf{v} - \mathbf{v}_R \rangle \quad (3.1)$$

where \mathbf{v}_R is a selected reference flow. We denote by $X = [x_1, x_2 \dots]^T$ the reduced-order state; the POD technique then guarantees that the POD modes φ_k minimize the error $\sum_i \|\mathbf{v}_i - (\mathbf{v}_R + \sum_k x_{ki} \varphi_k)\|^2$ over all possible orthonormal bases. The norm $\|\cdot\|$ is induced by the scalar product $\langle \cdot, \cdot \rangle$. As a reference solution \mathbf{v}_R we take the base flow at $Re = 50$.

For incompressible homogeneous flow, it is common practice to use the inner product based on the kinetic energy, in our case,

$$\langle \mathbf{u}, \mathbf{v} \rangle = \iint (u_x \cdot v_x + u_y \cdot v_y) \, dx dy. \quad (3.2)$$

The resulting reduced-order model is particularly efficient in capturing the most energetic structures of the flow — the ones that ultimately have to be controlled. Yet this choice does not ensure that the shear-stress sensor m (used in estimating the flow state) will be able to detect these structures. For this reason, it is important to verify that the true measurement of a flow field \mathbf{v} is reproduced by our low-dimensional POD model. In mathematical terms,

$$m(\mathbf{v}) \approx m(\mathbf{v}_R) + \sum_k x_k m(\phi_k) \quad (3.3)$$

on relevant phase-space trajectories. The coefficients $m(\phi_k)$ represent the measurement associated with the POD modes ϕ_k . The above relation may be deduced from expansion (3.1) and from the fact that the shear-stress measurement is linearly related to the flow-field. Property (3.3) is important since the signal m will be part of the control strategy; for example, the objective functional used in the control design could be based on the reduction of the variance of m . Additionally, the use of a dynamic observer to reconstruct the reduced state requires a comparison between the true measurement m of the flow-field and the current measurement m from the observer. If a given state does not yield an accurate sensor signal, it is rather unlikely that the sensor signal will result in an accurate estimation of the state. In short, we need to design a reduced-order model that represents both the energetic structures of the flow (which have to be controlled)

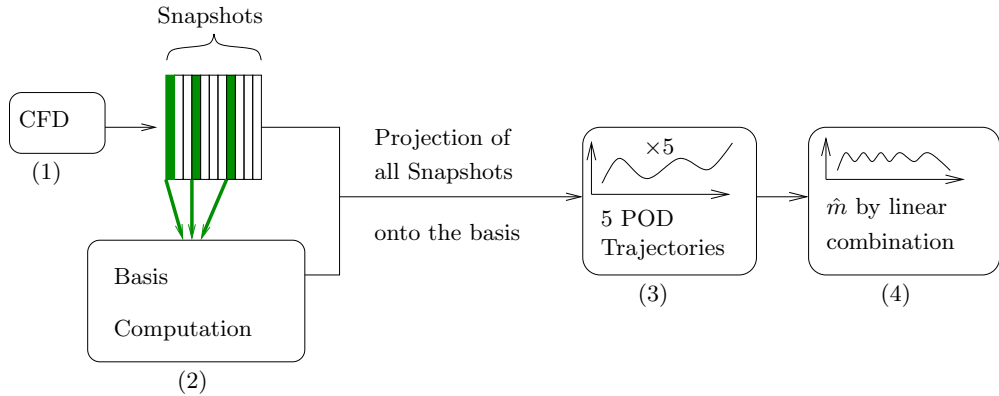


FIGURE 5. Estimation of the measurement signal for a given low-dimensional basis. (1) A numerical simulation is first performed which provides a set of snapshots. (2) Some of these snapshots are then used to compute a basis. (3) Once the basis is defined, all simulated snapshots can be projected onto the basis to form a POD phase-space trajectory. (4) The estimated measurement m is then obtained via a linear combination of the POD trajectories.

and the skin friction measurement m . For this reason, we define the customized scalar product

$$\langle \mathbf{u}, \mathbf{v} \rangle = K \cdot (1 - \alpha) [m(\mathbf{u}) \cdot m(\mathbf{v})] + \alpha \iint (u_x \cdot v_x + u_y \cdot v_y) \, dx dy \quad (3.4)$$

that incorporates the measured values $m(\mathbf{u}), m(\mathbf{v})$ of the flow variables (\mathbf{u}, \mathbf{v}) , in addition to the standard kinetic energy term. The multiplicative constant K scales the measurement term so that it has approximately the same order of magnitude as the kinetic-energy term. The parameter α can then be chosen within the interval $[0, 1]$ to balance the two components of the scalar product. Using (3.4), in place of the standard energy scalar product, will promote structures that have both a high energetic value and a strong signature in the measurement signal m , and will ultimately produce a basis that is observable by the sensor m .

To illustrate the effect of the customized scalar product, two different bases $(\mathcal{B}_1, \mathcal{B}_{1/2})$ have been computed, respectively with $\alpha = 1$ and $\alpha = 1/2$. More details on the snapshots used in the computations will be provided in §3.1.2. Following the sketch in figure 5, we can assess the capability of the two bases to reproduce the measurement m for a given flow field trajectory $\mathbf{v}(t)$. We compute the POD trajectories $x_k(t)$ for the first five POD modes ϕ_k with $k = 1, \dots, 5$ and the associated estimated measurements using the expression on the right-hand side of (3.3). In figure 6, we compare the estimated measurement signal to the true measurement $m(\mathbf{v})$ for the two bases. It clearly shows that only the basis with $\alpha = 1/2$ (with the measurement m included in the scalar product) is able to fully reproduce the true measurement m . In practice, the results are rather insensitive to changes in $\alpha \in (0, 1)$, so long as any measurement information is accounted for; the case $\alpha = 1$ (no measurement information) leads to a loss of observability. The precise choice of α with $0 < \alpha < 1$ in (3.4) is thus of secondary importance. We have verified that the results shown in figure 6 also hold for a larger set of basis modes (up to 20 POD modes); nevertheless, in what follows we choose five POD modes for our reduced-order model

3.1.2. Model structure

Identification of a model from observations requires the prior definition of a model structure that is able to characterize the system dynamics as accurately as possible.

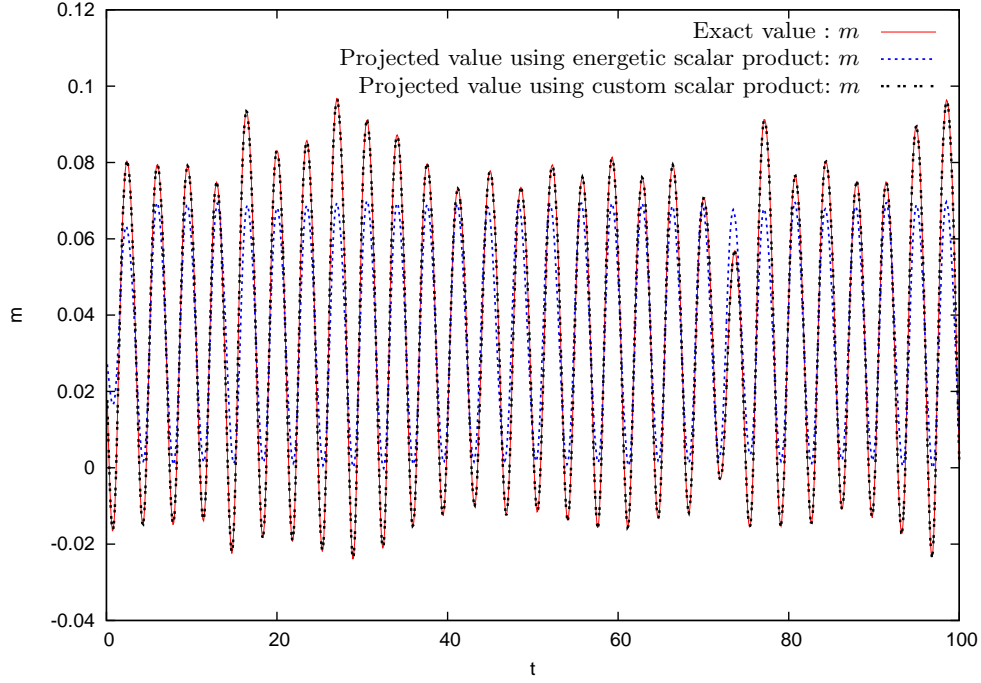


FIGURE 6. Comparison between the exact measurement $m = m(\mathbf{v})$ and the projected measurement $m = m(\mathbf{v}_R) + \sum_k x_k m(\phi_k)$ using different scalar products. Using a scalar product that only involves the kinetic energy, a basis with five modes does not reproduce the exact measurement values. In contrast, using the customized scalar product (3.4) for the design of the POD modes, the exact measurement signal can be recovered.

The model structure is obtained by considering the governing equations (2.1) and the expansion (3.1). In the governing equations, the Reynolds number Re will be replaced by the parameter ε defined as

$$\varepsilon = \frac{1}{Re_R} - \frac{1}{Re} \quad (3.5)$$

where $Re_R = 50$ is the Reynolds number associated with the base-flow \mathbf{v}_R . After substituting expansion (3.1) into equations (2.1), all terms involving only the reference base-flow cancel since \mathbf{v}_R is a steady solution of the Navier-Stokes equations at $Re = Re_R$. Projecting the resulting equation onto a given POD structure ϕ_i , using the orthogonality condition of the basis and integrating in time over a sampling time Δt yields

$$x_i^{t+1} - x_i^t = \varepsilon^t A_i + \underbrace{\sum_j (B_{ij} + \varepsilon^t \beta_{ij}) x_j^t + \sum_{j,k} C_{ijk} x_j^t x_k^t}_{\Phi_i(X^t, \varepsilon^t)} \quad (3.6)$$

where $A_i, B_{ij}, \beta_{ij}, C_{ijk}$ are constant coefficients. The time index is indicated in form of a superscript t or $t+1$. For $\varepsilon = 0$, (3.6) admits $X = \{x_i\} = 0$ as a steady solution, which stems from the definition of \mathbf{v}_R . Conforming to a traditional Galerkin projection technique (see Bergmann *et al.* 2005), the coefficients would be obtained by numerically evaluating inner products involving \mathbf{v}_R and the POD structures ϕ_k . Here, the model coefficients will not be determined by a Galerkin projection but rather identified using a training data-set. Galerkin projection simply ignores the influence of the neglected

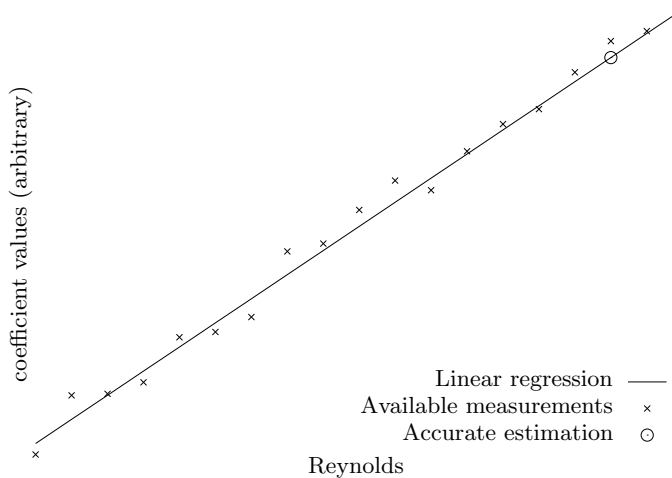


FIGURE 7. Illustration of linear regression (on random values) over a range of Reynolds numbers. The prediction of one single value (the circled symbol) is made more precise by using many measured points, rather than by taking a single measurement at the desired Reynolds number.

POD modes on the chosen POD basis and, consequently, has to be properly calibrated *a posteriori* to take into account these neglected modal effects (Galletti *et al.* 2004; Cordier *et al.* 2010). Ignoring these adjustments often leads to unstable reduced-order model, since the stabilizing effect of low-energy (neglected) POD modes on high-energy (included) modes is absent. Even though all model-reduction techniques introduce errors during the modeling procedure, identification commonly results in an effective model which captures an observed flow behavior. Our results will corroborate this point by demonstrating that the identification framework provides a remarkably stable and accurate model — a feature that is not easily obtained using a classical Galerkin projection technique.

Equation (3.6) shows that terms involving the coefficients B_{ij} and C_{ijk} are independent of the Reynolds number ϵ , whereas terms involving the coefficients A_i and β_{ij} are linearly dependent on ϵ . Even though the main goal of the present work is to obtain an accurate model of the dynamics at $Re = 200$, we will perform the identification of the coefficients with data-sets where the Reynolds number varies from $Re = Re_R$ to $Re = 200$. The rationale for this procedure is two-fold. First, scanning over a range of Reynolds numbers exposes the model to a richer dynamics which will ultimately yield an improved accuracy of the coefficients. This point is schematically illustrated in figure 7: precision at a given Reynolds number (circular symbol in figure 7) can be increased by providing more data points at lower Reynolds numbers (cross symbols) for the linear regression. Second, such a regression will indirectly parameterize the model by the Reynolds number. We thus expect the model to be effective over the same range of Reynolds numbers it has seen during the training/identification phase. This latter point will be illustrated in more detail in §3.1.4.

3.1.3. Learning and testing data-sets

The training data-set to determine the coefficients in (3.6) contains a sweep in the Reynolds number from $Re = 50$ to $Re = 200$; the protocol is shown in figure 9(a). In what follows, time t is non-dimensionalized by the airfoil chord and the free-stream velocity at Reynolds number $Re = 200$. Hence, the oscillation frequency drastically increases in the learning data-set as time evolves due to the increase of the free-stream velocity (see

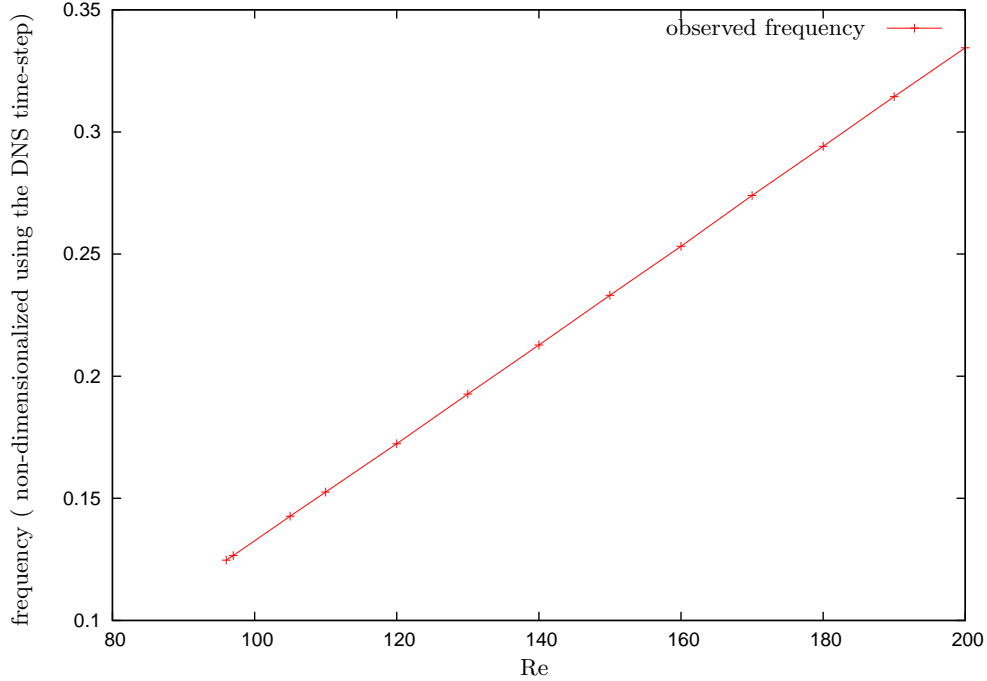


FIGURE 8. Frequencies variation for the training data-set. For Reynolds numbers below $Re_c = 96$, a peak to peak frequency is measured when possible. These values are identical to the ones used in figure 2 to plot the change in Strouhal number.

figure 8). In addition, a forcing signal $u(t)$ is imposed, which comprises localized peaks of random amplitude. This type of signal triggers transient responses of the flow which are of particular interest for the identification process as they allow the exploration of the system dynamics in the neighborhood of the limit cycles (see figure 9(b)). To be strict, one should remove from the training data-set those doublets (X^t, X^{t+1}) during which forcing has been applied, since no external driving term is included in our model. Doing so would only leave us with the transients that follow the forcing peaks. Yet, with the identification being a statistical process, our results showed that the forced snapshot-doublets occur sufficiently seldom to be influential; additionally, the regression algorithm acts as a filter that eliminates any ill effects. It is thus possible to consider the full training data-set. The flow trajectory in phase space is shown in figure 10 for a range of Reynolds numbers and forcing inputs.

The resulting trajectory shows a superposition of many limit cycles corresponding to different Reynolds numbers, each one perturbed by localized forcing peaks. This figure lends support to the discussion in §3.1.2 by showing that varying the Reynolds number and imposing randomly distributed localized forcings during the identification phase helps explore a far wider part of phase space than by simply focusing on the limit-cycle at $Re = 200$.

To compute the POD basis associated with the learning data-set, a correlation matrix is computed using 94 randomly chosen snapshots $\mathbf{v}_1 \cdots \mathbf{v}_{94}$, comprising both forced and unforced fields at Reynolds numbers ranging from $Re = 50$ to $Re = 200$. The correlation matrix R reads

$$R_{ij} = \langle \mathbf{v}_i, \mathbf{v}_j \rangle \quad (3.7)$$

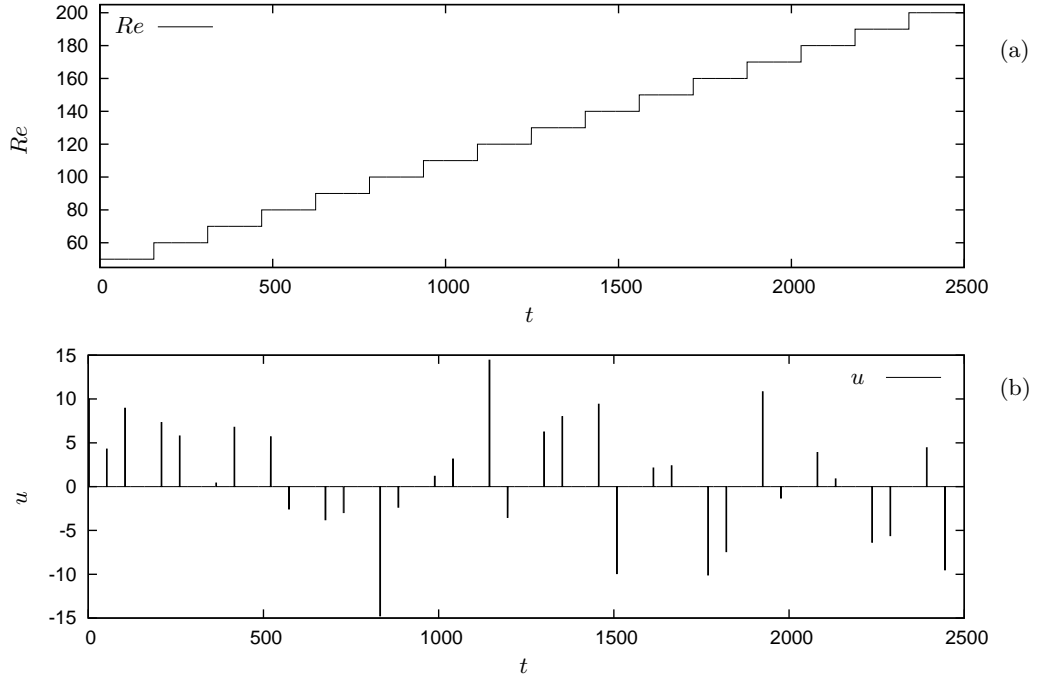


FIGURE 9. Training data-set: evolution of (a) the Reynolds number and (b) the forcing signal u as a function of time.

where the inner product $\langle \cdot, \cdot \rangle$ defined in (3.4) has been used. The POD modes ϕ_k are obtained from an eigendecomposition of the matrix R according to

$$R\phi_k = \lambda_k \phi_k, \quad \lambda_1 \geq \dots \geq \lambda_n \geq 0 \quad (3.8)$$

with n as the number of retained modes to form the POD-basis for our model; see Rowley (2005) for more details about the above algorithm. Once the POD basis is established, each snapshot in the training (and later testing) data-set can be projected onto this basis, so that training (and testing) POD phase-space trajectories can be defined. The number of modes in the POD basis has been varied from $n = 1$ to $n = 11$. Owing to the complexity of (3.6), the cost of identifying the model coefficients (3.6) quickly increases with the number of modes (the number of coefficients scales as n^3). We were able to verify that a model based on five POD modes yields most satisfactory results (see §3.1.4 for more details). Figure 11 shows the training POD trajectories for the first five POD modes. They are characterized by spikes stemming from the randomly distributed forcing peaks introduced in figure 9(b); the variation in the amplitude of mean value are due to changes in the Reynolds number according to the protocol shown in figure 9(a). We notice a general tendency of increasing amplitudes in time due to correspondingly larger limit-cycle amplitudes.

3.1.4. Model regression and validation

Once the training POD trajectories have been obtained, the unknown coefficients of the model (3.6) can be identified. The chosen structure fits a NLARX (NonLinear AutoRegressive eXogenous) model, and Matlab's `idnlarx` function from the System Identification Toolbox may be used to perform the regression. The choice of the basis dimension

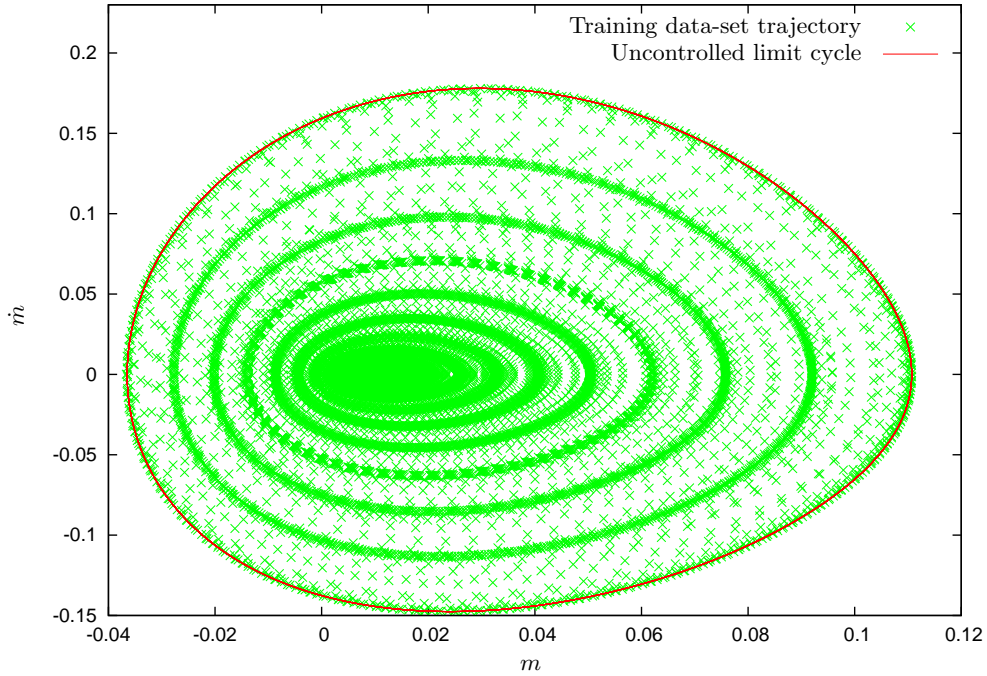


FIGURE 10. Trajectory of the training data-set, visualized in phase space (m, \dot{m}). Multiple limit cycles are visible, as well as transient trajectories that arise from both the forcing peaks and from the Reynolds number variations. A substantial part of the phase space (m, \dot{m}) is covered by such a simulation, in contrast to the phase-space trajectory of figure 4 where only one limit cycle is visible.

is not straightforward, and increasing the basis dimension from one to eleven showed that five modes provided the best results. This observation is also supported by the marked drop in the eigenvalues λ associated with (3.8) for $n > 5$ (see figure 17). The regression using `idnlarx` yielded the following loss function: $\det(E^T E) = 1.41 \cdot 10^{-20}$, where E stands for the residual error matrix. This low value confirms that the chosen model structure efficiently captures and represents the training dynamics.

In order to confirm that the thus identified model not only fits the training data-set (a situation commonly referred to as over-learning), a testing data-set has to be defined. Instead of increasing the Reynolds number, we chose to decrease it from $Re = 200$ to $Re = 140$, using smooth sigmoid transitions (see figure 12). No forcing is used in this simulation, since our current model is not yet capable of taking into account such forcings. As before, we choose to decrease the free-stream velocity to modify the Reynolds number, and time t is non-dimensionalized by the airfoil chord and the free-stream velocity at $Re = 200$ ($U_\infty = 1$ at $Re = 200$).

Figure 13 shows a comparison between the reduced-order measurement m obtained from (3.3) and the true measured value $m = m(\mathbf{v})$ from the DNS. A remarkable agreement is observed: as the Reynolds number progressively decreases, both the frequency and the amplitude shifts are accurately captured, and the model remains in phase with the exact trajectory over the entire simulation. Figure 14 displays results from the same simulation but represents the estimated and exact POD trajectories within the time interval $t = 40$ to $t = 190$. It shows that the model not only recovers the output mea-

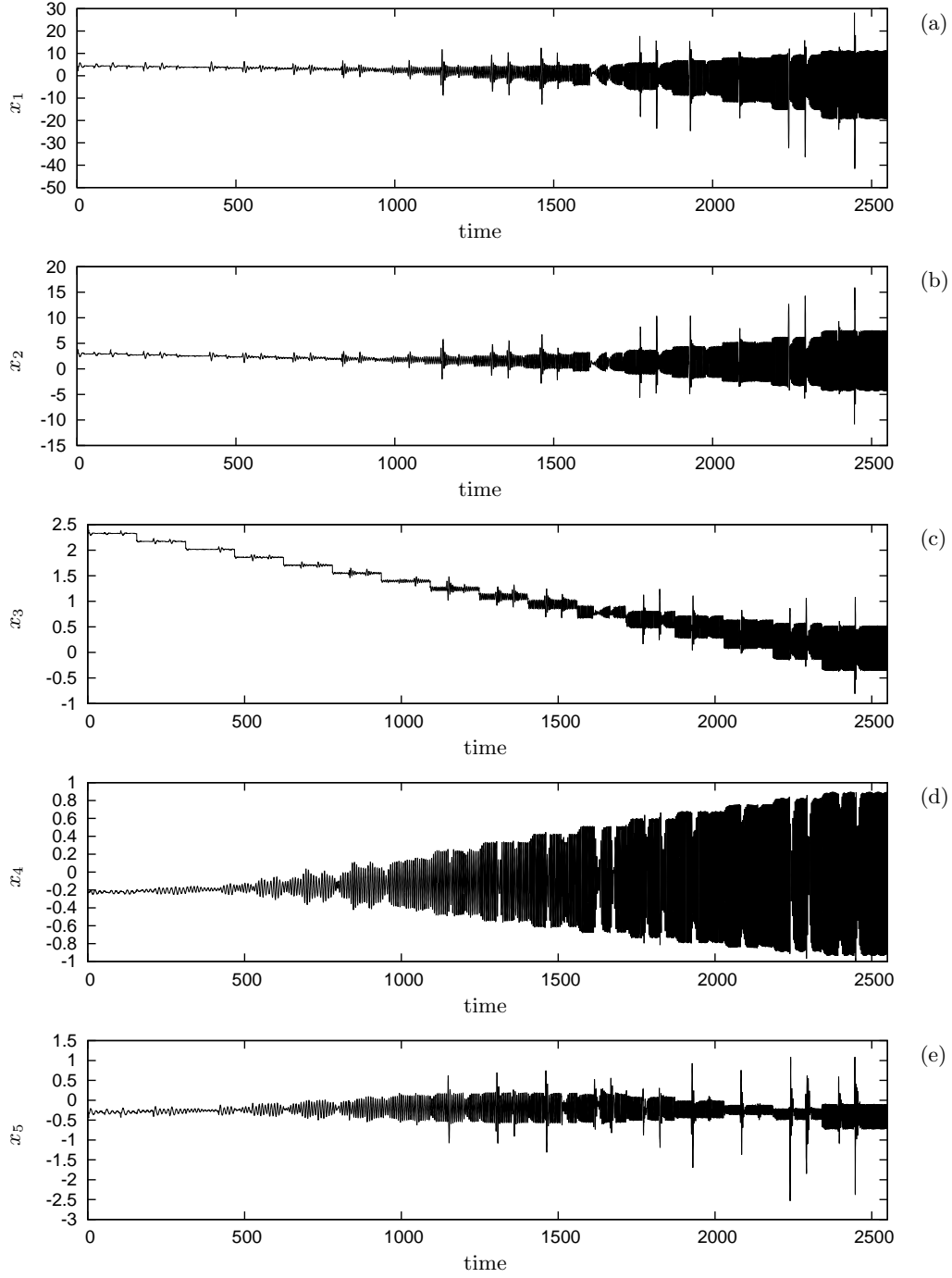


FIGURE 11. Training data-set POD trajectories. First five POD modes ((a) to (e)) are shown. Peaks are related to the forcing peaks introduced in figure 9(b), whereas the amplitude or mean value variations are linked to the Reynolds number variations shown in figure 9(a).

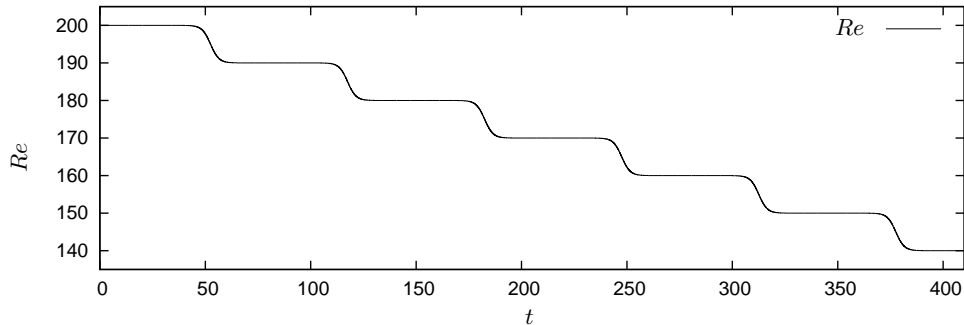


FIGURE 12. Reynolds number protocol versus time for the testing data-set; no external forcing is applied.

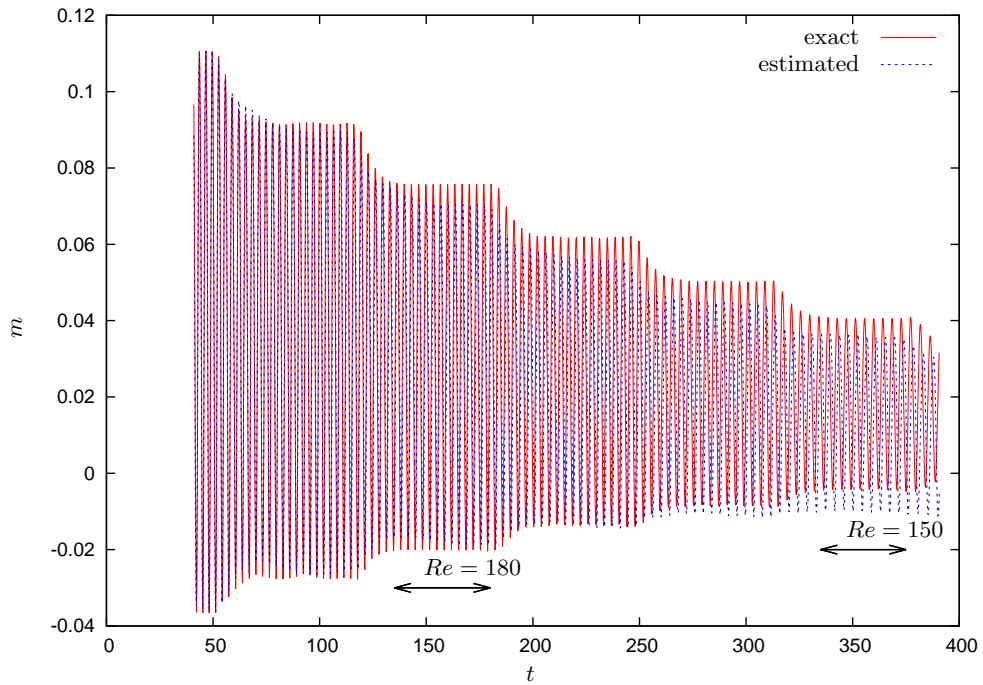


FIGURE 13. Shear-stress measurement m for testing data-set: estimated by the nonlinear model (blue dashed line) and measured exact values (red solid line).

surement, but also recovers all five POD trajectories. Finally, figure 15 confirms the ability of the low-order model to reproduce the different Strouhal numbers that are associated with different Reynolds numbers. It shows a remarkable correspondence between the observed and the identified dynamics. This observation verifies that accuracy of the low-order model is maintained over a wide range of Reynolds numbers.

3.1.5. Base-flow and linear dynamics

The equilibrium point of the Navier-Stokes equations (i.e., the base-flow) at $Re = 200$ may not be observed in the simulation, due to its linear instability. However, if the identified low-order model captures the observed flow dynamics, it is reasonable to expect

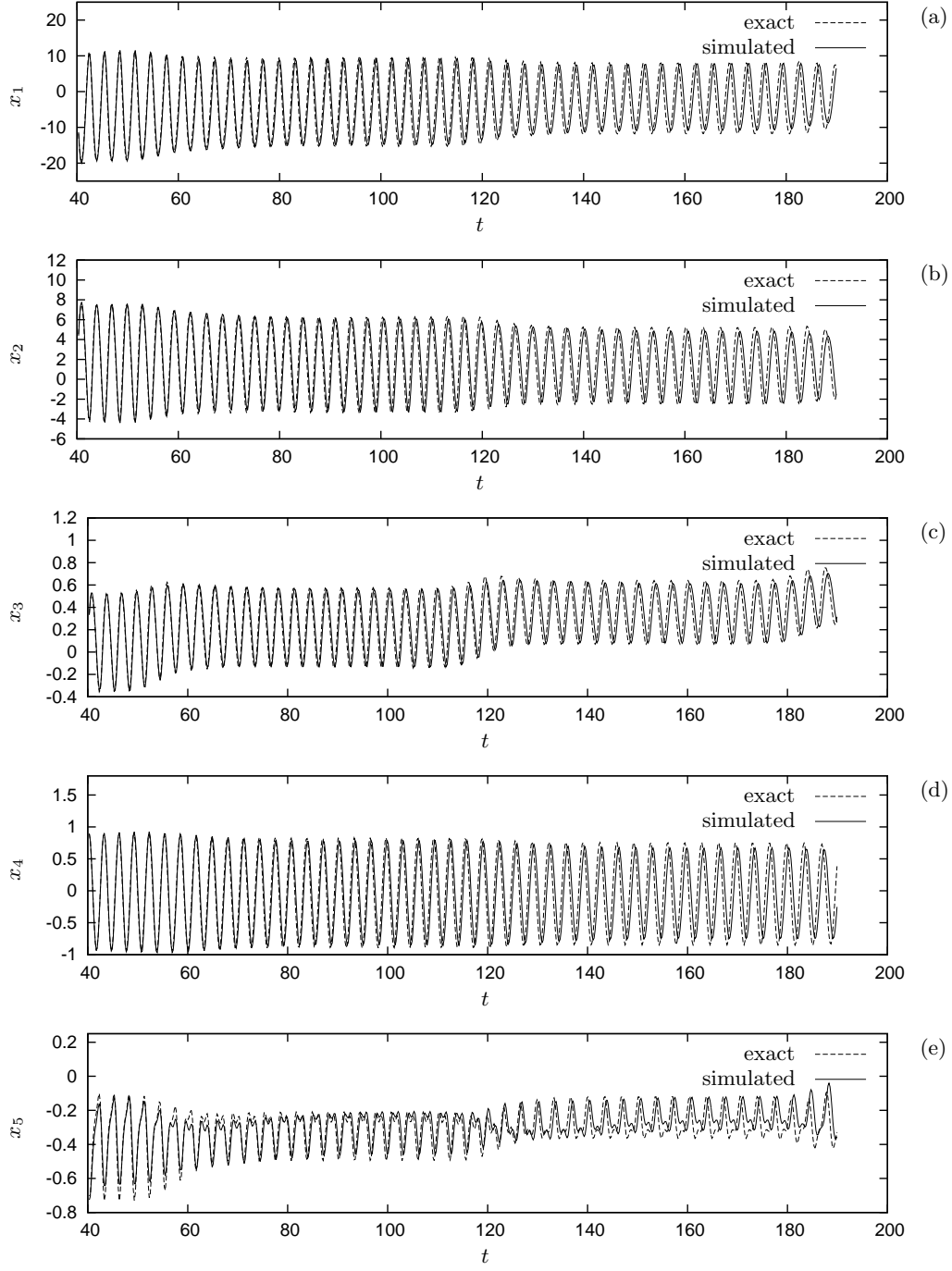


FIGURE 14. Comparison between the POD trajectory of the testing data-set, and the model-simulated POD trajectory (detailed view).

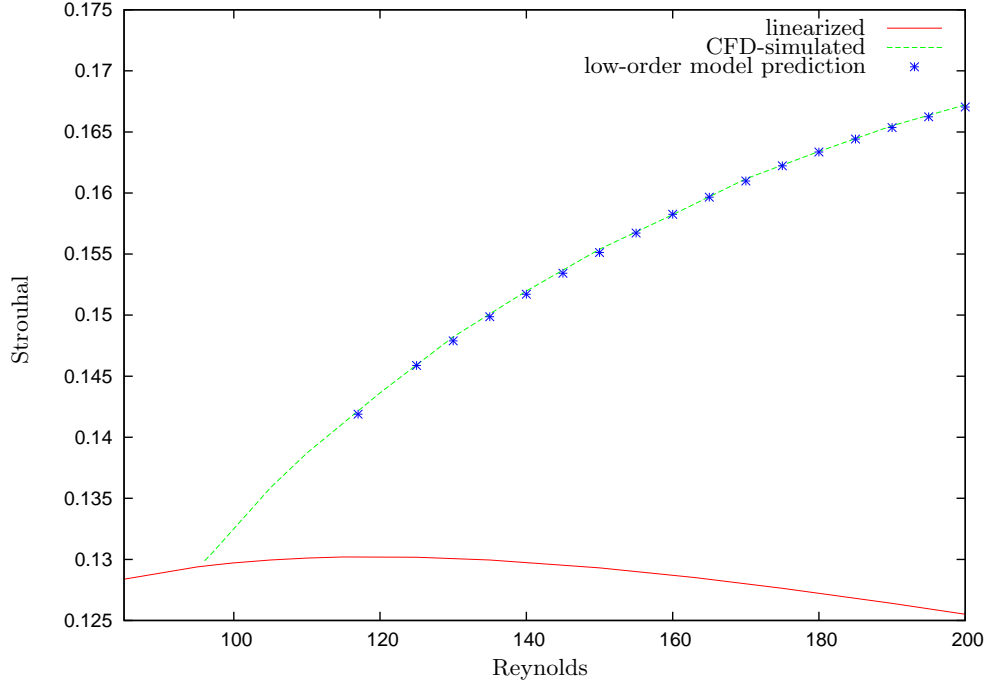


FIGURE 15. Strouhal number variations of the low-order model. Although the frequencies vary with the Reynolds number, the model is able to capture the system dynamics for each regime.

an unstable equilibrium point that corresponds to the base flow. This issue is particular important, since the base flow represents the only accessible steady point of the governing Navier-Stokes equations. Such a point can further be used as a control objective, as will be shown later.

From the reduced-order model, the base-flow X_{200} at $Re = 200$ can be obtained by solving $\Phi(X_{200}) = 0$ in (3.6). We may then compare this structure to the true base-flow projected onto the five POD modes. Even though such a comparison would not be possible in an experimental setting, it is still instructive to assess the quality of the recovered base state using our numerical data. Figure 16 shows horizontal velocity iso-contours of both the true base flow projected onto the five POD modes (red contours) and the base flow recovered from the model (black contours); remarkable agreement is observed. This agreement can be quantified using the measure $F = 1 - \|\mathbf{v}_{\text{estim}} - \mathbf{v}_{\text{exact}}\| / \|\mathbf{v}_{\text{exact}}\| = 84\%$ where $\mathbf{v}_{\text{estim}}$ is the estimated projected base flow and $\mathbf{v}_{\text{exact}}$ is the exact base flow obtained using a Newton method. To conclude, even though at such high a Reynolds number the base flow can no longer be observed directly, we have demonstrated that it can nevertheless be approximated, via an analysis of the observed unsteady dynamics of the flow.

3.2. Modeling the effect of forcing

In this section, the effect of the input forcing is incorporated into the model. First, a discussion about the effect of control input on the high-energy modes will be presented in §3.2.1. A new learning data-set and model structure will then be introduced in §3.2.2 to account for the effect of the control input. The identification of the newly introduced

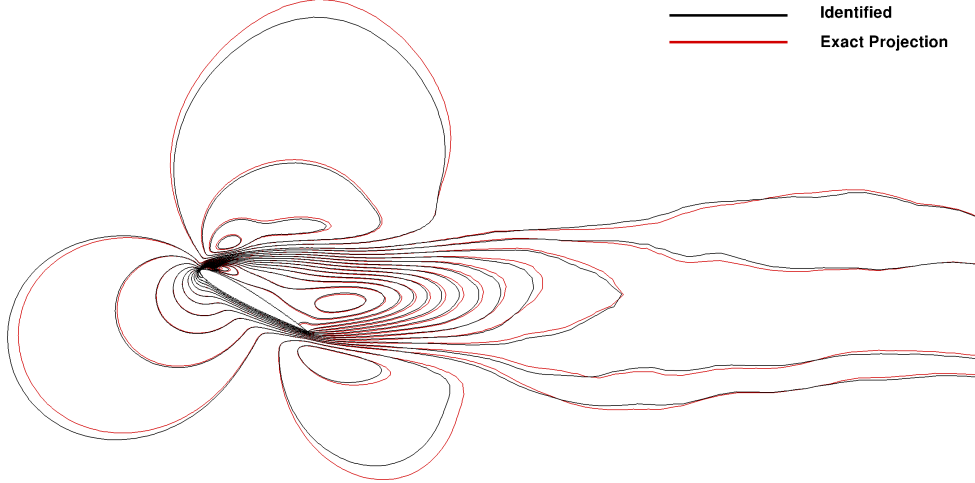


FIGURE 16. Comparison (for $Re = 200$) between the exact projected base flow (in red) and the model-identified base flow (in black). The iso-contours represent horizontal velocity.

coefficients will be performed in §3.2.3, and the final model will be validated against a new testing data-set.

3.2.1. Effect of control on high-energy POD modes and temporal reduction

Following a common Galerkin projection procedure, actuation by momentum forcing could directly be taken into account by adding a term $D_i u$ to the model structure given in (3.6) according to

$$x_i^{t+1} - x_i^t = \varepsilon A_i + \sum_j (B_{ij} + \varepsilon \beta_{ij}) x_j + \sum_{j,k} C_{ijk} x_j x_k + D_i u^t. \quad (3.9)$$

But such a model, with only a few high-energy POD modes, would fail to capture the actuation effect due to the small instantaneous impact of the control input on these modes. Generally speaking, flow control aims at significantly impacting the flow while expending as little energy as possible. For this reason, the control actuator is often located in sensitive regions, where a small energy input is amplified by some instability mechanism, leading to a large-scale modification of the system. The *instantaneous* effect of the control will still be weak on the high-energy POD modes. Inspection of the coefficients D_i , obtained by Galerkin projection, shows that their values are rather uniformly distributed among numerous POD modes and, more importantly, that they have a significant impact on several very-low-energy modes. Hence, while most of the energy is successfully captured by the first five POD modes of our model, the control input u affects both high- and low-energy modes. The forcing effects then propagate towards higher-energy modes due to nonlinear interactions and, after some time delay, ultimately affect the first five POD modes. Such a complex process can only be captured by a Galerkin-projection model if many POD modes are included in the model so as to capture the entire cascading action. However, this runs counter to model-reduction efforts in flow control which aim at rather small reduced systems.

In order to capture the effect of forcing input on the highest-energy POD modes, an supplementary term is added to the model which mimics the influence of the external

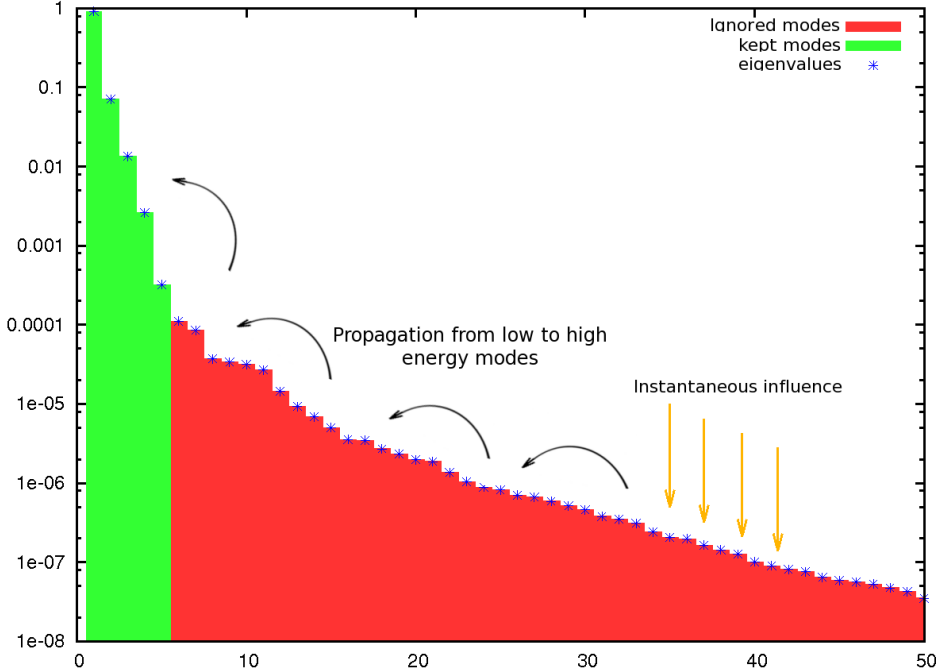


FIGURE 17. Eigenvalues of the correlation matrix associated with high-energy POD modes (see equ. (3.7)). The actuation instantaneously affects numerous low-energy POD modes and the nonlinear interactions associated with instability mechanisms propagate and amplify this energy towards large-scale structures. The highest-energy POD modes are influenced after some time delay.

forcing on these modes. This term is based on a delayed response of the system to a given energy input. It can be thought of as introducing a temporal reduction to our model, as opposed to the previous spatial reduction based on POD modes in §3.1.

3.2.2. Model structure with control input

A new simulation is performed at a fixed Reynolds number $Re = 200$ with stochastic external driving to obtain pertinent information about the influence of forcing input on the flow. We refer to the new data-set as the training data-set for actuation. Following the procedure described in §3.1.3, the corresponding exact POD trajectories, denoted by X_f , are extracted from the simulation snapshots to form a new data-set. We then focus on the part of the dynamics that is not predicted by the model identified in §3.1. To this end, we consider the following trajectories Δ which can be computed from X_f following

$$\Delta^t = X_f^{t+1} - X_f^t - \Phi(X_f^t) \quad (3.10)$$

where Φ is the function defined in (3.6) and the superscript t denotes the time index. Assuming that the original, unforced model Φ is sufficiently accurate, each instant Δ^t should only contain the part of the dynamics stemming from the forcing input u .

We now correlate the trajectories Δ^t with past control inputs. Following the arguments

given in §3.2.1, a linear relationship is postulated with

$$\Delta^t = \underbrace{\sum_{k=0}^{n_u} \alpha_k u^{t-k}}_{\Psi(u^t, \dots, u^{t-n_u})} \quad (3.11)$$

where each coefficient α_k is a 5×1 vector (for a 5-dimensional basis). The identification simply consists in finding a set of coefficients α_k which minimizes the quadratic error of the model over the training data-set for actuation. Contrary to §3.1, where a spatial reduction has been used (i.e., the POD algorithm), (3.11) represents a temporal reduction. Similar models have been used in Hervé *et al.* (2012) to model convective instabilities of a linearly stable flow over a backward-facing step. The number of coefficients to identify is equal to $5 \times (n_u + 1)$, where n_u is the temporal regression window (which has yet to be defined). Performing the regression for (3.11) involves an inexpensive pseudo-inverse, thus allowing a rather large temporal regression window n_u . This is in contrast to the strong constraints that apply to the number of POD modes mentioned in §3.1.

3.2.3. Identification and validation of the model

The randomly forced simulation is run sufficiently long so that the resulting data-set can be separated into two distinct subsets: one will be used for training, and the other for validation. To determine the temporal regression window (which is given by the coefficient n_u in (3.11)), different models with increasing values of n_u have been tested until satisfactory results were obtained. A value of $n_u = 50$ has been found optimal which corresponds to a non-dimensional time window of $t = 10$ (owing to the simplicity of the identification algorithm, this optimization can be performed very rapidly). Figure 18 compares, for the testing data-set, the five trajectories of Δ with the five trajectories of Ψ , as defined in (3.11). We observe that the model provides acceptable predictions of the effects of control input.

After the unforced dynamics and the influence of the control input have been identified, we can combine both components to form the final model

$$X^{t+1} - X^t = \Phi(X^t, \varepsilon^t) + \Psi(u^t, \dots, u^{t-n_u}) \quad (3.12)$$

where Φ has been defined in (3.6) and Ψ in (3.11). In a final test, figure 19 shows the results of a simulation of the complete model over the testing data-set shown in figure 18. The predicted shear-stress measurement m is compared to the measured value obtained from the direct numerical simulation. It shows that the model successfully predicts the flow behavior, even when strongly driven by an external input.

4. Control design

In this section, we will design a controller based on the model that was established in the previous section and assess its performance with the help of a numerical simulation. The design of an observer which provides the POD-state X from available real-time information m would be a necessary step in a realistic setup. However, this estimation problem is beyond the scope of this article. Instead, the simulation code will directly provide a state-space vector X at each time step (via a projection of the current flow state onto the five POD modes). In an experimental setup, a fast TR-PIV system could be used in a similar way to determine the reduced state. This reduced state will then be given to the controller which, in turn, will provide a control signal u to the numerical code.

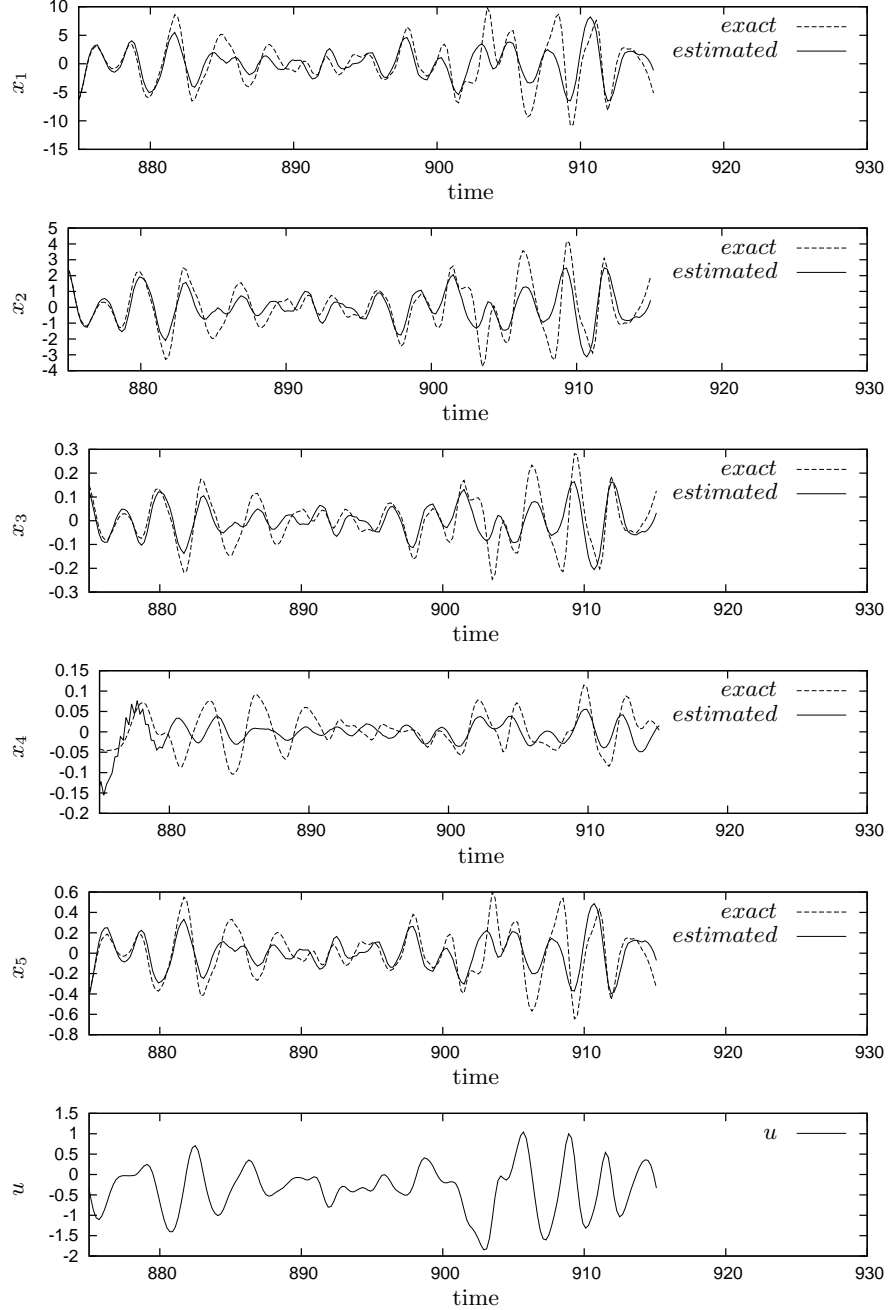


FIGURE 18. Identification results for the testing data-set with stochastic forcing. Comparison of the five trajectories of Δ and the five trajectories of Ψ . The bottom figure displays the control law $u(t)$ that was chosen. Note the different scales on the subfigures.

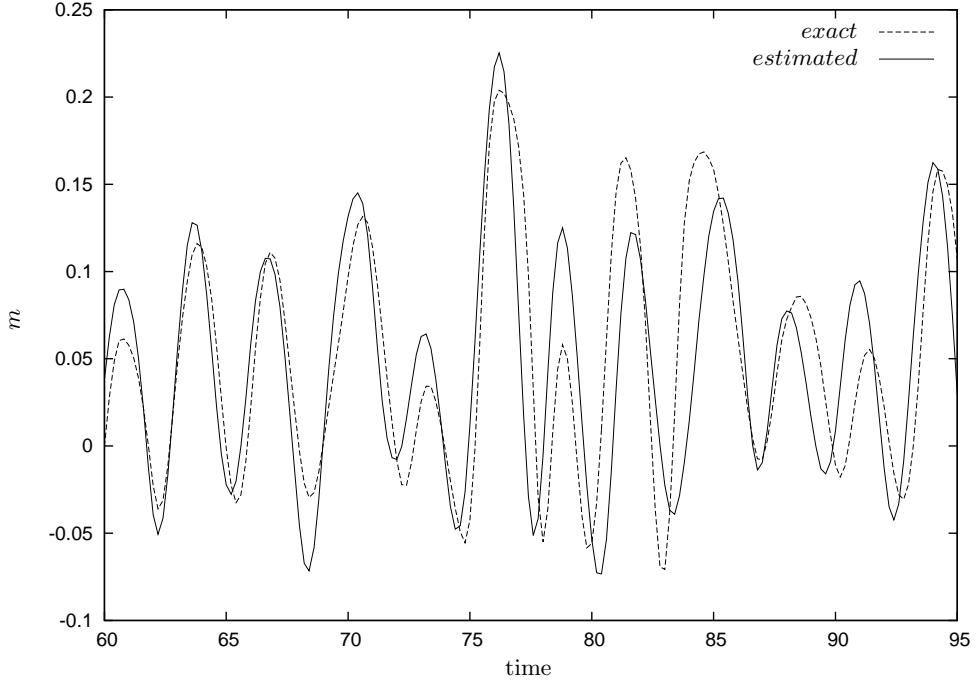


FIGURE 19. Comparison of exact and estimated shear-stress measurements for the testing data-set presented in figure 18. The reduced-order model is defined by (3.12)

4.1. Model-predictive control algorithm

We will introduce and apply model-predictive control (MPC) to suppress vortex shedding at $Re = 200$. For a given initial condition $X(t = 0)$, our model (3.12) will be used to predict the behavior of the system for any control strategy u . The controller then aims at determining the control u that minimizes a given objective functional over a specified time horizon. As mentioned in §2, a possible control objective could be the return towards the base flow. The objective functional may either directly target the kinetic energy of the fluctuations about this fixed-point, in which case $J = \sum_k (X_k - X_{k,200})^2$, or it may minimize the associated shear-stress measurement with $J = (CX - CX_{200})^2$ and C as the measurement matrix consisting of $m(\phi_k)$ (see equation (3.3)). In our study, we choose the objective functional based on the measurement and evaluate the controller's performance by its ability to reduce fluctuations in m .

Equation (3.12) can be rewritten as

$$X^{t+1} = f(X^t) + Bu^t \quad (4.1a)$$

$$m^t = CX^t, \quad (4.1b)$$

where X^t is now an *augmented* reduced state comprising the five POD coefficients as well

as past control inputs, i.e.,

$$X^t = \begin{bmatrix} x_1^t \\ \vdots \\ x_5^t \\ u^{t-1} \\ \vdots \\ u^{t-n_u} \end{bmatrix}. \quad (4.2)$$

In the above expression, f is a nonlinear quadratic function deduced from Φ and Ψ while the matrix B takes into account the instantaneous impact of u on the model. The functional to be minimized by the controller is defined as

$$J^t = \frac{1}{2} \sum_{i=t}^{t+N} [(CX^i - CX_{200}^i)^2 + \ell^2(u^i)^2] \quad (4.3)$$

where N defines the time-horizon over which the functional is to be minimized (N has yet to be specified). We use a standard Lagrangian technique (see, e.g., Gunzburger & Wood 2003) to minimize (4.3) subject to the model equation (4.1). First variations with respect to all involved variables yields a system of optimality conditions which reads

$$Z^{i+1} = f(Z^i) + Bu^i \quad i = 1, \dots, N-1 \quad (4.4a)$$

$$Z^1 = X^t \text{ (measured)} \quad (4.4b)$$

$$P^{i-1} = (\nabla_f(Z^i))^* P^i + C^* C (Z^i - X_{200}) \quad i = N, \dots, 2 \quad (4.4c)$$

$$P^N = 0 \quad (4.4d)$$

$$0 = \ell^2 u^i + B^* \cdot P^i \quad i = 1, \dots, N \quad (4.4e)$$

reminiscent of a nonlinear direct-adjoint system. Such a system can be solved by an iterative process, described as follows:

Step 0. We first measure the state vector X^t and initialize the remaining variables as follows: $u = 0$, $P^N = 0$, $Z^1 = X^t$.

Step 1. The direct equation (4.4a) is iterated $N-1$ times to obtain the vector $Z = [Z^1, \dots, Z^N]$.

Step 2. Using the solution Z from the previous step, the adjoint equation (4.4b) is iterated (backward in the time index) $N-1$ times to update the vector $P = [P^1, \dots, P^N]$.

Step 3. Based on (4.4c) the control law u is updated using an underrelaxation coefficient α according to

$$u := \alpha \left(-\frac{B^* P}{\ell^2} \right) + (1 - \alpha) u,$$

Step 4. The objective functional J in (4.3) is evaluated and convergence of the algorithm is checked.

Step 5. If convergence has not yet been reached, we return to **Step 1**.

Step 6. If convergence has been achieved, the vector $u = [u^1, \dots, u^N]$ contains the optimal control law, while Z contains the predicted future states $[X^{t+1}, \dots, X^{t+N}]$.

We stress that this algorithm uses a constant relaxation coefficient α , which is not optimal; an adaptive strategy for α would improve both convergence and robustness. How-

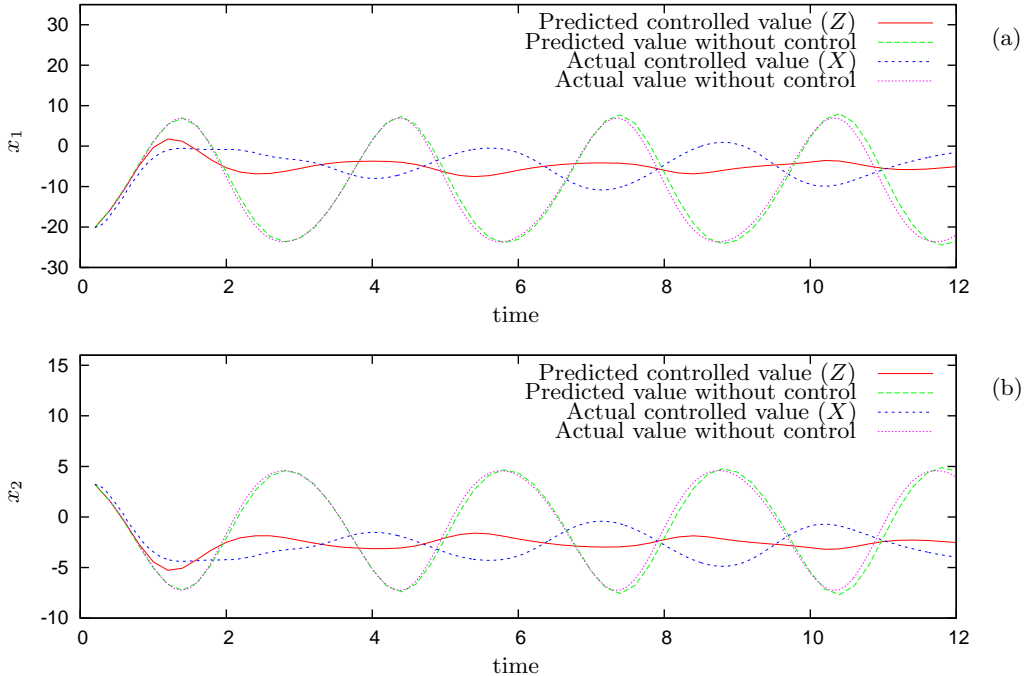


FIGURE 20. Comparison between the modeled state-values and the state-values of the numerical simulation. Time traces of the first (a) and second (b) POD-mode are shown.

ever, our initial attempt with constant α produced fast and satisfactory results such that further development of the above algorithm seemed unwarranted.

4.2. Control results

The model-predictive controller defined by the algorithm above is now applied to the numerical simulation and its overall performance is assessed. As explained above, the control strategy is computed in a *full-state information framework*, where the reduced state $[x_1 \dots x_5]$ is assumed to be known. This reduced state may be obtained by projecting the current flow field (from simulations or TR-PIV measurements) onto the POD basis each time a control input has to be determined. The time horizon in (4.4) is set to $N = 100$ which corresponds to a time window of length 20, since the time-step for the reduced-order model is $\Delta t = 0.2$; this window length corresponds to approximately six periods of the flow oscillations. To avoid error propagation, the control law is updated every 20 time steps of the numerical simulation.

Figure 20 shows results from applying the MPC strategy to our simulations over a time span from $t = 0$ to $t = 20$. Given an initial state, the low-order model predicts the system evolution without control (green line). The iterative optimization process then determines the control signal, and the controlled low-order model subsequently predicts a signal evolution (red line) for which the cost functional J is minimized. Applying this control law to the numerical simulation finally yields controlled states (blue line); this latter signal can *a posteriori* be compared to the uncontrolled state (magenta line).

Figure 21 shows the reduction of the shear-stress measurement fluctuations that can be achieved by applying the controller. We notice a significant drop in both the mean value (which moves closer to the base-flow value) and the variance of the measurement

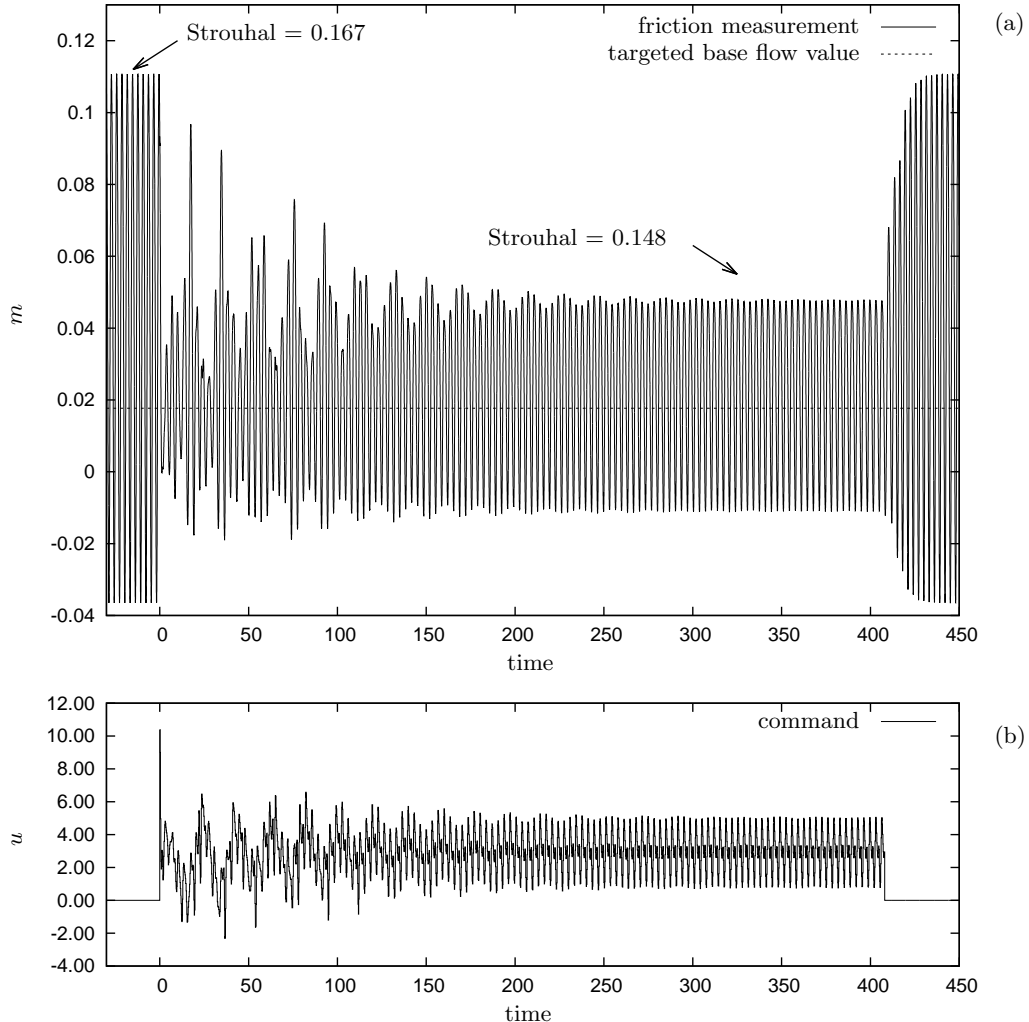


FIGURE 21. Performance analysis of the controller. Time evolution of the shear-stress measurement m (a) and its associated control signal (b). The controller is switched on at $t = 0$ and switched off at $t = 408$.

fluctuations (which is reduced by about 83%). The Strouhal number decreases from 0.167 to 0.148 (where 0.125 corresponds to the linearized Strouhal number, see figure 15). The control signal necessary to achieve this reduction is also displayed in figure 21.

In accordance with earlier displays of the measurement signal, figure 22 shows the control results in the phase-space (m, \dot{m}). The transient that can be observed between $t = 0$ and $t = 100$ in figure 21 has been omitted; only the asymptotic state is visualized in phase-space. We observe that the flow reaches a new limit cycle, whose amplitude is significantly reduced when compared to the uncontrolled case; we also notice that the controller achieves a net-reduction of the mean shear-stress value. Although the base-flow value is not fully reached, figure 22 demonstrates that the controller efficiently drives the flow dynamics towards the identified base-flow state.

Figure 23 depicts contours of the time-averaged kinetic energy fluctuations about the

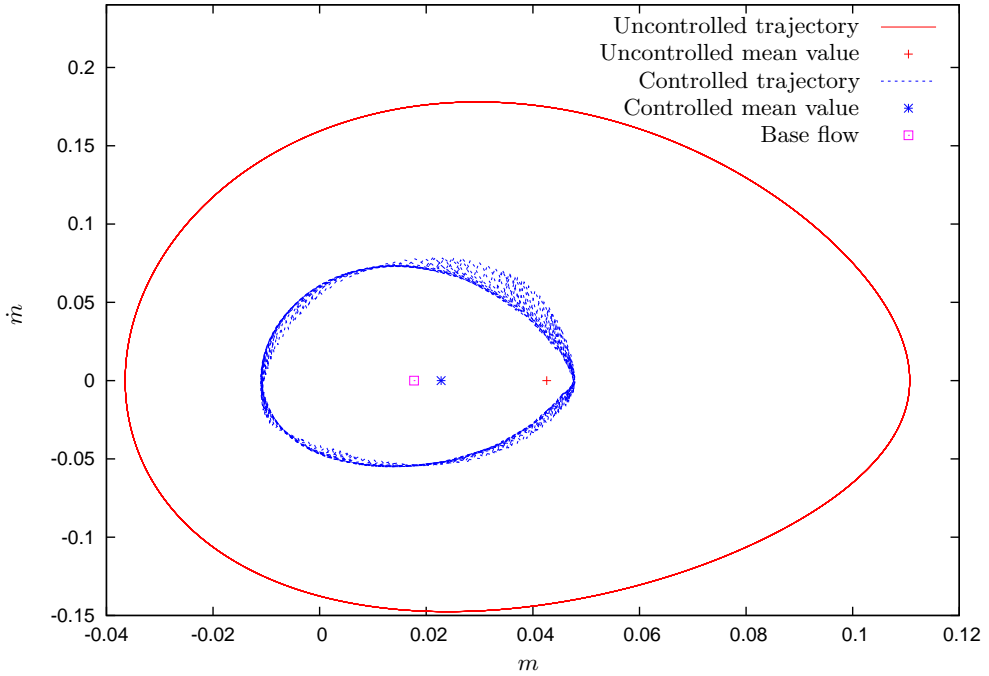


FIGURE 22. Phase portrait (m, \dot{m}) of the uncontrolled and controlled case (transients are not shown for more clarity). Red: uncontrolled simulation. Blue: controlled simulation. The control efficiently reduces the amplitude of the limit cycle, and the obtained mean-value shifts towards the base-flow value.

base flow, i.e., $\overline{u_x^2 + u_y^2}$ where $u' = u - u_{baseflow}$, for both a controlled and an uncontrolled simulation. The maximum peak of perturbation energy is decreased by about 20%, and the recirculation bubble is slightly increased. The streamlines are computed based on the time-averaged flow.

5. Conclusions

The flow over a NACA-0012 airfoil has been investigated as a typical supercritical oscillator flow in which nonlinearities play a dominant role in the flow dynamics. Rather than using a model-based approach where the flow dynamics are postulated *a priori* before applying reduction techniques, the modeling process in this study has been based only on flow observations which potentially could be extracted from an experiment. The modeling process involved a POD computation, where a customized scalar product successfully enforced observability of the extracted basis. A nonlinear auto-regressive (NARX) structure, with an explicit Reynolds number dependence, has then been used to model the unforced oscillations of the flow. The identified model recovers the observable dynamics of the flow and, as a by-product, retrieves the base flow which subsequently acts as a target for our control efforts. The influence of external forcing terms on the retained POD modes is then taken into account via a simple linear model that represents the transfer of energy between the control signal and the high-energy structures used in the NARX model. The nonlinear identified model shows good accuracy in capturing the flow dynamics on the limit cycle for $Re = 200$. Finally, a nonlinear control law is applied using a standard Lagrangian optimization algorithm and a model-predictive framework.

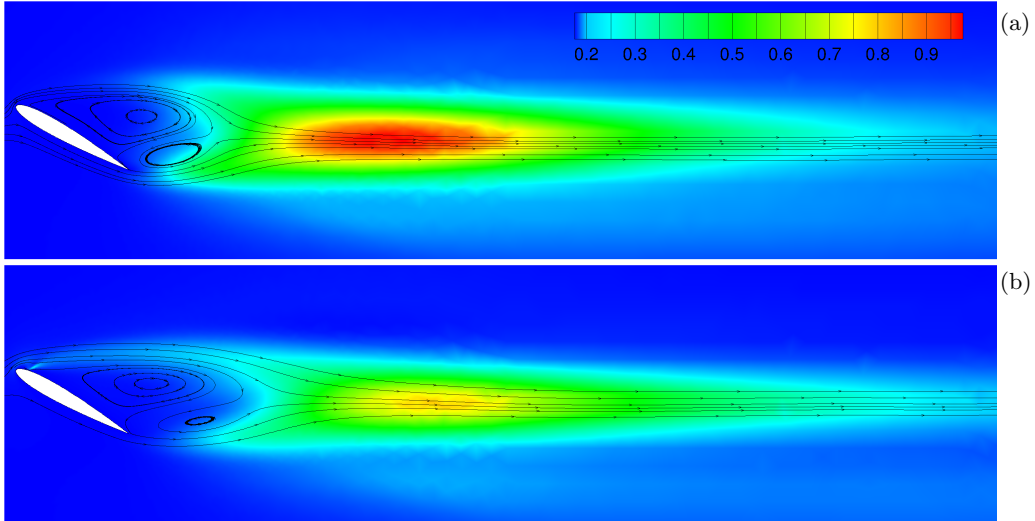


FIGURE 23. Control results visualized by contours of the time-averaged perturbation energy ($v'_x^2 + v'_y^2$): (a) uncontrolled simulation, (b) controlled simulation. Streamlines are added to the averaged flow. The peak of the perturbation energy is reduced by 20%.

The control results are encouraging and promising, as the objective functional could be drastically reduced.

Although the designed model successfully drives the flow towards the base state, the latter is not fully reached. Nonetheless, this process could be viewed as a first step of an iterative modeling process. Indeed, our results show that the controlled flow behaves rather differently from the uncontrolled saturated flow: the Strouhal number of the controlled flow falls between the uncontrolled and the base-flow Strouhal number. The controlled behavior of the flow could be used to perform a second identification step in which additional dynamics of the flow can be observed. This procedure could, for instance, be performed in the spirit of Morgans & Dowling (2007); Illingworth *et al.* (2011) where a first (preliminary) controller has to be used to perform the identification of a new model, after which a correction will provide a more robust and efficient (final) controller. The exploration of this approach is left for a future effort.

REFERENCES

- AHUJA, S. & ROWLEY, C.W. 2010 Feedback control of unstable steady states of flow past a flat plate using reduced-order estimators. *J. Fluid Mech.* **645**, 447–478.
- AKERVIK, E., HOEPFFNER, J., EHRENSTEIN, U. & HENNINGSON, D.S. 2007 Optimal growth, model reduction and control in a separated boundary-layer flow using global eigenmodes. *J. Fluid Mech.* **579**, 305–314.
- BARBAGALLO, A., SIPP, D. & SCHMID, P.J. 2009 Closed-loop control of an open cavity flow using reduced-order models. *J. Fluid Mech.* **641**, 1–50.
- BARKLEY, D. 2006 Linear analysis of the cylinder wake mean flow. *Europhys. Lett.* **75** (5), 750.
- BERGMANN, M. & CORDIER, L. 2008 Optimal control of the cylinder wake in the laminar regime by trust-region methods and POD reduced-order models. *J. Comp. Phys.* **227** (16), 7813–7840.
- BERGMANN, M., CORDIER, L. & BRANCHER, J.-P. 2005 Optimal rotary control of the cylinder wake using proper orthogonal decomposition reduced-order model. *Phys. Fluids* **17** (9).
- CATTAFESTA, L.N., SONG, Q., WILLIAMS, D.R., ROWLEY, C.W. & ALVI, F.S. 2008 Active control of flow-induced cavity oscillations. *Prog. Aerosp. Sci.* **44** (78), 479–502.

- CATTAFFESTA, L., WILLIAMS, D. R., ROWLEY, C. W. & ALVI, F. 2003 Review of active control of flow-induced cavity resonance. *AIAA Paper* **3567**.
- CORDIER, L., EL MAJD, B.A. & FAVIER, J. 2010 Calibration of POD reduced-order models using Tikhonov regularization. *Int. J. Num. Meth. Fluids* **63** (2), 269–296.
- GALLETTI, B., BRUNEAU, C.H., ZANNETTI, L. & IOLLO, A. 2004 Low-order modelling of laminar flow regimes past a confined square cylinder. *J. Fluid Mech.* **503**, 161–170.
- GLOWINSKI, R. 2003 Finite element methods for incompressible viscous flow. In *Numerical Methods for Fluids (Part 3)* (ed. P.G. Ciarlet & J.L. Lions), *Handbook of Numerical Analysis*, vol. 9, pp. 3–1176. Elsevier.
- GUNZBURGER, M. & WOOD, H. 2003 Perspectives in Flow Control and Optimization. *Appl. Mech. Rev.* **56**, B82.
- HE, J.-W. AND GLOWINSKI, R., METCALFE, R., NORDLANDER, A. & PERIAUX, J. 2000 Active control and drag optimization for flow past a circular cylinder: I. Oscillatory cylinder rotation. *J. Comp. Phys.* **163** (1), 83–117.
- HERVÉ, A., SIPP, D., SCHMID, P.J. & SAMUELIDES, M. 2012 A physics-based approach to flow control using system identification. *J. Fluid Mech.* **702**, 26–58.
- HUANG, S.-C. & KIM, J. 2008 Control and system identification of a separated flow. *Phys. Fluids* **20** (10), 101509.
- ILLINGWORTH, S.J., MORGANS, A.S. & ROWLEY, C.W. 2011 Feedback control of flow resonances using balanced reduced-order models. *J. Sound Vibr.* **330** (8), 1567–1581.
- LJUNG, L. 1999 *System Identification: Theory for the User*, 2nd edn. Prentice Hall.
- MORGANS, A.S. & DOWLING, A.P. 2007 Model-based control of combustion instabilities. *J. Sound Vibr.* **299** (12), 261–282.
- PROTAS, B. & WESFREID, J.E. 2002 Drag force in the open-loop control of the cylinder wake in the laminar regime. *Phys. Fluids* **14**, 810–826.
- ROWLEY, C.W. 2005 Model reduction for fluids using balanced proper orthogonal decomposition. *Int. J. Bifurc. Chaos* **15** (3), 997–1013.
- SIPP, D. & LEBEDEV, A. 2007 Global stability of base and mean flows: a general approach and its applications to cylinder and open cavity flows. *J. Fluid Mech.* **593**, 333–358.
- SIPP, D., MARQUET, O., MELIGA, P. & BARBAGALLO, A. 2010 Dynamics and control of global instabilities in open flows: A linearized approach. *Appl. Mech. Rev.* **63** (3), 030801.
- SIRISUP, S. & KARNIADAKIS, G.E. 2004 A spectral viscosity method for correcting the long-term behavior of POD models. *J. Comp. Phys.* **194** (1), 92–116.
- TOKUMARU, P.T. & DIMOTAKIS, P.E. 1991 Rotary oscillation control of a cylinder wake. *J. Fluid Mech.* **224**, 77–90.

Conclusions

Cette thèse a eu pour objectif de proposer un formalisme permettant d'utiliser des techniques d'identification de modèles réduits pour le contrôle optimal en boucle fermée d'écoulements instationnaires. Les méthodes développées ici s'inscrivent dans le cadre d'une étude théorique et montrent des résultats très encourageants quant à de futures applications possibles. Un accent particulier est mis sur la possibilité d'utiliser les méthodes développées dans un cadre expérimental, bien que les travaux présents se limitent à des applications numériques. En effet, les méthodes d'identification présentées ne requièrent pour leur application que des données que les moyens modernes de métrologie sont capables d'apporter (par TR-PIV, ou mesures instationnaires de frottements pariétaux).

4.1 Bilan des travaux présentés

A travers l'étude de deux écoulements, plusieurs problématiques sont isolées, puis traitées dans une optique de modélisation par identification. Dans chaque cas, une étude qualitative des équations gouvernant la dynamique est réalisée, et permet de définir une structure de modèle adaptée à l'écoulement. C'est cette évaluation physique qui permet d'obtenir de bons résultats, mais surtout d'envisager une généralisation des modèles obtenus dans différents cas d'application.

Pour modéliser les oscillations auto-entretenues de l'allée tourbillonnaire, on associe une base POD à un modèle non-linéaire capable de s'adapter à différents régimes de l'écoulement saturé. La dimension du modèle est fixée par le nombre de modes POD considérés, et permet de représenter la dynamique libre de l'écoulement avec un nombre de modes très faible (5 modes sont utilisés). L'utilisation des modes POD n'est pourtant pas pertinente dans tous les cas, notamment pour la modélisation de structures dont l'évolution spatiale est importante. Pour des phénomènes comme les instabilités convectives de la marche, mais également l'influence du contrôle dans l'écoulement de NACA012, on introduit plutôt des modèles dont l'objectif est de lier directement une entrée à une sortie. La dimension du modèle est alors fixée par une fenêtre temporelle utilisée pour décrire explicitement une fonction de transfert, au moyen de modèles ARX/ARMAX. Cette approche montre de bons résultats, et permet de simplifier la modélisation dans des cas où un grand nombre de modes POD aurait été nécessaire pour obtenir des performances comparables.

La volonté de se placer dans un cadre pseudo-expérimental pose des difficultés supplémentaires auxquelles des réponses sont proposées au cours de cette thèse. Le cas des amplificateurs de bruit pose comme principale difficulté la prise en compte des perturbations extérieures qui excitent l'écoulement, sans que l'on puisse pour autant mesurer ces dernières en conditions réelles. Plutôt que de supposer connaître leur distribution spatiale ou temporelle (comme c'est le cas dans les méthodes utilisant le filtre de Kalman ([Bagheri](#)

(et al., 2009; Barbagallo et al., 2012)), l'emploi d'un capteur amont comme substitution à la source de bruit permet de dériver un modèle ARMAX capable de prévoir avec une grande précision les fluctuations du système. L'ajout de bruit de capteurs, ou encore d'une source de perturbations non détectables dans l'écoulement permet en outre de montrer une remarquable robustesse du modèle, et en fait un candidat tout à fait plausible pour une future réalisation expérimentale.

Dans le cas des écoulements oscillants, c'est plutôt la nature fortement non-linéaire de l'écoulement et l'impossibilité d'observer le champ de base qui nécessitent une attention particulière. Pour palier à ces difficultés, on introduit un modèle non-linéaire basé sur une étude qualitative des équations gouvernant la dynamique de l'écoulement. On montre notamment que l'étude du champ saturé oscillant permet d'obtenir suffisamment d'informations pour construire un modèle non-linéaire capable de prévoir avec une bonne précision la dynamique de l'écoulement. De surcroît, la dynamique identifiée permet d'isoler un point fixe du modèle réduit. Le calcul numérique du champ de base permet de confirmer que le point fixe du modèle réduit correspond effectivement au point fixe de la dynamique identifiée. Ainsi, l'identification du modèle réduit d'après l'observation de la branche chaotique instationnaire permet d'obtenir des informations sur la position du champ de base, sans observation explicite de ce dernier. Le champ de base identifié peut alors être utilisé comme objectif de contrôle.

Pour chaque écoulement, un contrôle numérique est réalisé. Sans grande surprise, les performances finales des différents cas étudiés dépendent principalement de la qualité du modèle réduit utilisé. Dans chaque configuration, le contrôle permet une réduction significative des fluctuations de l'écoulement, et les résultats obtenus semblent particulièrement encourageants.

4.2 Perspectives futures

Si cette thèse a pour ambition de s'approcher du domaine expérimental, il reste toutefois de nombreux paramètres à explorer.

Estimateur temps réel La première avancée à réaliser est sans doute l'établissement d'un estimateur destiné au contrôle non-linéaire de l'écoulement de profil NACA012. En effet, bien que toutes les données utilisées pour la construction du modèle non-linéaire soient disponibles en conditions expérimentales, elle ne le sont pas nécessairement en temps réel. Dans l'article de la partie 3 apparaît la nécessité d'évaluer l'état des modes POD en temps réel pour le calcul d'une loi de contrôle. On parle en général d'estimateur, qui consiste en un système dynamique dont le rôle est d'évaluer l'état POD X à partir de mesures disponibles en temps réel. C'est en réalité par manque de temps que cette étape n'a pu être achevée, plutôt qu'en raison de la difficulté qu'elle pose. L'idée la plus basique consiste à estimer l'état d'après un vecteur de mesures instantanées. En effet, s'il est possible de prévoir une ou plusieurs mesure(s) d'après une combinaison linéaire de l'état $m = CX$, alors l'état peut être estimé par une simple multiplication de la matrice pseudo-inverse : $X = C^+m$. Des résultats préliminaires (non publiés ici) montrent que cette méthode permet de recouvrir les deux premiers modes POD avec une précision

presque parfaite en utilisant 5 mesures de frottements répartis sur l'aile. Pour déterminer le reste des modes, un filtre de Kalman étendu serait probablement la solution la plus efficace. Cette approche tend toujours à minimiser l'objectif $\|m - CX\|$, mais cette fois en ajoutant la contrainte $X^t = f(X^{t-1})$, afin de respecter la dynamique du modèle f . On parle de Kalman étendu lorsque f n'est pas linéaire, ce qui est le cas ici.

Amélioration des modèles par itérations successives Si le modèle proposé en §3 donne de bons résultats, il est probable que ceux-ci puissent être améliorés à travers un processus d'apprentissage itératif. En effet, la dynamique au voisinage du champ de base est sensiblement différente de celle au voisinage du cycle limite libre. Il serait donc plus intéressant d'observer le comportement de l'écoulement au voisinage du champ de base, mais ceci ne peut être réalisé qu'en possédant déjà un système de contrôle. Une fois un premier contrôleur défini par les méthodes introduites ici, il devient possible de s'approcher du champ de base. On peut alors imaginer se servir de ce premier contrôleur afin d'explorer la dynamique de l'écoulement dans un comportement plus proche de l'équilibre. Cette approche pourrait être envisagée à la manière de [Morgans and Dowling \(2007\)](#); [Illingworth et al. \(2011\)](#), en considérant l'écoulement contrôlé comme un nouveau système à identifier, ou même plus simplement en observant la dynamique de relaxation obtenue lorsque l'on éteint le contrôleur. Il est probable qu'un tel procédé puisse grandement améliorer la qualité du modèle final.

Adaptation du modèle aux conditions de vitesse Dans la partie 3, la première partie de la modélisation fournit un modèle capable de s'adapter à des changements de nombre de Reynolds. Cette propriété est vue comme un effet secondaire dû au choix de varier le nombre de Reynolds pour améliorer la précision du modèle à $Re = 200$, et n'est pas exploitée par la suite. En particulier, l'addition du modèle linéaire incluant le contrôle fixe le nombre de Reynolds pour lequel le modèle complet peut fonctionner. Il pourrait toutefois être intéressant de faire varier les coefficients du modèle linéaire en fonction du Reynolds, afin d'obtenir un modèle complet adaptatif en Reynolds. Des premiers résultats (non montrés ici) laissent penser qu'il serait assez envisageable d'identifier plusieurs modèles linéaires correspondant à des Reynolds différents pour un coût de calcul relativement faible. Une interpolation entre les différents coefficients obtenus semble possible, et mènerait à un modèle complet adaptatif. Cet aspect serait particulièrement intéressant à développer pour des raisons de robustesse. En effet, une faible variation du nombre de Reynolds (due par exemple à un changement de régime de vitesse en conditions de vol) peut rapidement provoquer des problèmes en contrôle par boucle fermée. La possibilité d'obtenir un contrôle adaptatif en Reynolds est donc particulièrement séduisante pour de futures applications pratiques.

Écoulements tridimensionnels Parmi les extensions possibles de ces travaux, on envisage également l'application des méthodes proposées dans des cas 3D. Des travaux comme ceux de [Semeraro et al. \(2011\)](#) montrent qu'un contrôle linéaire d'écoulement amplificateur est possible en utilisant une rangée de capteurs et d'actuateurs (cas de couche limite). Cette configuration semble tout à fait accessible aux méthodes d'identification,

puisque il est possible de superposer les différentes fonctions de transfert correspondant à chaque sortie dans le cadre linéaire. Il est assez probable qu'une étude de ce type soit à envisager avant d'envisager un protocole expérimental.

Essai en conditions expérimentales réelles L'emploi des méthodes d'identification de système se justifie presque exclusivement par la perspective qu'elles ouvrent en vue d'une application pratique. Bien que les travaux présentés ici aient été orientés dans cette direction, un grand nombre de paramètres liés à l'expérience n'ont pas été pris en compte, et il serait particulièrement intéressant de pouvoir confronter l'utilisation des méthodes de réduction de modèle par identification à un cas expérimental.

Effets des hauts nombres de Reynolds Enfin, plus ambitieuse serait l'étude de la modélisation en conditions compressibles, et à hauts nombres de Reynolds. La modélisation par identification fait intervenir des méthodes statistiques, et de la même manière qu'ici l'identification apporte une robustesse au modèle (en comparaison des méthodes de Galerkin utilisant la même structure de modèle), on pourrait espérer qu'une identification fasse apparaître un comportement filtré apparent d'une dynamique trop complexe pour être approchée de manière exacte. Ce point est probablement le plus ambitieux parmi ceux énoncés ici, mais il est aussi l'un des objectifs qu'il sera nécessaire d'atteindre afin de pouvoir porter les systèmes de contrôle actif en boucle fermée vers des applications industrielles.

Bibliographie

- Ahuja, S. and Rowley, C. (2010). Feedback control of unstable steady states of flow past a flat plate using reduced-order estimators. *J. Fluid Mech.*, 645 :447–478.
- Akers, J. and Bernstein, D. (1997). Armakov least-squares identification. In *American Control Conference, 1997. Proceedings of the 1997*, volume 1, pages 186 –190 vol.1.
- Akervik, E., Hoepffner, J., Ehrenstein, U., and Henningson, D. (2007). Optimal growth, model reduction and control in a separated boundary-layer flow using global eigenmodes. *Journal of Fluid Mechanics*, 579 :305–314.
- Antoulas, A. C. (2005). *Approximation of Large-Scale Dynamical Systems (Advances in Design and Control)*. Society for Industrial and Applied Mathematics, Philadelphia, PA, USA.
- Bagheri, S., Brandt, L., and Henningson, D. S. (2009). Input/output analysis, model reduction and control of the flat-plate boundary layer. *Journal of Fluid Mechanics*, 620(-1) :263–298.
- Bagheri, S. and Henningson, D. S. (2011). Transition delay using control theory. *Royal Society of London Philosophical Transactions Series A*, 369 :1365–1381.
- Barbagallo, A., Dergham, G., Sipp, D., Schmid, P., and Robinet, J.-C. (2012). Closed-loop control of unsteadiness over a rounded backward-facing step. *J. Fluid Mech.*, 703 :326–362.
- Barbagallo, A., Sipp, D., and Schmid, P. (2009). Closed-loop control of an open cavity flow using reduced-order models. *J. Fluid Mech.*, 641 :1–50.
- Barkley, D. (2006). Linear analysis of the cylinder wake mean flow. *Europhys. Lett.*, 75(5) :750.
- Barkley, D., Gomes, M. G. M., and Henderson, R. D. (2002). Three-dimensional instability in flow over a backward-facing step. *Journal of Fluid Mechanics*, 473 :167–190.
- Bearman, P. W. and Harvey, J. K. (1993). Control of circular cylinder flow by the use of dimples. *AIAA Journal*, .31 :1753–1756.
- Bergmann, M., Bruneau, C.-H., and Iollo, A. (2009). Enablers for robust pod models. *Journal of Computational Physics*, 228(2) :516 – 538.
- Bergmann, M. and Cordier, L. (2008). Optimal control of the cylinder wake in the laminar regime by trust-region methods and pod reduced-order models. *J. Comp. Phys.*, 227(16) :7813–7840.
- Bergmann, M., Cordier, L., and Brancher, J.-P. (2005). Optimal rotary control of the cylinder wake using proper orthogonal decomposition reduced-order model. *Phys. Fluids*, 17(9).
- Berkooz, G., Holmes, P., and Lumley, J. (1993). The proper orthogonal decomposition in the analysis of turbulent flows. *Annual Review of Fluid Mechanics*, 25 :539–575.
- Bewley, T. R. and Liu, S. (1998). Optimal and robust control and estimation of linear paths to transition. *Journal of Fluid Mechanics*, 365(-1) :305–349.
- Blackburn, H., Barkley, D., and Sherwin, S. (2008). Convective instability and transient growth in flow over a backward-facing step. *Journal of Fluid Mechanics*, 603 :271–304.

- Boiko, A., Dovgal, A., and Hein, S. (2008). Control of a laminar separating boundary layer by induced stationary perturbations. *European Journal of Mechanics - B/Fluids*, 27(4) :466 – 476.
- Booker, A. J., Dennis, J. E., Frank, P. D., Serafini, D. B., Torczon, V., and Trosset, M. W. (1999). A rigorous framework for optimization of expensive functions by surrogates. *Structural and Multidisciplinary Optimization*, 17 :1–13. 10.1007/BF01197708.
- Cattafesta, L., Garg, S., Choudhari, M., and Li, F. (1997). Active control of flow-induced cavity resonance. In *AIAA, Fluid Dynamics Conference*.
- Cattafesta, L., Song, Q., Williams, D., Rowley, C., and Alvi, F. (2008). Active control of flow-induced cavity oscillations. *Prog. Aerosp. Sci.*, 44(7–8) :479–502.
- Cattafesta, L., Williams, D. R., Rowley, C. W., and Alvi, F. (2003). Review of active control of flow-induced cavity resonance. *AIAA Paper*, 3567.
- Chevalier, M., Høeppner, J., Åkervik, E., and Henningson, D. S. (2007). Linear feedback control and estimation applied to instabilities in spatially developing boundary layers. *Journal of Fluid Mechanics*, 588 :163–187.
- Choi, H., Jeon, W.-P., and Kim, J. (2008). Control of flow over a bluff body. *Annual Review of Fluid Mechanics*, 40 :113–139.
- Cordier, L., El Majd, B., and Favier, J. (2010). Calibration of POD reduced-order models using Tikhonov regularization. *Int. J. Num. Meth. Fluids*, 63(2) :269–296.
- Couplet, M., Basdevant, C., and Sagaut, P. (2005). Calibrated reduced-order pod-galerkin system for fluid flow modelling. *Journal of Computational Physics*, 207(1) :192 – 220.
- Crouch, J., Garbaruk, A., and Magidov, D. (2007). Origin of transonic buffet on airfoils. *APS Meeting Abstracts*, pages 3–+.
- Deck, S. (2005). Numerical simulation of transonic buffet over a supercritical airfoil. *American Institute of Aeronautics and Astronautics Journal*, 43(7).
- Dergham, G., Sipp, D., and Robinet, J.-C. (2011). Accurate low dimensional models for deterministic fluid systems driven by uncertain forcing. *Physics of Fluids*, 23(9) :094101.
- Efe, M. and Ozbay, H. (2003). Proper orthogonal decomposition for reduced order modeling : 2d heat flow. In *Control Applications, 2003. CCA 2003. Proceedings of 2003 IEEE Conference on*, volume 2, pages 1273 – 1277 vol.2.
- Ehrenstein, U. and Gallaire, F. (2008). Two-dimensional global low-frequency oscillations in a separating boundary-layer flow. *Journal of Fluid Mechanics*, 614 :315.
- Ehrenstein, U., Passaggia, P.-Y., and Gallaire, F. (2010). Control of a separated boundary layer : reduced-order modeling using global modes revisited. *Theoretical and Computational Fluid Dynamics*, 25 :195–207. 10.1007/s00162-010-0195-5.
- Galletti, B., Bruneau, C., Zannetti, L., and Iollo, A. (2004). Low-order modelling of laminar flow regimes past a confined square cylinder. *J. Fluid Mech.*, 503 :161–170.

- Gibson, J. S., Lee, G. H., and Wu, C. F. (2000). Least-squares estimation of input/output models for distributed linear systems in the presence of noise. *Automatica*, 36(10) :1427 – 1442.
- Glowinski, R. (2003). Finite element methods for incompressible viscous flow. In Ciarlet, P. and Lions, J., editors, *Numerical Methods for Fluids (Part 3)*, volume 9 of *Handbook of Numerical Analysis*, pages 3–1176. Elsevier.
- Godard, G. and Stanislas, M. (2006). Control of a decelerating boundary layer. part 1 : Optimization of passive vortex generators. *Aerospace Science and Technology*, 10(3) :181 – 191.
- Gunzburger, M. (2000). Adjoint equation-based methods for control problems in incompressible, viscous flows. *Flow, Turbulence and Combustion*, 65 :249–272. 10.1023/A :1011455900396.
- Gunzburger, M. and Wood, H. (2003). Perspectives in Flow Control and Optimization. *Appl. Mech. Rev.*, 56 :B82.
- He, J.-W., Chevalier, M., Glowinski, R., Metcalfe, R., Nordlander, A., and Periaux, J. (2000). Drag reduction by active control for flow past cylinders. In Burkard, R., Jameson, A., Strang, G., Deuflhard, P., Lions, J.-L., Capasso, V., Periaux, J., and Engl, H., editors, *Computational Mathematics Driven by Industrial Problems*, volume 1739 of *Lecture Notes in Mathematics*, pages 287–363. Springer Berlin / Heidelberg. 10.1007/BFb0103923.
- Hervé, A., Sipp, D., Schmid, P., and Samuelides, M. (2012). A physics-based approach to flow control using system identification. *J.Fluid Mech.*, 702 :26–58.
- Holmes, P., Lumley, J., and Berkooz, G. (1996). *Turbulence, Coherent Structures, Dynamical Systems and Symmetry*. Cambridge University Press.
- Huang, S.-C. and Kim, J. (2008). Control and system identification of a separated flow. *Phys. Fluids*, 20(10) :101509.
- Ilak, M. and Rowley, C. W. (2008). Feedback control of transitional channel flow using balanced proper orthogonal decomposition. *5th AIAA Theoretical Fluid Mechanics Conference*.
- Illingworth, S., Morgans, A., and Rowley, C. (2011). Feedback control of flow resonances using balanced reduced-order models. *J. Sound Vibr.*, 330(8) :1567–1581.
- Illingworth, S. J., Morgans, A. S., and Rowley, C. W. (2012). Feedback control of cavity oscillations using simple linear models. *Journal of Fluid Mechanics*.
- Illy, H., Geffroy, P., and Jacquin, L. (2005). Contrôle des oscillations de cavité au moyen d'un cylindre placé transversalement à l'écoulement. In *17e congrès de mécanique*.
- Jacquin, L., Molton, P., Deck, S., Maury, B., and Soulevant, D. (2005). An experimental study of shock oscillation over a transonic supercritical profile. *American Institute of Aeronautics and Astronautics Journal*, 35th AIAA Fluid Dynamics Conference and Exhibit :1–11.
- Juang, J. and Pappa, R. S. (1985). An eigensystem realization algorithm for modal parameter identification and model reduction (control systems design for large space structures). *Journal of Guidance, Control, and Dynamics (ISSN 0731-5090)*, 8 :620–627.
- Kim, J. (2003). Control of turbulent boundary layers. *Physics of Fluids*, 15 :1093–1105.

- Kim, J. and Bewley, T. R. (2007). A linear systems approach to flow control. *Annual Review of Fluid Mechanics*, 39(1) :383–417.
- Lacy, S., Venugopal, R., and Bernstein, D. (1998). Armakov adaptive control of self-excited oscillations of a ducted flame. In *Decision and Control, 1998. Proceedings of the 37th IEEE Conference on*, volume 4, pages 4527 –4528 vol.4.
- Lin, J. C. (2002). Review of research on low-profile vortex generators to control boundary-layer separation. *Progress in Aerospace Sciences*, 38(4–5) :389 – 420.
- Ljung, L. (1999). *System Identification*. 2nd edition.
- Luchtenburg, D., Gunther, B., Noack, B., King, R., and Tadmor, G. (2009). A generalized mean-field model of the natural and high-frequency actuated flow around a high-lift configuration. *J. Fluid Mech.*, 623 :283–316.
- Ma, Z., Ahuja, S., and Rowley, C. (2010). Reduced-order models for control of fluids using the eigensystem realization algorithm. *Theoretical and Computational Fluid Dynamics*, pages 1–15. 10.1007/s00162-010-0184-8.
- Marquet, O., Sipp, D., Chomaz, J.-M., and Jacquin, L. (2008). Amplifier and resonator dynamics of a low-reynolds-number recirculation bubble in a global framework. *Journal of Fluid Mechanics*, 605 :429–443.
- Moore, B. (1981). Principal component analysis in linear systems : Controllability, observability, and model reduction. *Automatic Control, IEEE Transactions on*, 26(1) :17 – 32.
- Moreau, E. (2007). Airflow control by non-thermal plasma actuators. *Journal of Physics D : Applied Physics*, 40(3) :605.
- Morgans, A. and Dowling, A. (2007). Model-based control of combustion instabilities. *J. Sound Vib.*, 299(1–2) :261–282.
- Noack, B., Afanasiev, K., Morzynski, M., Tadmor, G., and Thiele, F. (2003). A hierarchy of low-dimensional models for the transient and post-transient cylinder wake. *J. Fluid Mech.*, 497 :335–363.
- Penrose, R. (1955). A generalized inverse for matrices. 51 :406–413.
- Protas, B. and Wesfreid, J. (2002). Drag force in the open-loop control of the cylinder wake in the laminar regime. *Phys. Fluids*, 14 :810–826.
- Rowley, C. (2005). Model reduction for fluids, using balanced proper orthogonal decomposition. *Int. J. Bifurc. Chaos*.
- Rowley, C., Colonius, T., and Murray, R. (2004). Model reduction for compressible flows using pod and galerkin projection. *Physica D Nonlinear Phenomena*, 189 :115–129.
- Safonov, M. and Chiang, R. (1989). A schur method for balanced-truncation model reduction. *Automatic Control, IEEE Transactions on*, 34(7) :729 –733.
- Samimy, M., Debiasi, M., Caraballo, E., Ozbay, H., Efe, M., and Yuan, X. e. a. (2003). Development of closed-loop control for cavity flows. *AIAA Paper*, 4258.

- Samimy, M., Debiasi, M., Caraballo, E., Serrani, A., Yuan, X., Little, J., and Myatt, J. H. (2007a). Feedback control of subsonic cavity flows using reduced-order models. *Journal of Fluid Mechanics*, 579 :315–346.
- Samimy, M., Kim, J.-H., Kastner, J., Adamovich, I., and Utkin, Y. (2007b). Active control of high-speed and high-reynolds-number jets using plasma actuators. *Journal of Fluid Mechanics*, 578 :305–330.
- Semeraro, O., Bagheri, S., Brandt, L., and Henningson, D. S. (2011). Feedback control of three-dimensional optimal disturbances using reduced-order models. *Journal of Fluid Mechanics*, 677 :63–102.
- Shih, W., Wang, C., Coles, D., and Roshko, A. (1993). Experiments on flow past rough circular cylinders at large reynolds numbers. *Journal of Wind Engineering and Industrial Aerodynamics*, 49(1–3) :351 – 368.
- Sipp, D. and Lebedev, A. (2007). Global stability of base and mean flows : a general approach and its applications to cylinder and open cavity flows. *J. Fluid Mech.*, 593 :333–358.
- Sipp, D., Marquet, O., Meliga, P., and Barbagallo, A. (2010). Dynamics and control of global instabilities in open flows : A linearized approach. *Appl. Mech. Rev.*, 63(3) :030801.
- Sirisup, S. and Karniadakis, G. (2004). A spectral viscosity method for correcting the long-term behavior of POD models. *J. Comp. Phys.*, 194(1) :92–116.
- Sirovich, L. (1991). Analysis of turbulent flows by means of the empirical eigenfunctions. *Fluid Dynamics Research*, 8(1–4) :85 – 100.
- Tadmor, G. and Noack, B. (2004). Dynamic estimation for reduced galerkin models of fluid flows. In *American Control Conference, 2004. Proceedings of the 2004*, volume 1, pages 746 –751 vol.1.
- Tokumaru, P. and Dimotakis, P. (1991). Rotary oscillation control of a cylinder wake. *J. Fluid Mech.*, 224 :77–90.
- Willcox, K. and Peraire, J. (2002). Balanced model reduction via the proper orthogonal decomposition. *AIAA Journal*, 40 :2323–2330.